

ALMA MATER STUDIORUM – UNIVERSITÀ DI BOLOGNA

SCUOLA DI INGEGNERIA E ARCHITETTURA

Sede di Forlì

Corso di Laurea in Ingegneria Aerospaziale Classe LM-20

TESI DI LAUREA

in Dinamica e Controllo Orbitale LM

**Tracking, photometry and spectroscopy of space debris:
the Malindi, Loiano, Las Campanas and Cerro Tololo
observation campaign results**

Candidato:
Tommaso Cardona

Relatore
Prof. Fabrizio Piergentili

Correlatore
Prof. Patrick Seitzer
University of Michigan

Controrelatore
Prof. Paolo Tortora

Anno Accademico 2012/13

Sessione II

A mio padre

Index

Abstract	7
Sommario	9
Chapter 1	
Introduction to Space Debris	11
1.1 – Definition of space debris.....	12
1.2 – Optical measurements.....	16
1.2.1 – Astrometry applied to space debris	16
1.2.2 – Photometry applied to space debris	18
1.2.2.1 – Magnitude	19
1.2.2.2 – Colors.....	19
1.2.2.3 – The atmosphere.....	20
1.2.2.4 – Light curves.....	24
1.2.3 – Spectroscopy applied to space debris	26
1.2.3.1 – Optical reduction	29
Chapter 2	
ALMASCOPE at Broglio Space Center in Kenya	33
2.1 – The ALMASCOPE observatory.....	34
2.2 – The Malindi test campaign	38
2.2.1 - Observation campaign statistical results.....	39
Chapter 3	
The Loiano campaigns for physical characterization of space debris	45
3.1 – The G.D. Cassini Observatory	46
3.2 – Observation nights.....	48
3.3 – Data processing	51
3.3.1 – Reflectance	52
3.4 – Results.....	52
3.4.1 – February and April 2011	52
3.4.2 – August 2011.....	58

Chapter 4	
Optical reflection spectroscopy of space debris.....	65
4.1 – The observatory used	66
4.1.1 – Magellan	66
4.1.2 – MODEST	69
4.3 – Blind Non-Sidereal Tracking problem	70
4.4 – Rates correction code	73
4.5 – GUI (Graphical User Interface) development	80
4.5.1 – Test at Angel Hall Observatory	89
Chapter 5	
Chile observing campaigns	97
5.1 – First test at Magellan Telescope in May 2012	97
5.2 – Test at Magellan Telescope in January 2013	103
5.2.1 – Results.....	105
5.2.1.1 – Titan IIIC Transtage debris	106
5.2.1.2 - Other GEO Debris	107
5.2.1.3 – IDCSP Observations	108
5.2.3 – Results discussion	109
5.3 – Test at MODEST in February 2013	110
Chapter 6	
Conclusions.....	115
6.1 – ALMASCOPE conclusion.....	115
6.2 – Loiano observation campaign conclusion and future work	115
6.3 – Future work with NASA Orbital Debris Program Office.....	116
Appendix	119
A.1 – Celestial Equatorial Coordinate System	119
A.2 - Definition of Two-line Element Set Coordinate System.....	121
Bibliography	123
Reference	125
Acknowledgements.....	131

Abstract

The main purpose of my thesis has been the analysis of the space debris environment and their characterization through optical measurements. In particular I had the opportunity to contribute to the Italian Space Agency activities in space debris optical observation campaign and I cooperated directly with NASA Orbital Debris Program Office by working at the Astronomy Department of the University of Michigan for six months.

The thesis contains the results of four different observation campaigns, which I participated actively working on designing observation strategy, collecting measurements and analyzing data:

- at the Broglio Space Center in Malindi for the ALMASCOPE project, an Italian observatory fully dedicated to space surveillance
- at the G. D. Cassini Observatory in Loiano for physical characterization of space debris
- at the NASA Observatories Las Campanas and Cerro Tololo in Chile to complete my work started at the Astronomy Department of the University of Michigan coordinated by prof. Patrick Seitzer

The thesis contains the results of these observing campaigns and the code that I have realized to achieve them, in particular the blind non-sidereal tracking code realized for NASA Orbital Debris Program Office to perform spectroscopy of orbital debris at the 6.5 m Magellan telescope and the correlated Graphical User Interface (GUI) created to interface the observatory hardware in order to automate all the observing procedures.

I co-authored a number of papers during my thesis works which have been published and presented on international journals and at different congresses focused on space debris:

“Space debris measurement using joint mid- latitude and equatorial optical observations” from Piergentili, Ceruti et al. published on IEEE Transactions on Aerospace and Electronic Systems analyzes a system for orbital object monitoring, using a mid-latitude and an equatorial observatory. The enhancements with respect to the use of a single telescope located at mid latitude, for space debris detection and tracking are highlighted in terms of surveying volume, object identification and orbital determination accuracy on the basis of measurements achieved during the 2010 Malindi observation campaign.

“Physical characterization of space debris in the geosynchronous region”, “The Loiano campaigns for photometry and spectroscopy of geosynchronous objects” and *“Physical characterization of objects in the*

GEO region with the Loiano 1.5m telescope” from Rossi, Cardona et al. presented at International Astronautical Conference (space debris session) and the European Conference on Space Debris showed the obtained data at the Loiano campaigns and the discussion on how to establish the physical nature and hence, possibly, the origin of the space debris observed and, moreover, the analysis of the light-curves of these objects, to achieve information on their shape.

“Optical Reflection Spectroscopy of GEO Objects”, “Visible Light Spectroscopy of GEO Debris” and *“Comparisons of a Constrained Least Squares Model versus Human-in-the-loop for Spectral Unmixing to Determine Material Type of GEO Debris”* from Seitzer, Cardona et al. presented at IAC, AMOS conference and European Conference on Space Debris show optical spectroscopy obtained with an imaging spectrograph on one of the twin 6.5-m Magellan telescopes at Las Campanas Observatory in Chile and the identification of each object’s suspected material component.

Sommario

Lo scopo principale della mia tesi è stato l'analisi dell'ambiente dei detriti spaziali e la loro caratterizzazione attraverso misurazioni ottiche al telescopio. In particolare ho avuto l'opportunità di contribuire all'attività dell'Agenzia Spaziale Italiana nelle campagne di osservazione dei detriti spaziali e di cooperare direttamente con il *NASA Orbital Debris Program Office* lavorando al Dipartimento di Astronomia dell'Università del Michigan per sei mesi.

La tesi contiene i risultati di quattro differenti campagne di osservazione cui ho partecipato, lavorando attivamente sulla pianificazione della strategia di osservazione, la raccolta di misurazioni e analisi dei dati:

- al Broglio Space Center di Malindi per il progetto ALMASCOPE, un osservatorio italiano completamente dedicato alla *"space surveillance"*
- al telescopio the G. D. Cassini di Loiano per la caratterizzazione fisica dei detriti
- agli osservatori NASA di Las Campanas e Cerro Tololo in Cile per completare il lavoro da me iniziato presso il Dipartimento di Astronomia dell'Università del Michigan, coordinato dal Prof. Patrick Seitzer

La tesi contiene i risultati di queste campagne di osservazioni e lo sviluppo dei codici da me realizzati per raggiungerli, in particolare un capitolo tratta lo sviluppo del codice per il *"blind non-sidereal tracking"* che ho realizzato per il NASA Orbital Debris Program Office al fine di realizzare indagini spettroscopiche al telescopio Magellan, e lo sviluppo della correlata interfaccia grafica (GUI) creata come interfaccia dell'hardware dell'osservatorio per automatizzare le procedure di osservazione dei detriti spaziali.

Sono stato co-autore di diversi articoli durante il mio lavoro di tesi che sono stati pubblicati e presentati su riviste internazionali e a diverse conferenze focalizzate sui detriti spaziali:

"Space debris measurement using joint mid- latitude and equatorial optical observations" di Piergentili, Ceruti et al. pubblicato su IEEE Transactions on Aerospace and Electronic Systems analizza un sistema per il monitoraggio di detriti spaziali usando un doppio osservatorio localizzato a media latitudine ed equatoriale. Sono riportati i vantaggi rispetto all'uso di un singolo osservatorio a medie latitudini per quanto riguarda l'identificazione e il tracciamento dei detriti spaziali, questi vantaggi sono analizzati in termini di maggior numero di oggetti identificati e maggior accuratezza orbitale sulla base delle misurazioni ottenute durante la campagna di osservazioni del 2010 a Malindi.

“Physical characterization of space debris in the geosynchronous region”, “The Loiano campaigns for photometry and spectroscopy of geosynchronous objects” and “Physical characterization of objects in the GEO region with the Loiano 1.5m telescope” di Rossi, Cardona et al. presentati all’International Astronautical Conference (sessione relative ai detriti spaziali) e all’European Conference on Space Debris mostrano I risultati ottenuti durante le campagne di osservazione al telescopio di Loiano e discutono come stabilire la natura fisica ed eventualmente l’origine dei detriti spaziali osservati. Inoltre è presente l’analisi delle curve di luce di tali oggetti, al fine di ottenere maggiori informazioni riguardanti la loro forma.

“Optical Reflection Spectroscopy of GEO Objects”, “Visible Light Spectroscopy of GEO Debris” e “Comparisons of a Constrained Least Squares Model versus Human-in-the-loop for Spectral Unmixing to Determine Material Type of GEO Debris” di Seitzer, Cardona et al. presentati alle conferenze at IAC, AMOS ed European Conference on Space Debris mostrano I risultati delle indagini spettroscopiche ottenute durante le campagne di osservazione ad uno dei due telescopi gemelli Magellan situati all’osservatorio di Las Campanas in Cile e l’identificazione dei componenti dei materiali analizzati.

Chapter 1

Introduction to Space Debris

Human space activities are principally concentrated in three Earth orbit altitude regions. These regions are Low Earth Orbit (LEO), Semi-Synchronous Orbit and Geosynchronous Earth Orbit(GEO). Each of these offers specific advantages. LEO, 200-2.000 km high, has the advantage of relative ease of access for the large masses required for piloted spacecraft. In fact close proximity to Earth makes LEO attractive for automated high-resolution-imaging spacecraft and high-signal strength communications. Semi-synchronous orbits from 10000 to 20000 km high are important for navigation (Global Positioning System constellation), as well as communications. GEO is about 36000 km high. The satellite telecommunications industry uses the Geostationary Arc, for example for weather satellites (figure 1.1).

As a general rule, the higher above Earth's atmosphere a satellite orbits, the longer it will persist in orbit. At GEO altitude, atmospheric drag is unimportant. A GEO satellite is likely to orbit for millions of years. LEO is continually cleansed by atmospheric drag. However, many LEO objects orbit for years, and most will orbit for centuries. The oldest artificial space object is the U.S. Vanguard 1 satellite. The 3968 x 650 km orbit it reached on March 17, 1958, ensured its longevity. The first satellite, the Soviet Union's Sputnik-1, decayed from its low orbit on January 1, 1958, less than 3 months after launch.

In March 2013 the NSSDC Master Catalog listed 6.936 satellites which had been launched into orbit since 1957. [1]



Figure 1.1 – Satellites and Space debris orbiting around the Earth. The geostationary arc is visible [2]

On June 29, 1961, the US Transit-4A satellite was launched from Kennedy Space Center on a Thor-Albestar rocket [3]. The spacecraft was deployed into an orbit altitude between 881 and 998 km, with an inclination of 66.8°. Transit-4A was catalogued by First Aerospace Control Squadron of the US Air Force as the 116th space object since the launch of Sputnik-1 on October 4, 1957. At 06:08:10 UTC on June 29, 77 min after the injection and separation of Transit-4A and two additional payloads, the Ablestar upper-stage exploded, distributing its dry mass of 625 kg across at least 298 trackable fragments, of which nearly 200 were still on orbit more than 40 years later. This first on-orbit break-up event in space history increased instantaneously by at least a factor of 3.5 the number of orbiting objects [4]. Since this date space debris has been the largest contributor to the observable space object population, with on-orbit explosion as its largest cause.

1.1 – Definition of space debris

The terms *space debris* and *orbital debris* are often used as synonyms, with the following definition as adopted by the IADC: “*Space debris are all man-made objects including fragments and elements thereof, in Earth orbit or re-entering the atmosphere, that are non-functional.*” [5]. According to this definition, 46.5% of the catalogued space objects prior to the Ablestar explosion would have been classified as space

debris, for instance in the form of spent upper stages and mission-related release objects (not counting decommissioned satellites).

With increasing launch and deployment activities, the space debris environment also started to take shape. In August 1964 the first geostationary satellite, Syncom-3, was deployed. In June 1978, the first spacecraft explosion happened in GEO. In 1979 Lubos Perek, chief of the Outer Space Affairs Division at the United Nations, presented a paper on "*Outer Space Activities versus Outer Space*", which was the first to recommend space debris migration measures, including the re-orbiting of GEO spacecraft into a disposal orbit at the end of life [6].

Nowadays, more than 500000 pieces of debris are tracked as they orbit the Earth. They all travel at speeds up to 7.9 km/s, fast enough for a relatively small piece of orbital debris to damage a satellite or a spacecraft. The rising population of space debris increases the potential danger to all space vehicles, but especially to the International Space Station and other spacecraft with humans aboard [7].

Some recent events have pushed IADC member agencies to increase their capability for Space Debris Surveillance:

- China's 2007 anti-satellite test, which used a missile to destroy an old weather satellite, added more than 3000 pieces to the debris problem.
- On February 10, 2009, a defunct Russian satellite collided with and destroyed a functioning U.S. Iridium commercial satellite. The collision added more than 2000 pieces of trackable debris to the inventory of space junk (figure 1.2).
- The starting of the European program SSA (Space Situational Awareness) which provides for the building of a network of European observatories and radar.

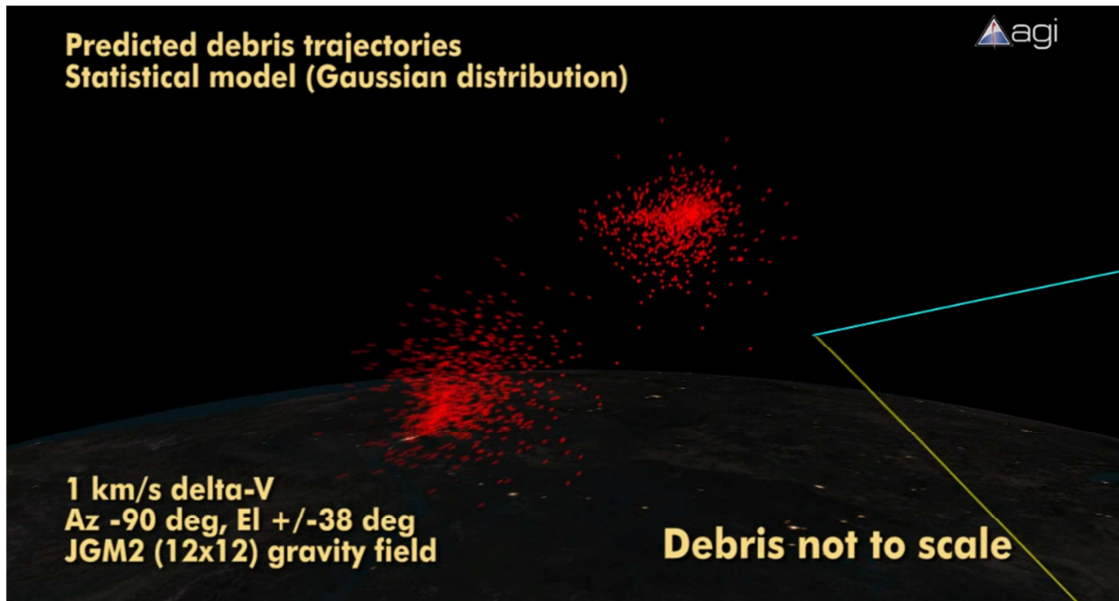


Figure 1.2 – Cosmos vs. Iridium[8]

NASA and the DoD (Department of Defense) cooperate and share responsibilities for characterizing the satellite (including orbital debris) environment. The DoD’s Space Surveillance Network tracks discrete objects as small as 5 cm in diameter in LEO and about 1 m in GEO. Currently, about 15000 officially cataloged objects are still in orbit. The total number of tracked objects exceeds 21000. NASA statistically determines the extent of the population for objects less than 10 cm in diameter (figure 1.3).

Collision risks are separated into three categories depending upon size of threat (table 1.1). For objects 10 cm and larger, conjunction assessments and collision avoidance maneuvers are effective in countering objects that can be tracked by the Space Surveillance Network. Objects smaller than this are usually too small to track and too large to shield against. Debris shields can be effective in withstanding impacts of particles smaller than 1 cm.

Table 1.1
Population sizes of objects in Earth orbit [9]

Category	Definition	Estimated population	Potential Risk to Satellite
Trackable	> 10 cm in diameter	19000+	Complete destruction
Potentially Trackable	> 1 cm in diameter	Several hundred thousand	Complete to partial destruction
Untrackable	< 1 cm in diameter	Many millions to billions	Degradation, loss of certain sensors or subsystems

Because satellites are clustered in a few useful orbits and objects remain in those orbits for many years, the risk of a collision is higher than might be expected. Computer models based on observations of debris are used to predict future growth of the debris population, and thus the probability of collisions with satellites, under different expectations. As shown in figure 1.4, in the next 40 years, such a collision is expected to occur every 5 years on average. Mitigation measures reduce the number of impacts (middle line), but even if no satellites are launched from now on, the number of collisions will continue to increase (lower line). Current trends is somewhere between the upper and middle lines.

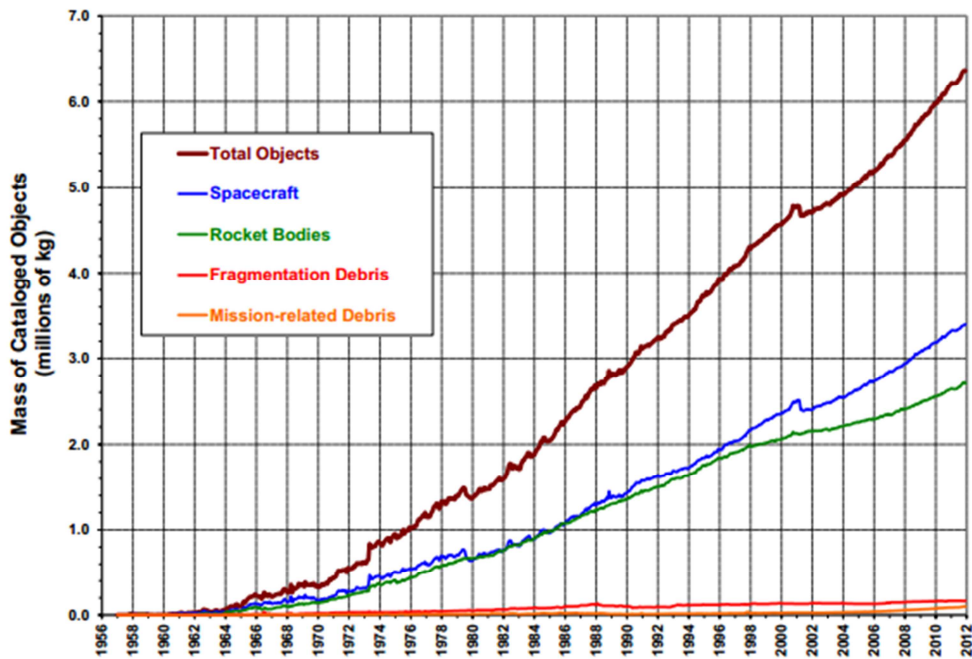


Figure 1.3 – Number and type of catalogued debris objects over time [10]

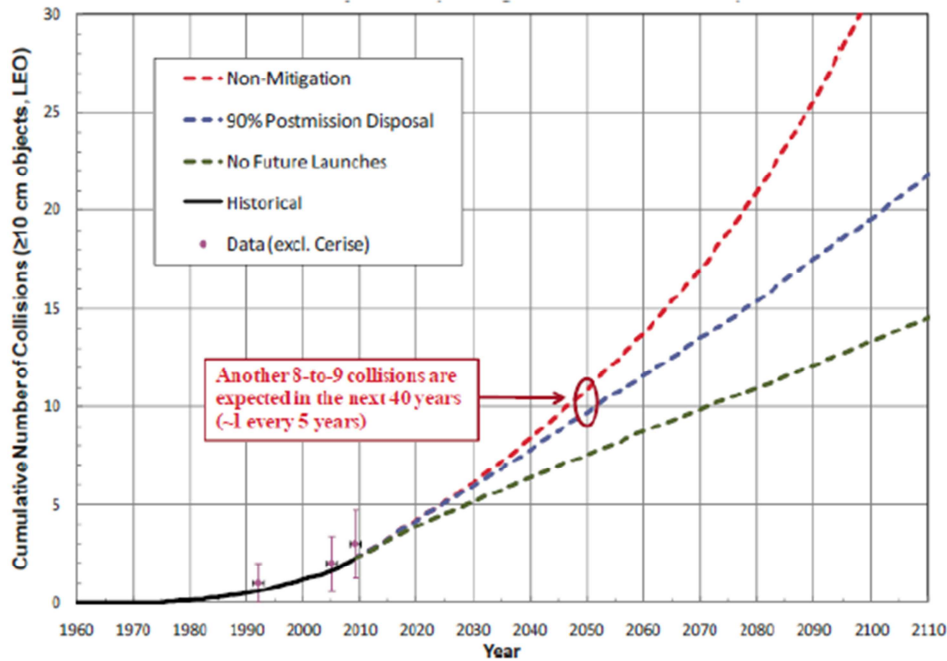


Figure 1.4 – The cumulative number of collisions with objects larger than 10cm in LEO expected over the next century [10]

1.2 – Optical measurements

To model the space debris environment it is necessary to collect data regarding actual situation, thus optical measurements are required. According to the Inter-Agency Space Debris Coordination Committee (IADC), an international governmental forum for the worldwide coordination of activities related to the issues of man-made and natural debris in space, international observation campaigns for debris determination in higher orbit have been promoted. The aim of these campaigns is to determine and characterize the space debris especially on the LEO and GEO regions. In particular for GEO region optical means are more used than radar ones due to the low sensitivity of radar at long distances. At the present the only way to detect and characterize space debris in this region is through optical measurements. Main space debris research field are astrometry photometry and spectrophotometry.

1.2.1 – Astrometry applied to space debris

Professor Thomas Schildknecht from the University of Bern in *“Optical astrometry of fast moving objects using CCD detectors”* [11] describes astronomy as “the science of measuring position, velocity and shape of the object in the sky”. The results he achieved firstly in 1994 and presented in that publication with geostationary satellites increased the use of CCD technology for applied problems of orbital mechanics:

many objects in the GEO belt were finally observed with CCD detectors with an accuracy sufficient for precise orbit determination and active positioning.

Due to these techniques an unexpected space debris population has been detected in 2004 Schildknecht et al. ([12],[13]) with the unique properties of a very high area-to-mass ratio (HAMR) (figure 1.5).



Figure 1.5 – HAMR materials [12]

The orbits of those objects are heavily perturbed by the effect of direct radiation pressure. Unknown attitude motion complicates orbit prediction. The area-to-mass ratio of the objects seems to be not stable over time. With optical observations of several HAMR objects, observed over several years and investigates the variation of their area-to-mass ratio and orbital parameters. A normalized orbit determination setup has been established and validated with two low and two of the high ratio objects, to ensure, that comparable orbits over longer time spans are determined even with sparse optical data. A sparse data setup was established to create comparable orbits over longer time intervals. Orbits with two data sets only do produce small differences between the propagated ephemerides and further observations, as long as 1.2 hours are covered within the sets. Other factors, such as that the observations stem from different sites or the time interval between the sets, are found to be negligible.

The orbits of high area-to-mass ratio (HAMR) objects were analyzed in this setup. The AMR value, that is the scaling factor of the direct radiation pressure (DRP) parameter, varies over time. The order of

magnitude of the variation of the area-to-mass ratio (AMR) value was not correlated with the order of magnitude of its error [12].

The variation of the AMR is not averaged out in the fit interval of orbit determination. In the evolution of the AMR value over time, no common characteristic could be determined for different HAMR objects. Further work on the orbits of HAMR objects is needed, to improve the radiation pressure model, to determine possible attitude motion or deformations and to understand also resonance effects and the existence of chaotic regions [13].

1.2.2 – Photometry applied to space debris

The most fundamental information we can measure about orbiting objects is the amount of energy, in the form of electromagnetic radiation, that we receive from that and it could radiated if we consider a star or reflected if a space debris. This quantity is called the flux. The flux that is reflected from the object is strictly dependent on the attitude of the debris. In fact if we consider a debris that has exposed perpendicularly to the sun some parts of solar panels, the flux reflected will be different from the one reflected from the same debris with the solar panels parallel to the direction of the sun. The science of measuring the flux received is called photometry.

All astronomical information comes to us from some form of electromagnetic radiation (EMR). It is possible to study EMR over a range of wavelength covering a range from short wavelength, high photon energy gamma rays to long wavelength, low energy radio photons. The range of wavelengths our eyes are sensitive to is called the visible wavelength range and goes from 4500 to 6500Å [14]

All EMR comes in discrete lumps called photons. A photon has a definite energy and frequency or wavelength. The relation between photon energy E_{ph} and photon frequency ν is given by:

$$E_{ph} = h\nu \quad (1.1)$$

or, since $c = \lambda\nu$

$$E_{ph} = \frac{hc}{\lambda} \quad (1.2)$$

where h is Planck's constant and λ is the wavelength, and c is the speed of light.

The energy of visible photons is around few electron volts. Much of the EMR spectrum is blocked by the atmosphere, and can only be studied using telescopes placed above the atmosphere (e.g. Hubble Space

Telescope, James Webb Space Telescope). Only in the optical and radio regions of the spectrum are there large atmospheric windows (portions of the EMR spectrum for which the atmosphere is at least partially transparent) that allow to study the universe.

The goal is to make measurements of the EMR from space objects with finest resolution possible (with different type of detail like angular detail, wavelength detail, and time detail).

The observation are always limited in angular and wavelength coverage, and limited in resolution in angle and wavelength. The ideal goal is to obtain the spectral energy distribution (SED) reflected by the objects (space debris in this case), or how the energy reflected from the object is distributed in wavelength. It is necessary to use a filter that pass only certain wavelengths of lights. If we put a filter in front of CCD camera, we obtain an image just in the wavelengths passed by the filter. This give us the opportunity to measure the brightness of an object [14].

1.2.2.1 - Magnitude

Magnitude is the logarithmic measure of the brightness of an object (power fluxes, or energy received per unit time per unit area) measured in a specific wavelength.

Considering two objects (for example two stars), with flux f_1 and f_2 , it is possible to define the magnitude difference between the two as:

$$m_1 - m_2 = -2.5 \log \left(\frac{f_1}{f_2} \right) \quad (1.3)$$

The most common use for magnitudes is for expressing the apparent brightness of stars. To give a definite number for a magnitude of an object (instead of just the magnitude difference between two different objects), it has to be pick a starting place, or zero point, for the magnitude system by using standard stars [14].

1.2.2.2 - Colors

One widely used filter system in the optical region of the spectrum is called the UBVRI system. The letters correspond to different filters: U for ultraviolet, B for blue, and V for visual, R for red, I for infrared. The central wavelengths of the filters are roughly: U – 3650Å, B – 4450Å, V – 5500Å, R – 6600Å, I – 8000Å.

The magnitude are defined in each filter. The color of an object is related to the variation of flux with wavelength. Using broadband UBVRI the color index is defined as the difference between the magnitudes in 2 colors, e.g.

$$B - V = m_B - m_V \quad (1.4)$$

defines the B – V color index.

From the basic equation defining magnitudes (1.3) we see that a magnitude difference corresponds to a flux ratio. The ratio is the flux at B relative to the flux at V, of the same object, instead of different objects.

$$B - V = m_B - m_V = -2.5 \log \left(\frac{f_B}{f_V} \right) + const \quad (1.5)$$

Where f_B is the flux averaged over the B filter and f_V is the flux averaged over the V filter. The *const* appears in the above equation because of the way the zero point of the color system is defined.

For broadband UBVRI filter system the standard stars used most frequently today to determine the value of the constant are from the work of the astronomer Arlo Landolt, who defined classes of not variable stars with the main characteristic of a brightness that do not overwhelm the detector and telescope in use, with a good S/N in a short exposure ([16],[17]).

1.2.2.3 - The atmosphere

The atmosphere absorbs some fraction of the light from all celestial objects. The amount of light absorbed is different for different wavelengths, and also changes with time. The dimming of light in its passage through the atmosphere is called atmospheric extinction.

There several problems connected to the presence of the atmosphere, principally the Earth's atmosphere allows only a small fraction of all wavelengths of EMR to penetrate, moreover the light passing through turbulent atmosphere causes smearing of images of the objects (seeing). It is also important to consider the atmospheric extinction (the atmosphere absorbs and scatters some fraction of the light at all optical wavelengths) and refraction (the atmosphere acts as a prism, spreading out light in a small spectrum along the line pointing to the zenith) [14].

For these reasons the passage of the light rays through the atmosphere scrambles the rays slightly and makes them no longer exactly parallel. The direction of the rays is being continuously changed by a slight amount, as the rays traverse the turbulent atmosphere. Seeing makes the images of stars appear much

larger than the limit set by diffraction, does not refer to the loss of light but only to the loss of detail caused by scrambling of light rays. It is characterized the seeing by the angular FWHM (full width at half maximum), which is the angular size of the star image at a level of half the peak level (figure 1.6).

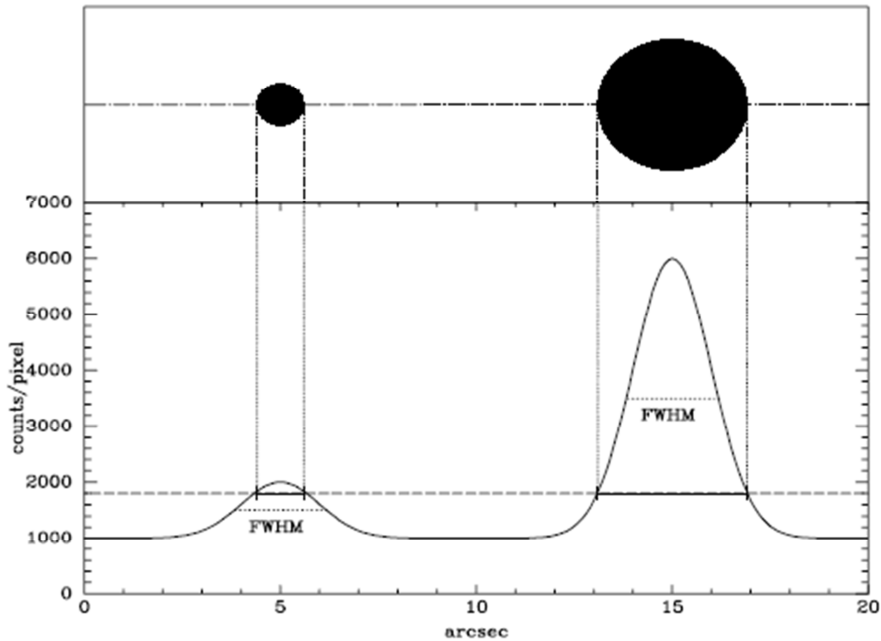


Figure 1.6 – Top: schematic image of a faint star and a bright star, showing brighter star looking bigger than fainter. Bottom: Brightness profile along dot-dash line crossing the centers of the two stars. The shapes of the two stars are exactly the same, the bright star is simply 5 times the intensity above sky at each point relative to the faint star. Brightness along the dashed line at constant level of 1800 counts/ pixel across image shows that, while the bright and faint star have the same shape, the bright star looks bigger at each gray level on the image. The dotted line on each star profile marks the FWHM of each star. [14]

Radiation transfer is the branch of astrophysics that deals with how EMR travels through and interacts with matter. One of the central concepts of radiation transfer is that of optical depth, indicated with τ . Considering a slab of gas that absorbs a very small fraction of any EMR that falls on it. Say we have a beam of EMR of flux f_{inc} (incident flux) and that the output flux (f_{out}) is 0.99 that of f_{inc} (as shown in figure 1.7). It is possible to say that the optical depth of the slab is 0.01.

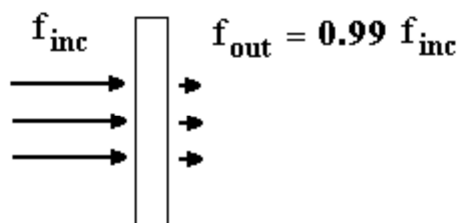


Figure 1.7 – A thin slab which absorbs 1% of light incident on it [14]

If there are a more opaque slab (e.g. a slab composed of 50 of the slabs from the previous figure stuck next to each other like in figure 1.8) the relationship between f_{inc} and f_{out} of the 50th slab is:

$$f_{out} = f_{inc}(0.99)^{50} = f_{inc} \left(1 - \frac{0.5}{50}\right)^{50} = 0.61f_{inc} \quad (1.6)$$

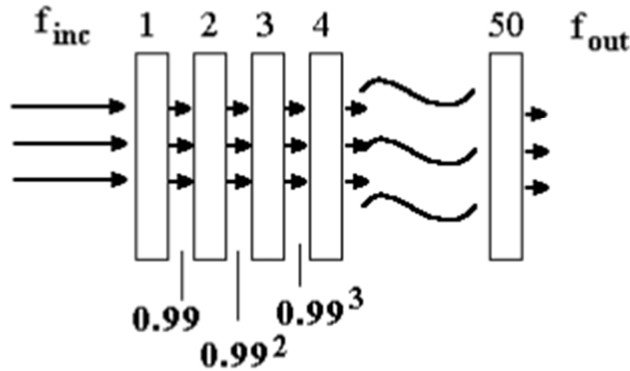


Figure 1.8 – A slab consisting of 50 smaller slabs each absorbing 1% of the light incident on them[14]

The output flux is

$$e^{-\tau} = e^{-0.5} = 0.61 \quad (1.7)$$

In general, the incident and output flux of a slab of optical depth τ are related by the equation

$$f_{out} = f_{inc}e^{-\tau} \quad (1.8)$$

So τ is defined as

$$\tau = -\ln\left(\frac{f_{out}}{f_{inc}}\right) \quad (1.9)$$

This configuration of an absorbing slab and incident beam and output beam is about the simple radiation transfer problem there is (in fact in almost every real case, τ varies strongly with wavelength λ).

It is possible to think of the atmosphere as an absorbing slab. Consider the beam of light from some star that will hit our telescope mirror. Just outside the atmosphere, the beam has flux f_{inc} . At the telescope, the flux of this beam is less due to absorption and scattering of light out of the beam (f_{obs}) (figure 1.9).

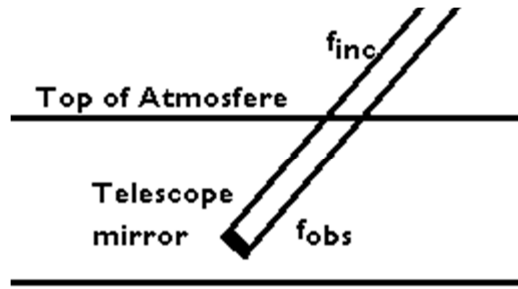


Figure 1.9 – Beam of the light from an object that will hit the telescope [14]

If the telescope look straight up (at the zenith) there is minimum possible path length through the atmosphere (for a given altitude of observatory). At an angle θ from the zenith (called the zenith angle) the amount of air the telescope look through, relative to that at zenith, is given by secant θ (figure 1.10).

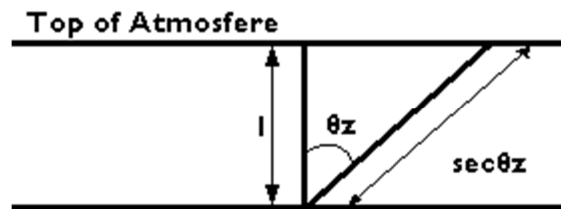


Figure 1.10 – Airmass equals secant of the zenith angle

The relation of f_{obs} (at zenith) and f_{inc} can be specified by the optical depth τ_1 of the atmosphere at zenith. To solve this is possible to measure the change in extinction in the atmosphere at different airmasses (different zenith angles) and extrapolate the observed flux to 0 airmass (above the atmosphere): the common strategy is to measure the flux of a star, wait until the star rises or sets some, so that the zenith angle changes, then measure the flux again. From these two fluxes, the optical depth at zenith can be derived. Instead of talking about τ_1 directly, a related quantity called the absorption coefficient K is used. It has units magnitudes per unit airmass and it is obtained from

$$K = 2.5 \log \left(\frac{f_{inc}}{f_{obs}(\theta = 0)} \right) \quad (1.10)$$

1.2.2.4 - Light curves

By calculating the value of brightness with the filters UBVRI it is possible to construct a graph called light curve that shows the brightness of an object over a period of time (figure 1.11)

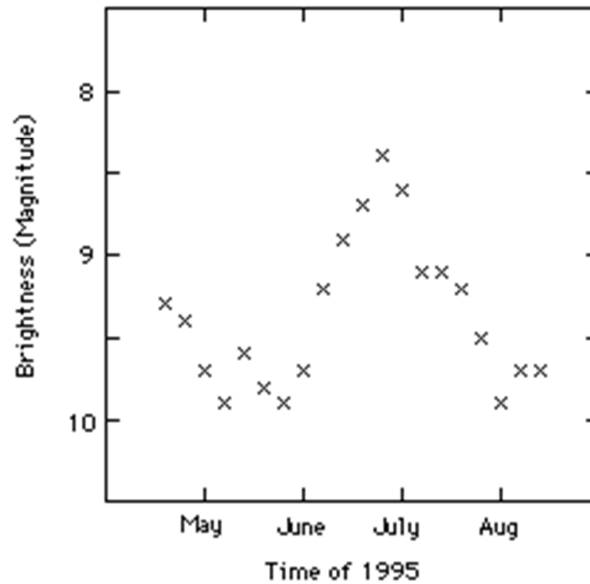


Figure 1.11 - Light curve of a star during a period of six months [18]

Satellites and in particular space debris do not have a constant brightness, they give off flashes at typically regular times. This flashing behavior is caused by the tumbling motion of the object. The satellite's metallic surfaces act as mirrors for the sun (specular reflection). Objects with a diffusely reflecting surface will also show varying brightness since the observer will see a changing amount of light reflecting area of the rocket as it tumbles about in its orbit. Measuring the period between two flashes or maxima/minima in the light curve can give a good approximation for the satellite's rotation motion (figure 1.12).



Figure 1.12 – Tumbling images of SL12RB 26895 with 60 sec exposition taken at the Loiano Observatory

It is possible to define a *flash period* as the time interval between two flashes. Measuring the time interval during which the space debris has flashed some tens of times can, after dividing this total time by the number of flash periods, give a good approximation for the true rotation motion. Counting at least hundred flashes, an accuracy of up to 0.001 seconds can be obtained. However, the rotation period can be correlated to the flashes pattern through analysis of geometrical configuration and physical composition of the satellite if known. The attitude motion changes during space debris lifetime due to perturbations that act on the object, like the earth magnetic field , the solar radiation pressure or the atmospheric drag for LEO. Especially for HAMR objects the solar radiation pressure it is very important because due to the intrinsically characteristic of high area to mass of the debris, the interaction between the surface and the radiation pressure is very high. This interaction can change the attitude and these changings are observable even in short period on light curves [19].

These techniques to reconstruct the attitude and determine angular velocity have been used by professor Santoni et al. [20] and the results have been presented at 63rd International Astronautical Congress 2012.

1.2.3 – Spectroscopy applied to space debris

Spectroscopy is one of the essential tools at astronomer’s disposal, permitting to determine the chemical compositions, physical properties, and radial velocities of astronomical sources. If we can measure the flux in small wavelength intervals, we start to see that the flux is quite irregular on small wavelength scales. This is connected to the interaction of light with the atoms and molecules in the object. By studying these “bumps and wiggles” in the flux as a function of wavelength, it is possible to understand what it is made of, how the object is moving and rotating, the pressure and ionization of the material in the object, etc. All astronomical spectrographs contain four necessary elements (figure 1.13): a slit on to which the light from the telescope could be focused; a collimator, which would take the diverging light beam and turn it into parallel light; a disperser that is typically a reflection grating; and a camera that would then focus the spectrum onto the detector ([14], [15]).

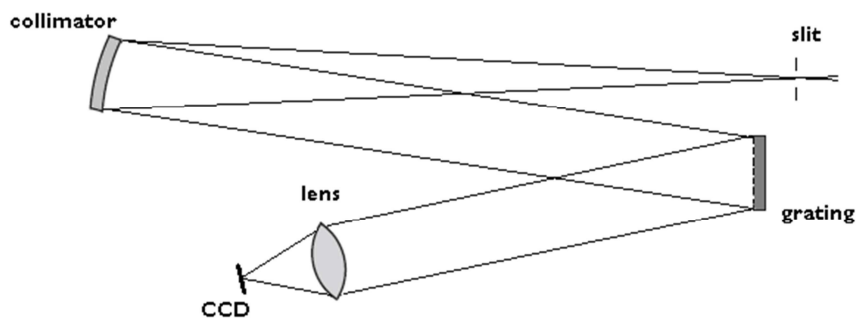


Figure 1.13 – Main components of an astronomical spectrograph

The slit sits in the focal plane, and usually has an adjustable width w . The image of the object is focused onto the slit. The diverging beam continues to the collimator, which has focal length L_{coll} . The f -ratio of the collimator (its focal length divided by its diameter) must match that of the telescope beam, and hence its diameter has to be larger the further away it is from the slit, as the light from a point source should just fill the collimator. The collimator is usually an off-axis paraboloid, so that it both turns the light parallel and redirects the light towards the disperser [15].

In most astronomical spectrographs the disperser is a grating, and is ruled with a certain number of grooves per mm, usually of order 100-1000. If one were to place one’s eye near where the camera is shown in figure 1.13 the wavelength λ of light seen would depend upon exactly what angle i the grating was set at relative to the incoming beam (the angle of incidence), and the angle θ the eye made with the normal to the grating (the angle of diffraction) [15]. How much one has to move one’s head by in order to change

wavelengths by a certain amount is called the dispersion, and generally speaking the greater the projected number of grooves/mm (e.g. as seen along the light path), the higher the dispersion, all other things being equal. The relationship governing all of this is called *the grating equation* and is given as

$$m\lambda = \sigma(\sin i + \sin \theta) \quad (1.11)$$

In the grating equation, m is an integer representing the order in which the grating is being used. Without moving one's head, and in the absence of any order blocking filters, one could see 8000Å light from first order and 4000Å light from second order at the same time. An eye would also have to see further into the red and blue than human eyes can manage, but CCDs typically have sensitivity extending from 3000–10000Å, so this is a real issue, and is solved by inserting a blocking filter into the beam that excludes unwanted orders, usually right after the light has passed through the slit [15].

The angular spread (or dispersion) of a given order m with wavelength can be found by differentiating the grating equation:

$$\frac{d\theta}{d\lambda} = \frac{m}{\sigma \cos \theta} \quad (1.12)$$

for a given angle of incidence i . Note, though, from (Eq. 1.11)

$$\frac{d\theta}{d\lambda} = \frac{(\sin i + \sin \theta)}{\lambda \cos \theta} \quad (1.13)$$

In the Littrow condition ($i = \theta$), the angular dispersion is given by:

$$\frac{d\theta}{d\lambda} = \frac{2}{\lambda} \tan \theta \quad (1.14)$$

These must be used in low order (m is typically 1 or 2) to avoid overlapping wavelengths from different orders. These spectrographs are designed to be used with a small angle of incidence (e.g. the light comes into and leaves the grating almost normal to the grating) and the only way of achieving high dispersion is by using a large number of grooves per mm (e.g. σ is small in Eq. 1.12). Note from the above that in the Littrow condition

$$\frac{m}{\sigma} = 2 \frac{\sin \theta}{\lambda} \quad (1.15)$$

So, if the angle of incidence is very low, $\tan \theta \sim \sin \theta \sim \theta$, the angular dispersion is

$$\frac{d\theta}{d\lambda} \sim \frac{m}{\lambda} \quad (1.16)$$

If m has to be small to avoid overlapping orders, then the only way of increasing the dispersion is to decrease σ , e.g. by using a larger number of grooves per mm. Alternatively, if the angle of incidence is very high, it is possible to achieve high dispersion with a low number of grooves per mm by operating in a high order. This is indeed how echelle spectrographs are designed to work, with typically $\tan \theta \sim 2$ or greater. A typical echelle grating might have ~ 80 grooves/mm, so $\sigma \sim 25\lambda$ or so for visible light. The order m has to be of order 50. Echelle spectrographs can get away with this because they cross-disperse the light and thus do not have to be operated in a particular low order to avoid overlap [15].

Gratings have a blaze angle that results in their having maximum efficiency for a particular value of $m\lambda$. Think of the grating as having little triangular facets, so that if one is looking at the grating perpendicular to the facets, each will act like a tiny mirror. It is easy to envision the efficiency being greater in this geometry. When speaking of the corresponding blaze wavelength, $m = 1$ is assumed. When the blaze wavelength is centered, the angle θ above is this blaze angle. The blaze wavelength is usually computed for the Littrow configuration, but that is seldom the case for astronomical spectrographs, so the effective blaze wavelength is typically a bit different [15].

As one moves away from the blaze wavelength λ_b , gratings fall to 50% of their peak efficiency at a wavelength on the blue side

$$\lambda = \frac{\lambda_b}{m} - \frac{\lambda_b}{3m^2} \quad (1.17)$$

and on the red side

$$\lambda = \frac{\lambda_b}{m} + \frac{\lambda_b}{2m^2} \quad (1.18)$$

Thus the efficiency falls off faster to the blue than to the red, and the useful wavelength range is smaller for higher orders. Each spectrograph usually offers a variety of gratings from which to choose. The selected grating can then be tilted, adjusting the central wavelength [15].

The light then enters the camera, which has a focal length of L_{cam} . The camera takes the dispersed light, and focuses it on the CCD, which is assumed to have a pixel size p , usually $15\mu\text{m}$ or so. The camera design often rules in the overall efficiency of most spectrographs.

Consider the trade-off involved in designing a spectrograph. For one thing, it would be great to use a wide enough slit to include most of the light of a point source, e.g. be comparable or larger than the seeing disk; but the wider the slit, the poorer the spectral resolution, if all other components are held constant. Spectrographs are designed so that when the slit width is some reasonable match to the seeing (1arcsec, say) then the projected slit width on the detector corresponds to at least 2.0 pixels in order to satisfy the

principle of the Nyquist-Shannon sampling theorem. The magnification factor of the spectrograph is the ratio of the focal lengths of the camera and the collimator, e.g. L_{cam}/L_{coll} . This could be considered a good approximation if all of the angles in the spectrograph are small, but if the collimator-camera angle is greater than about 15° , a factor of r , called grating anamorphic demagnification should be included. The factor r is defined as

$$r = \frac{\cos\left(t + \frac{\phi}{2}\right)}{\cos\left(t - \frac{\phi}{2}\right)} \quad (1.19)$$

where t is the grating tilt and ϕ is collimator-camera angle. Therefore the projected size of the slit on the detector will be $Wr L_{cam}/L_{coll}$, where W is the width of the slit. This projected size has to be equal to at least 2 pixels.

The spectral resolution is characterized as $R = \lambda/\Delta\lambda$, where $\Delta\lambda$ is the resolution element, the difference in wavelength between two equally strong spectral lines that can be resolved, corresponding to the projected slit width in wavelength units [15].

The free spectral range $\delta\lambda$ is the difference between two wavelengths λ_m and λ_{m+1} in successive orders for a given angle θ :

$$\delta\lambda = \lambda_m - \lambda_{m+1} = \frac{\lambda_{m+1}}{m} \quad (1.20)$$

For conventional spectrographs that work in low order ($m = 1-3$) the free spectral range is large, and blocking filters are needed to restrict the observation to a particular order. For echelle spectrographs, m is large ($m > 5$) and the free spectral range is small, and the orders must be cross-dispersed to prevent overlap [15].

1.2.3.1 - Optical reduction

To extract the spectra from an images taken from a long slit spectrograph, several calibration data are needed. In fact not only the data frame s themselves are necessary, but also bias frames (that allow to remove any residual bias structure), bad pixel mask (that permit to interpolate over nonlinear pixels of the CCD), dark frames (obtained with the shutter closed with the same exposition time of the data frames), dome flats (necessary to correct the pixel to pixel variation within the CCD) spectrophotometric standard stars (that are spectra of stars with calibrated flux) and comparison arcs obtained with a short exposure of a combination of discharges tubes containing HeNeAr (helium, neon, argon) [15].

For reduction the main program used is IRAF that allows to extract the data. The main steps are

1. Fit and subtract overscan: by averaging the results of the columns of the overscan.
2. Dark subtraction.
3. Interpolate over bad pixel.
4. Construct the master bias frame.
5. Apply a master normalized featurless flat by combining all the dome flat.
6. Correct the non-uniformity in the spatial direction (slit illumination function).
7. Identification of the object and sky by finding the location of the stellar spectrum on the detector
8. Wavelength calibration.
9. Extraction of the spectrum by adding all the spatial profile and subtracting the sky and then applying the wavelength solution.
10. Normalization by fitting a low order function to the spectrum in order to exclude absorption lines.

The final results is a spectra like the one shown in figure 1.14.

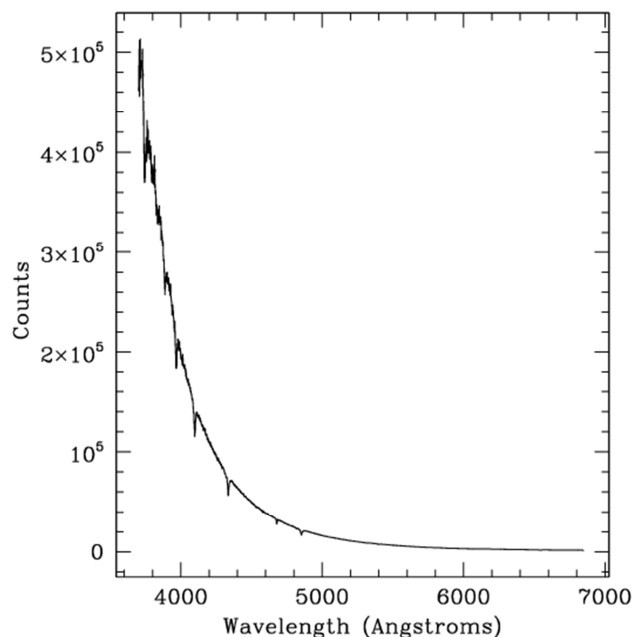


Figure 1.14 – spectra of a star after normalization [15]

This technique has been adopted not only to study the physical composition of the stars but also for identifying space debris. Lederer et al. [21] describes the results obtained by the comparison of the spectra obtained for a space debris (IDCSP) and the laboratory test for solar panels. The spectroscopy of the IDCSP resulted most similar to solar cell exanimated; however this cell was manufactured in the 1990s whereas the IDCSPs were designed and built in the 1960s, thus an identical match was not expected.

Also for the analysis of near-Earth objects (NEOs) a similar technique has been adopted during the MIT, University of Hawaii and the NASA IRTF joint campaign for reconnaissance of specific subsets of the NEO population conducted by professor Richard Binzel [22]. The main goal have been to measure the spectral characteristics of NEOs having propulsion requirements < 7 km/sec, characterize the properties of objects in comet-like orbits for understanding asteroid-comet connections and characterize the potentially hazardous asteroid subgroup and to specifically compare with the broader NEO population to understand better meteorite sources. The obtained spectra for NEO MN4 is shown in figure 1.15.

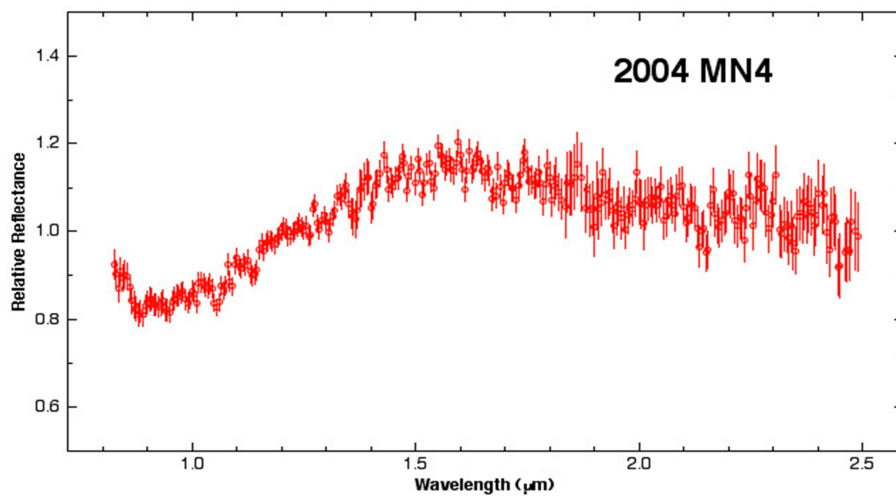


Figure 1.15 – Spectrum NEO MN4 [22]

Chapter 2

ALMASCOPE at Broglio Space Center in Kenya

Due to the need to avoid collision between operative satellites and orbital debris, observation campaigns are continuously by all the space agencies. I had the opportunity to participate in a test campaign for the installation of an Italian observatory fully dedicated to space surveillance. Aim of the campaign was the evaluation of the system performance from the Malindi Broglio space center site.

In this chapter a system for orbital object monitoring is analyzed, based on a mid-latitude and an equatorial observatory. Compared to the use of a single telescope located at mid latitude, improvements in space debris detection and tracking were observed in surveying volume, object identification and orbital determination accuracy. The need to improve observation performances in monitoring and cataloguing these objects is constantly increasing, due to the constant growth of operative satellites and space debris in both GEO and LEO regions [24].

The best accuracy in terms of orbit determination and space debris environment survey can be achieved by merging optical and radar measurements ([25], [26]), but the absence of dedicated radar transmitters at the disposal of space debris survey activity on a routine basis, precludes employing this type of solution. Thus, in order to increase the space debris observation capabilities, the opportunity to establish a network of observatories outside Europe has been examined. In fact the idea of an observatory for space debris located in Equatorial Africa could significantly improve the Italian and European capability to provide support to operative spacecraft both in LEO and GEO impact risk management and in orbital maneuvers measurement. For these reasons a dedicated optical campaign was performed to demonstrate that it could effectively permit to increase the Italian monitoring capability in any orbital regime and inclination [24].

The Malindi Italian Observatory is complementary to observatories located in Europe and it is well suited to realize an integrated system to improve the Orbit Determination capability of HEO (High Earth Orbit) objects by performing simultaneous or consecutive observations from two different sites. It allows an increase the arc of observable trajectory, also permitting to realize different geometrical configurations. Moreover, an equatorial Observatory would permit to track LEO or re-entering high inclination objects over

longer orbit arcs. The same object could be tracked consecutively by observatories located in Africa and in Europe, thus increasing the accuracy of achieved orbital parameters. This can be useful in evaluating the impact probability related to close approaches ([27], [28], [29], [30]) and in evaluating the impact points of re-entering objects. Both observatories would permit to increase the European space surveillance capability by achieving data from sites with different meteorological conditions, obtaining less sparse measurements from longer orbit arcs and facilitating the orbit determination and tracklets correlation [31].

2.1 – The ALMASCOPE observatory

The main features of the observatories considered are based on the characteristics of the ALMASCOPE (ALMA mater studiorum university teleSCOPE) observatory. This observatory, established in 2009, is an Italian observatory fully dedicated to space surveillance [24] that participated in IADC (Inter Agency Space Debris Coordination Committee) coordinated campaign.

The observatory is based on a commercial off-the-shelf mount, similar to the one used for the FIRST (First Italian Russian Space Debris Telescope) observatory [32], realized in June 2009 and located at Colleparado (Frosinone - Italy). The telescope is a 25 cm f/4 in Newtonian configuration and the CCD is based on a Kaf1600E sensor, which has an array of 1024x1536 pixels, each pixel is 9x9 micron (total chip size 9.2x13.8mm). The system instrumental accuracy for astrometry is about 2 arc-sec. The telescope field of view is of about 1°. The lightness and the fastness in motion, together with high image downloading speed make the proposed solution suitable for tracking space debris as well as for performing complex searching grids for space debris surveys. This observation system proved to be effective also for spent upper stages attitude determination, based on light curve measurements [33]. The ALMASCOPE is shown in figure 2.1.



Figure 2.1 – ALMASCOPE at the Broglio Space Center [24]

A main component of the whole system is the software for image processing and this point has been stressed in literature ([34], [35], [36], [37]). The software used for image processing has been developed to permit the complete automation of the observatory. The debris identification can be performed by the analysis of images both with point like stars or with stripes like stars. The logic of the procedure is shown in figure 2.2. A first check is performed to verify the image integrity; then the image is converted into black & white so that the pixel value is 0 (black) or 1 (white). An algorithm provides the retrieval of stretched objects: the image is discarded if more than 10 objects of this shape are found (this situation was usually due to the motion of the telescope during the shutter opening). On the contrary, if a smaller number of stretched objects is found the image is stored and analyzed for track identification. The image analysis routine is the core of the process. The image analysis algorithm performs two main tasks: the detection of lighting tracks within an image, and the cataloguing of tracks into two classes: moving objects (debris), and static objects (stars). Identified objects are further analyzed by evaluating magnitude and by comparing them with the database of catalogued objects in order to detect their nature (Correlated –CT, Uncorrelated – UCT). The last step, to validate the system, is the analysis of unseen objects; in other words it is obtained the number of objects that even if in the field of view according to the catalogue, were not identified [24].

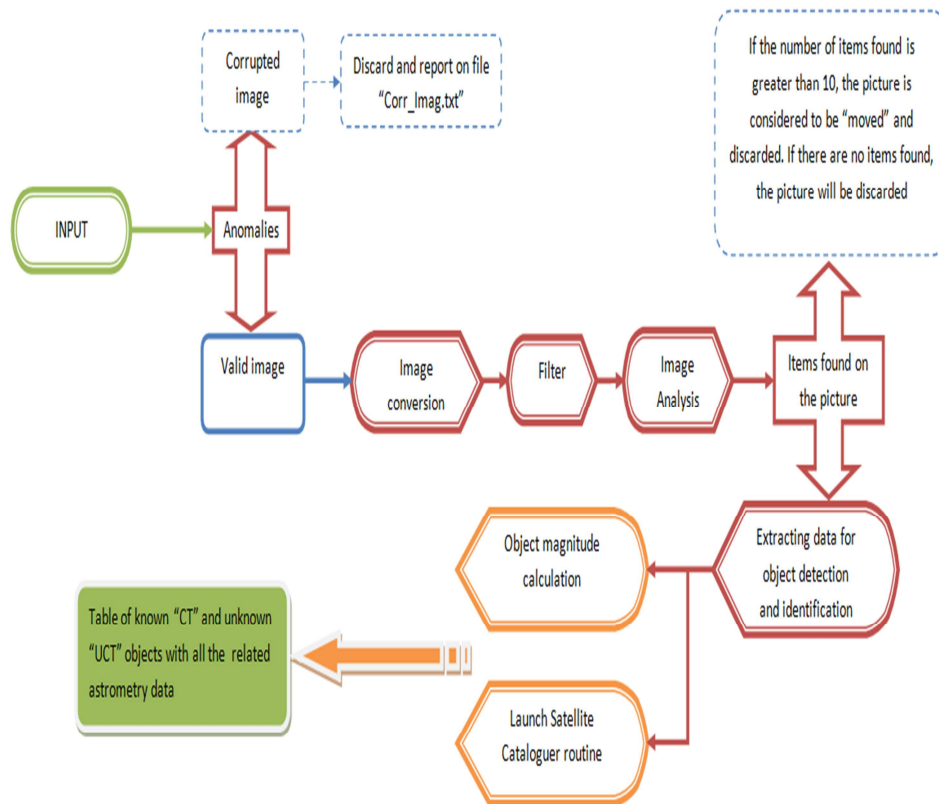


Figure 2.2 – Image analysis software general layout [24]

The Broglio Space Centre (BSC) in Malindi (Kenya) is managed by the Italian Space Agency. The base is situated on the coast of the Indian Ocean (40.19°E, 2.99°S). It consists of two segments, the marine segment represented by the launch oceanic platform and the earth segment for the telecommunication center. Thanks to its equatorial location, the base is well suited for Earth based space surveillance activities.

There are some specific features that make the use of two jointly operated observatories in Italy and in Kenya potentially profitable, including the percentage of usability during the year and the geometry of observations in terms of sun-satellite-observer positions for mid to high inclination orbits. Observatories located in Italy and in Kenya are complementary under the aspect of percentage of usability during the year, in terms of cloud coverage and rainfall. The seasonal cloud coverage percentage, shown in Table 2.1, and the average rainfall per month, shown in figure 2.3, validate the suitability of an observatory located in Malindi during wintertime and of an observatory located in Italy during summertime. Two periods around March and around August are suitable for performing joint observations.

Table 2.1 [39]

Seasonal cloud coverage percentage

	Winter	Spring	Summer	Autumn
Rome	60%	50%	20%	60%
Malindi	40%	30%	50%	30%

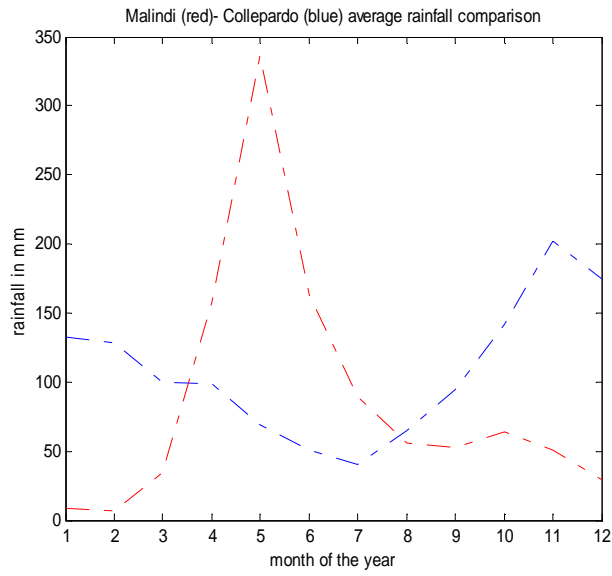


Figure 2.3 – Comparison of the average annual rainfall between Malindi and central Italy [39]

The daylight analysis shows that situations exist, in which both sites are close to the terminator and could observe a passing LEO object during the same orbit. These particular conditions arise close to sunset in wintertime and close to sunrise in summertime as visible in figure 2.4. The terminator shape during equinoxes does not make it possible to have both stations in darkness during the same LEO object orbit. In such a case successive orbits must be considered necessarily.

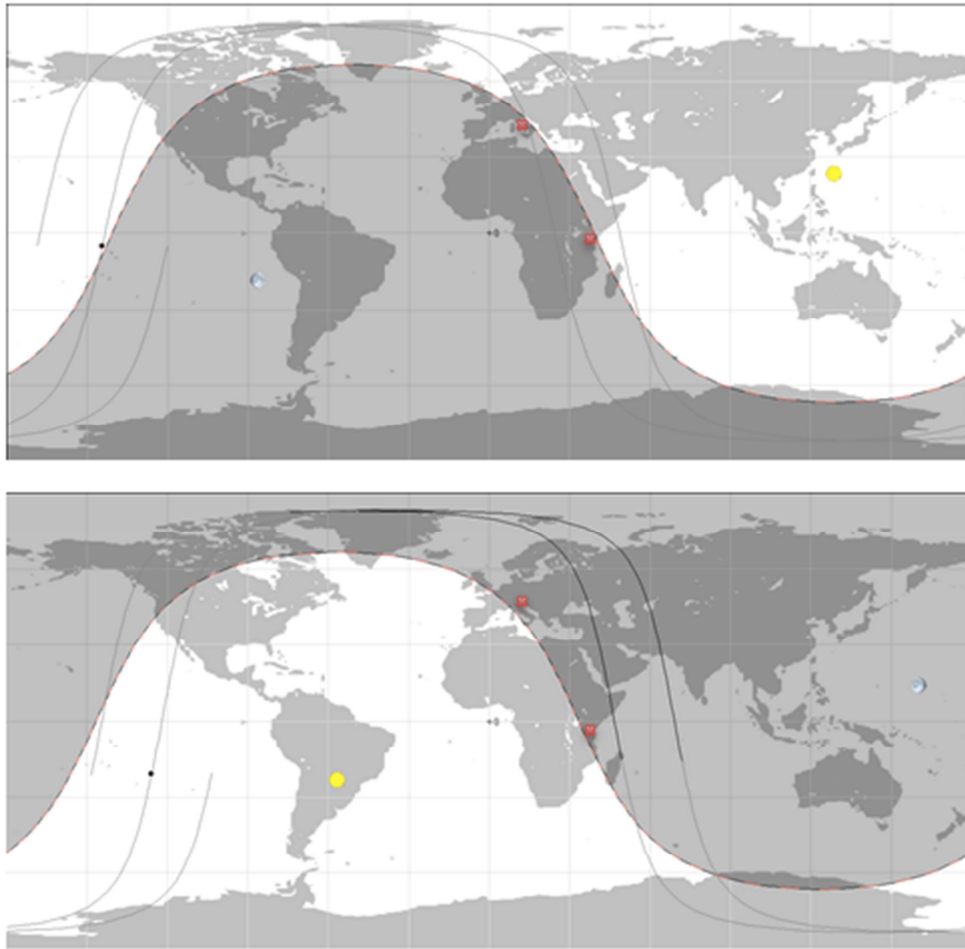


Figure 2.4 – Terminator position and shape in summertime sunrise (Top) and in wintertime sunset (Bottom), the crosses mark the Italy and Malindi position [36]

2.2 – The Malindi test campaign

In order to verify the effectiveness of the Equatorial observatory, a three-week test campaign was carried out from the Malindi Base in September 2010, using the ALMASCOPE observatory.

The main purpose was to verify the quality of measurements and to collect data suitable for performing numerical simulations of the joint mid-latitude and equatorial observations. The observation campaign was carried out from two different sites within the Broglio Space center: the first one inside the base camp and the second one from the SAN MARCO off-shore platform, located 5 miles away from the coast (figure 2.5). The light pollution is extremely low from the platform while inside the base camp it is present, even if low. The observation campaign showed that the seeing was acceptable for space debris observations, moreover

it should be noticed that it is extremely variable with the seasonal effect and close to sea level, it was estimated at about 4'' in September which is the wet season, the seeing improves during the dry season.

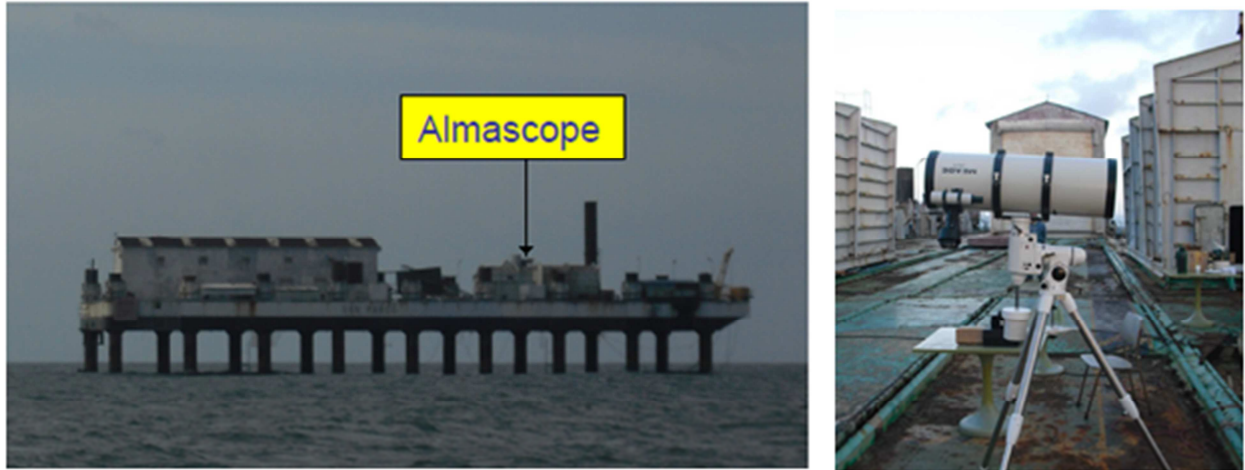


Figure 2.5 – Observatory on the SAN MARCO platform

2.2.1 - Observation campaign statistical results

During the three observation weeks I collected several measurements in order to compare achievable results from Malindi sites with a standard survey campaign performed from Northern hemisphere observatories. The histogram in figure 2.6 shows the number of pictures taken for each night. The average observation time was about 5 hours, excluding the three rainy nights of 15th, 16th and 19th September, with more than 1000 picture collected per night. The number of images and of observation hours as well as the frequency of objects occurrences is comparable to standard IADC observation campaign [23]. Hence the site seems to be suitable for effective optical observations, on a continuous basis [24].

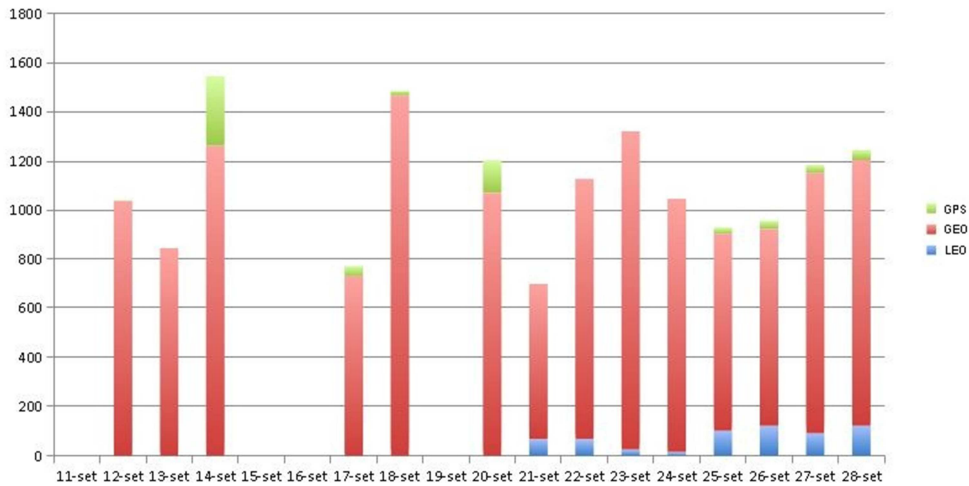


Figure 2.6 - Number of pictures taken per night [24]

The diagrams presented in figure 2.7 show the percentage of pictures taken in the three target regions LEO, GEO and MEO. Most of the pictures concern the GEO region because the GEO survey occupied the instrumentation for the largest number of hours per night.

For this kind of campaign a strategy pointing at performing a statistical survey was implemented. During the first week of the observation campaign the GPS region was observed, beside the GEO, to collect useful calibration data of the instrumentation and image analysis procedures. During the last week the LEO region was also observed.

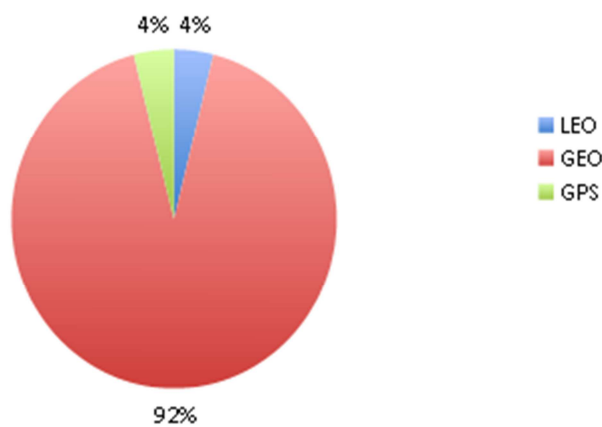


Figure 2.7 – Target regions percentage and number of pictures taken [24]

The observed fields of view in terms of topocentric right ascension and declination are represented in figure 2.8 with respect to the distribution of the geosynchronous catalogued objects. Many fields lay on the geostationary ring, others have different inclination for the search of uncatalogued objects.

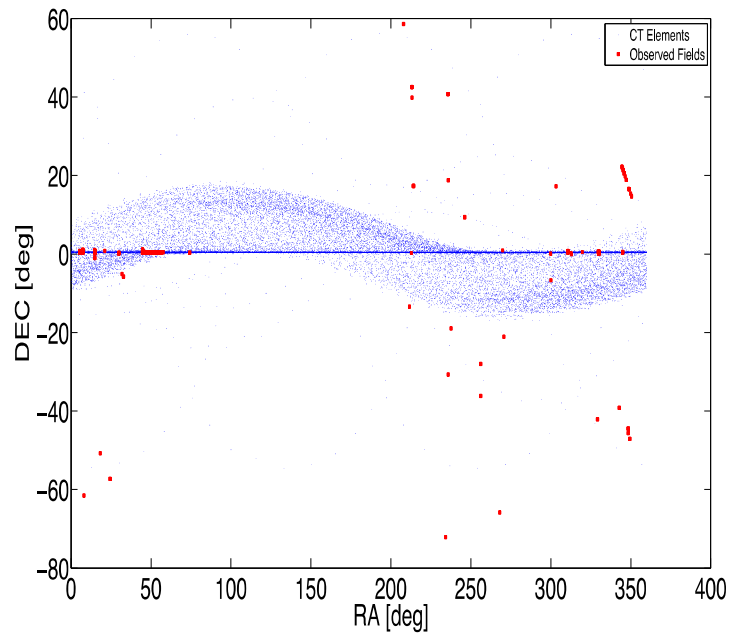


Figure 2.8 – Fields of view of the observation campaign [24]

The differences of orbital regimes observed are evident from the semimajor axis-eccentricity graph outlined in figure 2.9. In this graph all the catalogued objects observed are grouped in clouds indicating different orbital regimes.

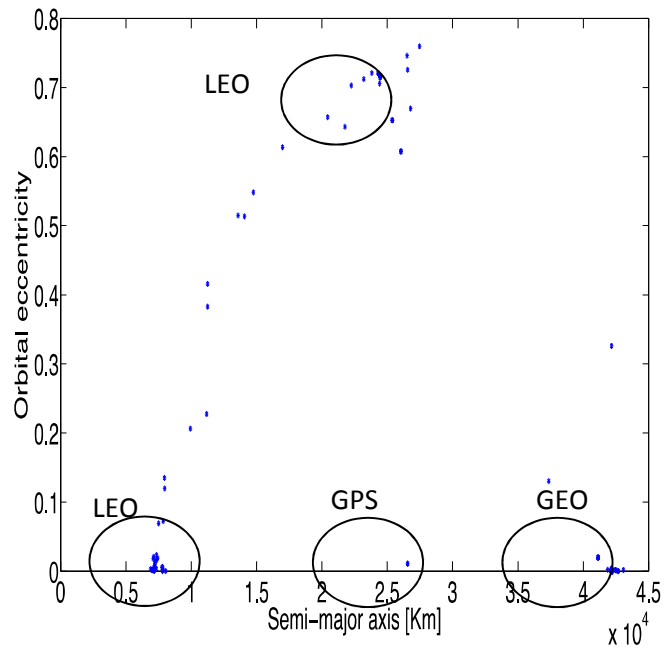


Figure 2.9 – Semimajor axis – Eccentricity of the observed objects [24]

The RAAN-Inclination distribution of objects in the geosynchronous region is shown in figure 2.10. It respects the usual shape of the RAAN-inclination graph appears [31], confirming that the achieved data are comparable with literature standard data and the system is suitable for standard surveys.

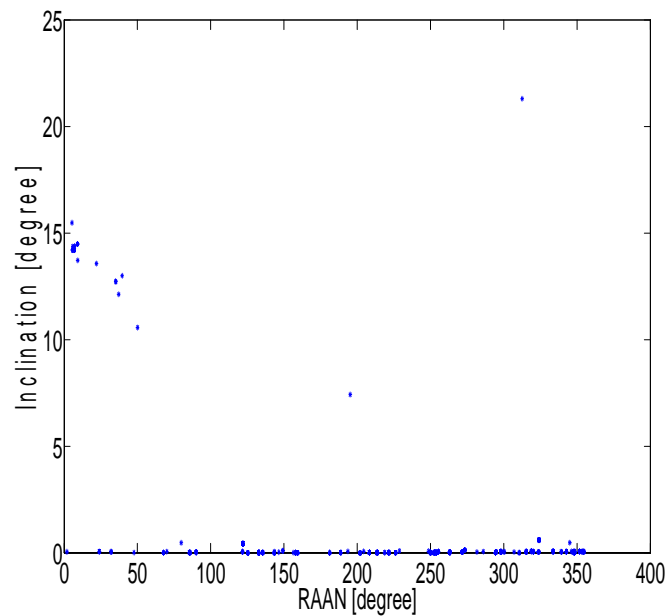


Figure 2.10 – RAAN-Inclination distribution of the objects observed in geosynchronous region [24]

The total number of tracklets taken during this campaign are shown in figure 2.11, indicating those recognized as objects Catalogued in the NORAD Two Line Elements catalogue (CT) and Uncatalogued objects (UCT). The UCT tracklets are about one third of the CT. The tracklets position for cataloguing purposes was assessed from the image center position given by the mount. In this case an accuracy of about 5' is considered, mainly due to the system alignment error. Also the percentage of UCT and CT objects fulfills with standard observation campaign result [23].

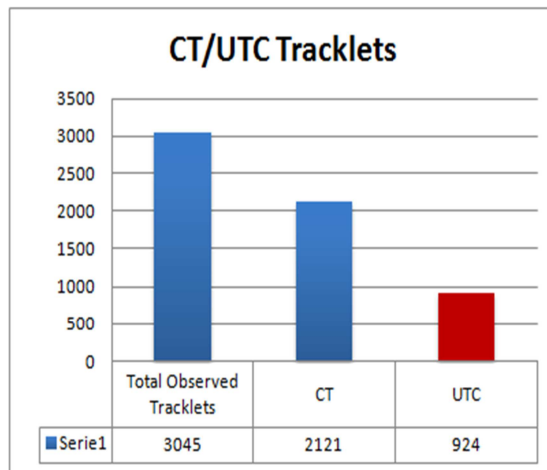


Figure 2.11 – Tracklets of catalogued and uncatalogued objects during the observation campaign performed at the BSC [24]

Chapter 3

The Loiano campaigns for physical characterization of space debris

In 2011 a pilot program for the physical characterization, through photometric measurements, of the space debris population in high Earth orbits was started and has gone on since then at the 152cm G.D. Cassini Telescope in Loiano, operated by the *INAF Astronomical Observatory* of Bologna, Italy [42]. I had the opportunity to participate in this program which is coordinated by CNR in cooperation with *Italian Space Agency (ASI)*, *University of Bologna* and *University La Sapienza* in Rome by implementing the observation strategies on the basis of objects to observe orbital characteristics and keeping into consideration the observatory constraints, moreover I carried out the observation campaign collecting measurements and participating in data analysis examination.

Dedicated optical observation campaigns are achieved to characterize the environment in the GEO region because the population of debris is still partly uncertain. In fact the GEO region is one of the most crowded orbits since its particular characteristics are suitable to a huge number of commercial mission. The widespread exploitation of this orbital region in the last fifty years has created a large number of objects that will pollute this region for the following centuries. The long term dynamics of these objects shows that their motion is limited to a *thorus* encircling the geostationary ring with a periodic change of the equatorial inclination. This motion is essentially driven by the presence of third bodies (e.g. the Sun, the Moon), Earth asphericity and solar radiation pressure environmental perturbations. The effect of solar radiation pressure in particular, in fact it seems to be the main responsible for the creation of a peculiar population of space debris, having mean motion around 1 and high eccentricity, recently discovered by the ESA OGS telescope [45]. It was shown that these objects have a very high area to mass ratio (HAMR) [46] and probably these objects are fragments of thermal blankets or multi-layer insulation (MLI) which had separated from aged spacecraft or been ejected by explosive fragmentations of spacecraft. At the present their exact nature, as well as, the nature of many space debris in GEO, remains currently elusive due to lack of physical, spectroscopic studies.

3.1 – The G.D. Cassini Observatory

All the observations were performed from the Loiano observatory (figure 3.1), located near Bologna ($44^{\circ} 15' 33''$ N, $11^{\circ} 20' 02''$ E) at the elevation of 785 m. The observatory is located in a quite dark region, with a reduced light pollution, the average measured seeing all year round being about $2''$.



Figure 3.1 – G.D. Cassini Observatory, main dome

The telescope used is a 152 cm diameter Ritchey-Chretien configuration, system with $f/3$ at the primary focus and 8 at the secondary. The telescope, shown in figure 3.2, has an English mount and can only track in sidereal mode. This represents a serious limit of the system for our purposes, since the absence of differential tracking does not allow the continuous tracking of drifting objects (e.g. HAMR objects), thus reducing the time the objects are in the spectrograph slit.

In figure 3.3 the telescope and CCD controlling station is shown.



Figure 3.2 – Cassini Telescope



Figure 3.3 – Telescope and CCD controlling station

The telescope is equipped with BFOSC (Bologna Faint Object Spectrograph and Camera) [47], a multipurpose instrument for imaging and spectroscopy, with an EEV CCD (1340x1300px) capable of covering a field of view of 13'x13'. This is an instrument designed to be used both as spectrograph and as imaging system. The configuration used for taking spectra of observed objects includes a 2'' slit (large enough to permit a longer object dwelling time in the field of view) and a grism essentially focused on the visible light, whose efficiency is shown in figure 3.4.

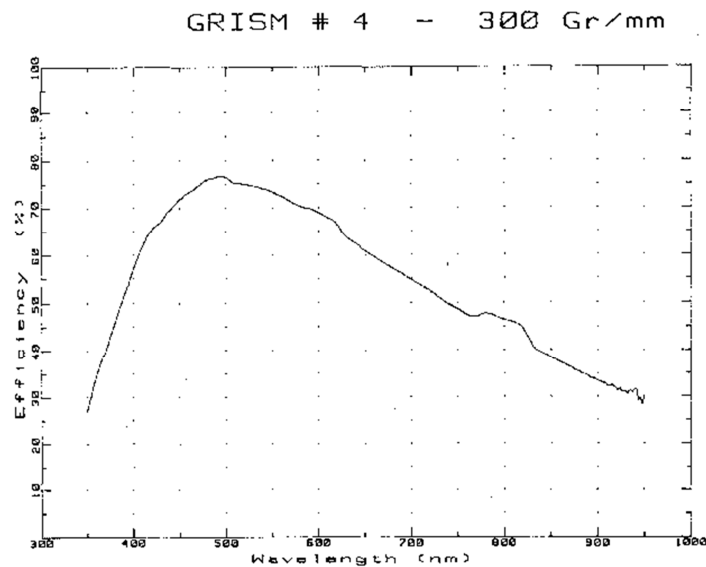


Figure 3.4 - Characteristics of the grism#4 used for orbital objects spectra [47]

3.2 - Observation nights

Seven nights were scheduled in February, April and August 2011 but only five were sufficiently photometric to perform observations. The number of pictures taken and the number of hours of observation performed are shown in figure 3.5. The number of pictures taken is related to the kind of targets acquired while the number of observing hours is strictly related to sunset and sunrise time (in fact during summer the observation nights are shorter).

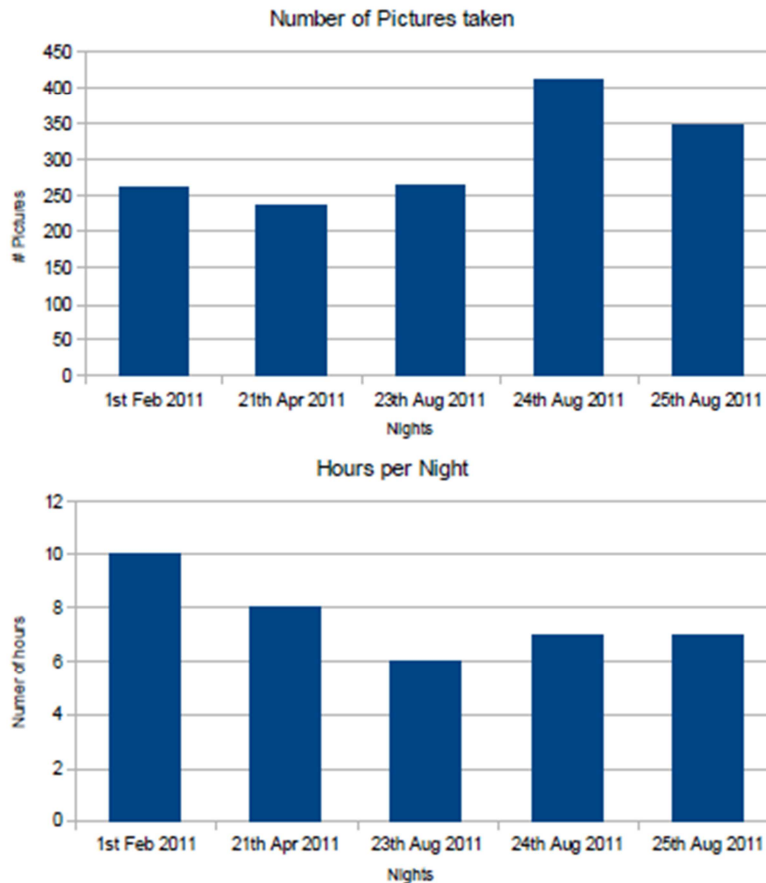


Figure 3.5 – Number of pictures taken and hours per night [43]

The strategy for performing the pilot observation campaign implied the observation of operative spacecraft and upper stages to achieve data to be used for comparison with data achieved from HAMR objects. Orbital parameters for such objects were made available from the ISON group International Scientific Optical Network (ISON) group of the *Keldysh Institute of Applied Mathematics* of the *Russian Academy of Sciences* for the April nights and from the *NASA Orbital Debris Program Office* for the April and August nights. GPS satellites were observed for timing calibration. A standard photometric sequence consists of repeated observations in each of the B-V-R-I filters repeated until a sufficient photon count was reached for each object ([42], [43]).

A summary of observed objects is sketched in figure 3.6. It is noticeable how the HAMR objects were observed in the last nights when a sufficient number of data on well-known spacecraft were collected.

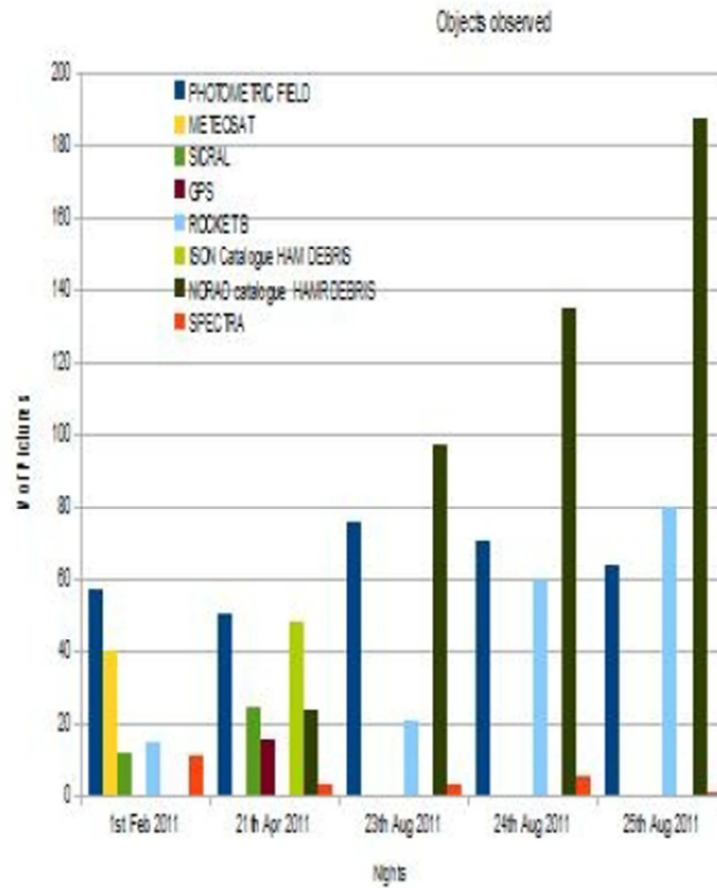


Figure 3.6 - Observed objects during the pilot observation campaign [43]

I implemented observation strategy adapt to achieve, for all the objects in the list, multi-band photometric observations. It should be noticed that the high instability of orbit of HAMR objects [40] make them very difficult to observe and track..

Table 3.1 summarizes the objects considered.

Table 3.1
List of observed objects

Name	Type of object	Epoch of observation
Meteosat 7	GEO Satellite	February 2011
Meteosat 9	GEO Satellite	February 2011
SICRAL 1	GEO Satellite	February 2011
SICRAL 1B	GEO Satellite	February and April 2011
SL12 28240	Rocket Body	February and August 2011
SL12 26397	Rocket Body	February 2011
SL12 13983	Rocket Body	August 2011
SL12 28256	Rocket Body	August 2011
90085	HAMR object	April 2011
95452	HAMR object	April 2011
84983	HAMR object	April 2011
84964	HAMR object	August 2011
84967	HAMR object	August 2011
84980	HAMR object	August 2011
84993	HAMR object	August 2011

3.3 – Data processing

The CCD images were reduced and calibrated with a standard method plus the addition of some ad-hoc procedures to correctly handle the more peculiar ones, showing strong fast and irregular variations in magnitude [42]. Bias and flat-field corrections were performed: a master flat field was computed as a median of several dome flat fields. The instrumental magnitudes were measured using aperture photometry with an integrating diameter typically about six times the FWHM.

This was considered optimum since it is large enough to include most of the point spread function, yet small enough to minimize background sky noise. Source detection and sky subtraction were performed using the *SEXtractor* software package ([48], [49]). For peculiar objects (like some of the HAMRs) the IRAF task *polyphot* was used. This task allows to perform aperture photometry using a polygonal aperture whose vertex are user defined. 4 or 6 vertex were used, according to the kind of object, e.g., large enough to include the whole objects without considering too much sky background. For every object the same aperture was always used.

For magnitude calibration, observations of different standard stars [50] were obtained over a wide range of airmasses and stellar types. A quality check on the stars is performed mainly to be sure that they are not saturate, the S/N is larger than 100 and the effective airmass at the exact epoch of the image is used (i.e., not the one at the beginning of the exposure). The zero point, and color terms obtained from the Landolt fields were then used to convert instrumental magnitudes to apparent magnitudes. B and V filters have been calibrated using the B-V color; the R filter has been calibrated using the V-R color; the I filter has been calibrated using the R-I color. The color terms calibration of the HAMR data was particularly cumbersome due to the large variations observed. A multi-step averaging procedure was performed to obtain the average colors from the single calibrated magnitudes [24].

The errors quoted take into account both the instrumental errors given by photon statistics alone and the calibration errors.

3.3.1 – Reflectance

Once the magnitudes at different wavelengths are computed, the reflectance values at each wavelength can be obtained using the following equation:

$$R(\lambda) = 10^{-0.4[(M_F - M_V) - (M_F - M_V)_\odot]} \quad (3.1)$$

where (M_F) and $(M_F)_\odot$ are respectively the magnitudes of the object and the Sun at the central wavelength of filter F (specified to be BVRIJHKs). The equation is normalized to unity at the central wavelength of filter V using M_V and $M_{V\odot}$, i.e., the V magnitudes of the object and the Sun [42].

3.4 – Results

3.4.1 – February and April 2011

During the observing nights in February and April 2011, multi-band photometric observations were performed ([42], [43]). Unfortunately the images of SICRAL 1B taken in February were not exploitable. The

HAMR objects 95452 and 84983 turned out to be too faint and too fast moving for our sensor, so no exploitable data was found in the images. The list of the objects observed in the February and April nights for which exploitable data were recorded is seen in table 3.2.

Table 3.2
List of observed objects

Name	Type of object	Epoch of observation
Meteosat 7	GEO Satellite	February 2011
Meteosat 9	GEO Satellite	February 2011
SICRAL 1	GEO Satellite	February 2011
SL12 28240	Rocket Body	February 2011
SL12 26397	Rocket Body	February 2011
90085	HAMR object	April 2011

Figure. 3.7 and 3.8 show the distribution of the color indexes of the observed objects. In particular in figure 3.7 the B-R vs. B-V index is shown, while in Fig. 3.8 the R-I vs. B-R distribution is shown.

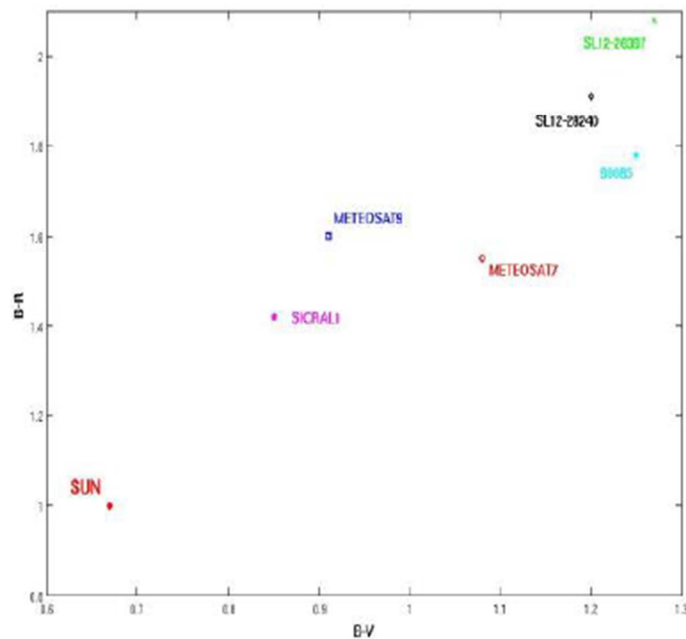


Figure 3.7 – Photometric B-R vs. R-V color indices. The full red circle marks the position of the Sun at B-V = 0.67 and B-R = 1 [42]

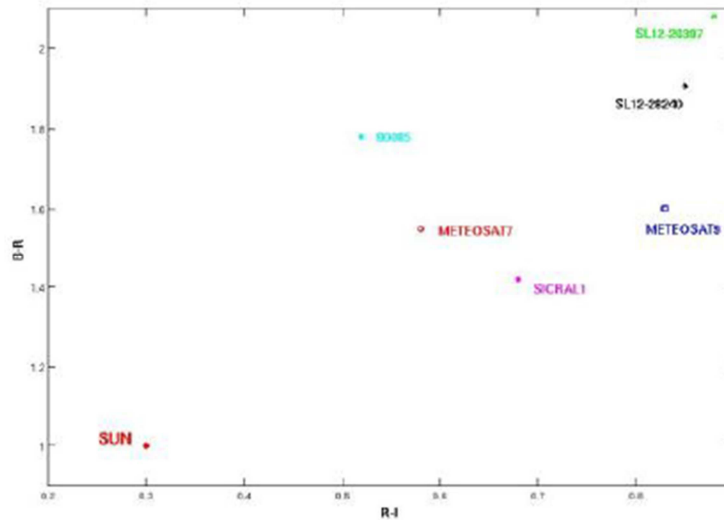


Figure 3.8 – Photometric B-R vs. R-I color indices. The full red circle marks the position of the Sun at R-I=0.3 and B-R = 1 [42]

Note that in figure 3.8, the bluest objects are at the lower left, and the reddest objects at upper right. So it can be noticed how the objects are all redder than the Sun.

Using Eq. (3.1) the normalized reflectance of the objects was calculated. From figure 3.8 it is possible to notice how the two rocket bodies are significantly redder than the other objects. Perhaps it comes as a surprise the fact that also Meteosat9 appears quite red and significantly different from its twin spacecraft Meteosat7. The Meteosats are cylindrical satellites covered with solar cells, so we would deem the reflectance of Meteosat7 more typical of this class of satellites. While the most probable explanation for this discrepancy is a possible problem with the data analysis (calibration) it is worth noting that actually Meteosat7 and Meteosat9 belong to two different generations of Meteosats and are placed on orbits with significantly different inclinations (which might be responsible for different aspect angles) [42].

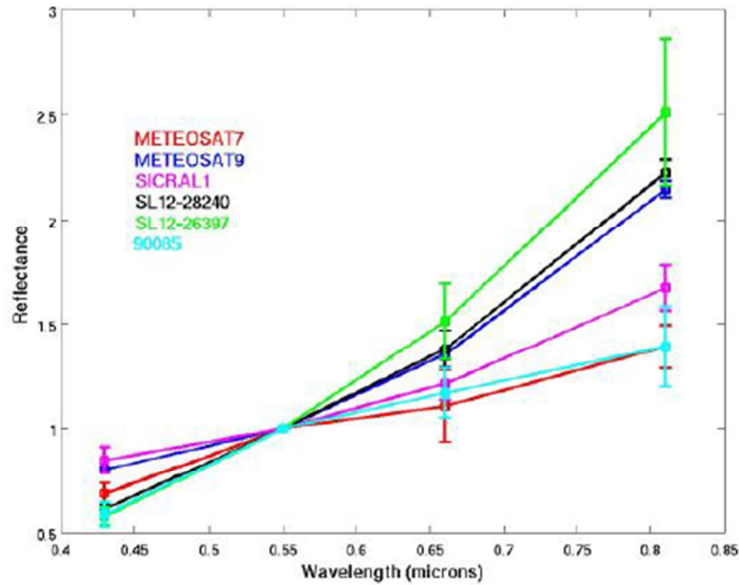


Figure 3.9 – Normalized reflectance values data from the February 2011 [42]

Comparing obtained results with the available literature, it is possible to notice how observed objects would mix with the bulk of the objects observed by Seitzer et al. [51]. Cowardin et al. published a set of laboratory photometric data for a series of orbital debris targets [52]. Comparing figure 3.7 with figure 3.10 and 3.11 from Cowardin [52], it is possible to notice that the three intact satellites lie in the region where most of their sample are located (in particular solar cell samples). On the other hand the two rocket bodies and the HAMR object 90085 are located in a region where no measurements are given by the authors for the B-R versus B-V color indexes. By examining figure 3.12. 3.13 from Cowardin [52], it becomes apparent that all our objects lie close to the two GEO objects they observed. In particular 90085 is very close to the Mylar sample analyzed by them. This could point to a possible composition determination for 90085.

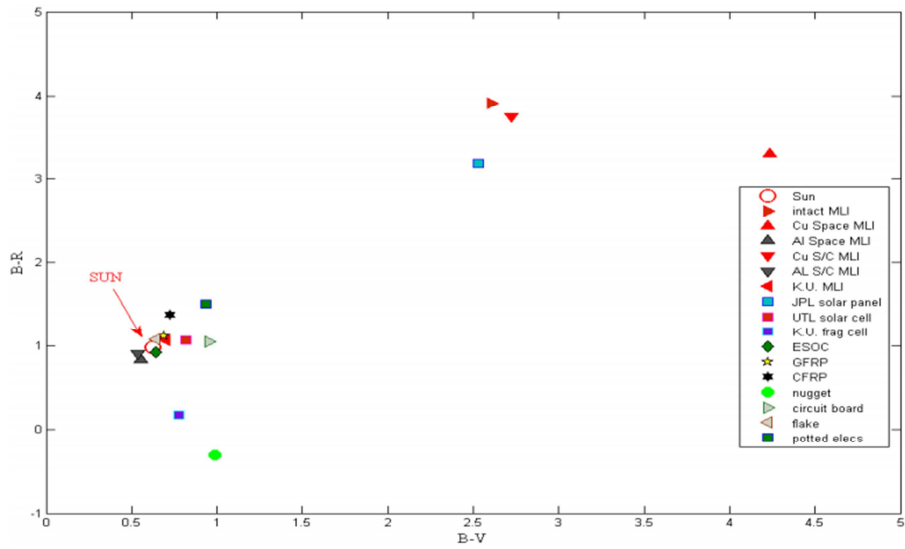


Figure 3.10 – Photometric B-R vs. B-V color indices for all fourteen laboratory fragments [52]

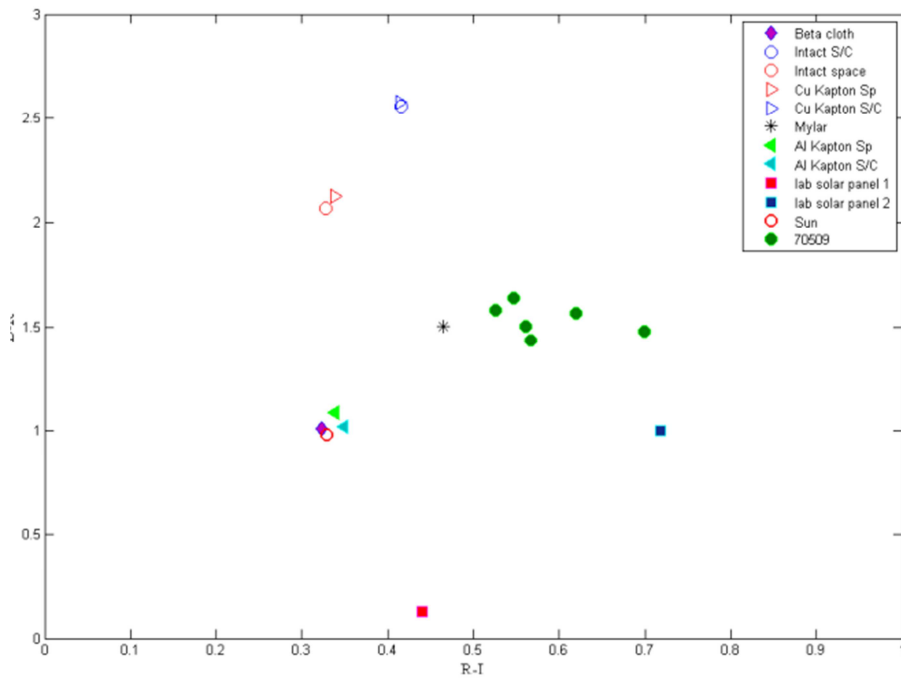


Figure 3.11 – Spectroscopic color indices with stable GEO object [52]

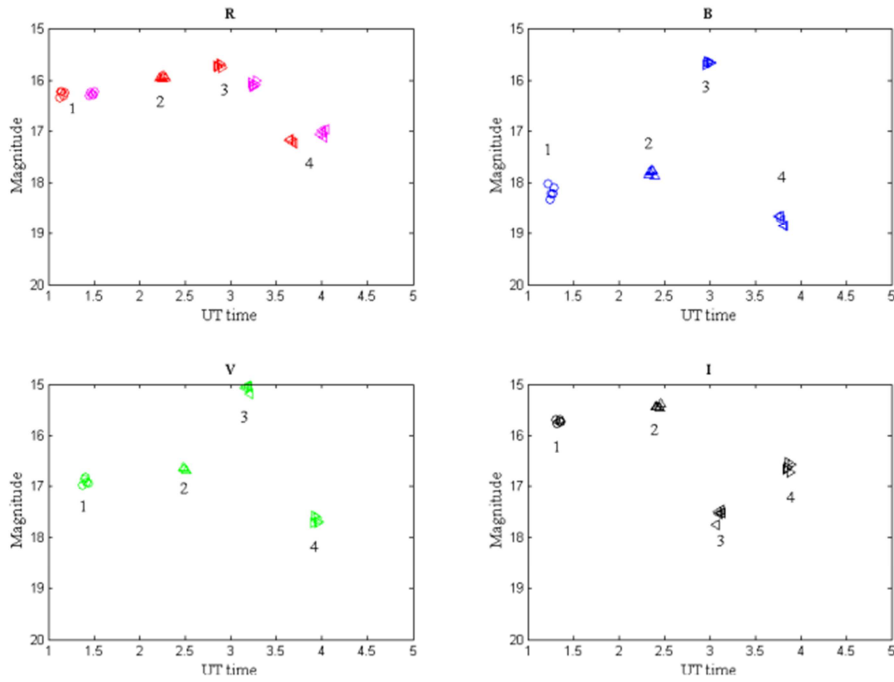


Figure 3.12 – Four sequences of filter photometry acquired by CTIO 0.9 m on GEO object [52]

In Figure 3.12 the GEO object is stable on short time sequences (5-20 min), but on longer time scales the object appears to brighten in the B and V filter, and decrease in the R and I band at approximately same time. This type of behavior is also seen in the laboratory when the copper-colored Kapton rotates toward the aluminized Kapton face with single layers of MLI. The magnitude changes from peaking in the R to peaking in the Bor V, respectively [52].

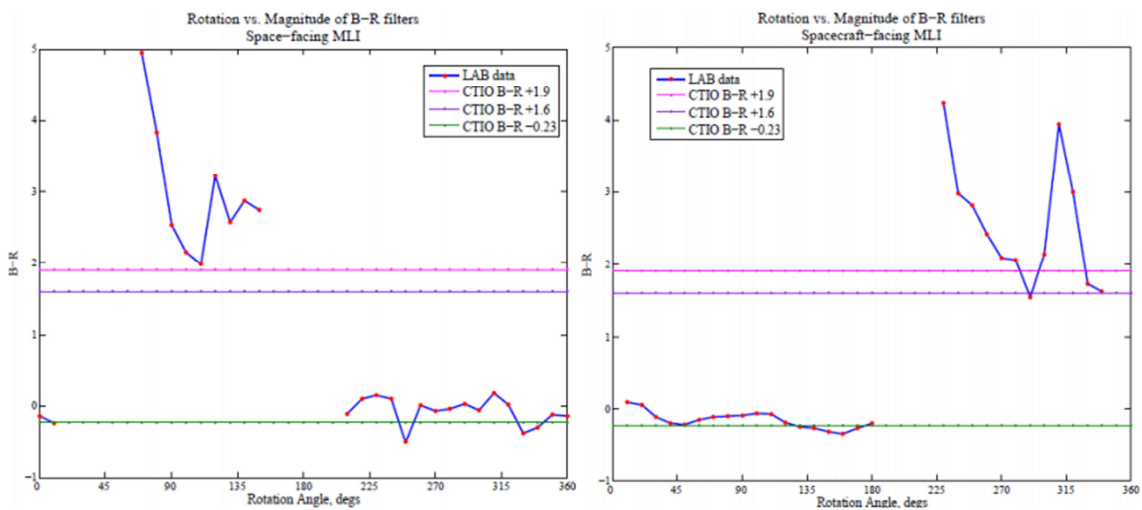


Figure 3.13 – B-R over all rotations for space-facing MLI (copper-colored Kapton illuminated first, followed by aluminized Kapton on left) (aluminized Kapton illuminated first, followed by copper-colored Kapton on right) over plotted with telescopic B-R. [52]

3.4.2 – August 2011

During the observing nights in August 2011, multi-band photometric observations were performed. The list of the objects observed in the August nights for which exploitable data were recorded is presented in Table 3.3.

Table 3.3
List of observed objects

Name	Type of object	Epoch of observation
SL12 28240	Rocket Body	August 2011
SL12 13983	Rocket Body	August 2011
SL12 28256	Rocket Body	August 2011
84964	HAMR object	August 2011
84967	HAMR object	August 2011
84980	HAMR object	August 2011
84993	HAMR object	August 2011

Figure 3.14 show the distribution of the B-R vs. B-V index while in 3.15 the R-I vs. B-R index are shown. The magenta diamonds denote to the objects observed in the February and April 2011 runs. The red squares and the blue circles refer to the objects observed, respectively, on August 24 and August 25 2011. Some of the objects were observed in multiple nights mostly to check consistency between the measurements and also possible physical variations.

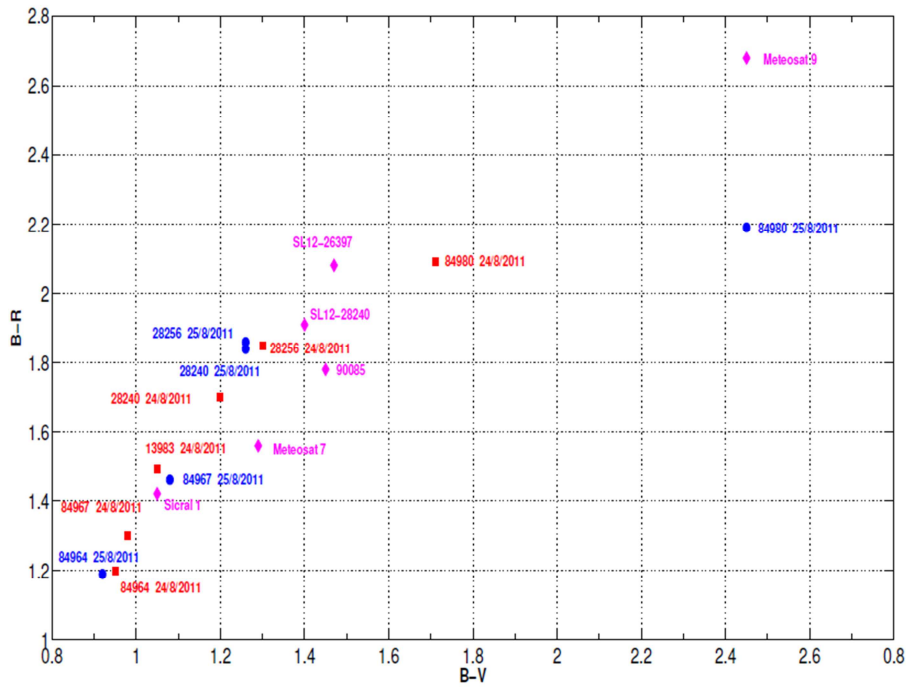


Figure 3.14 – Photometric B-R vs. B-V color index [44]

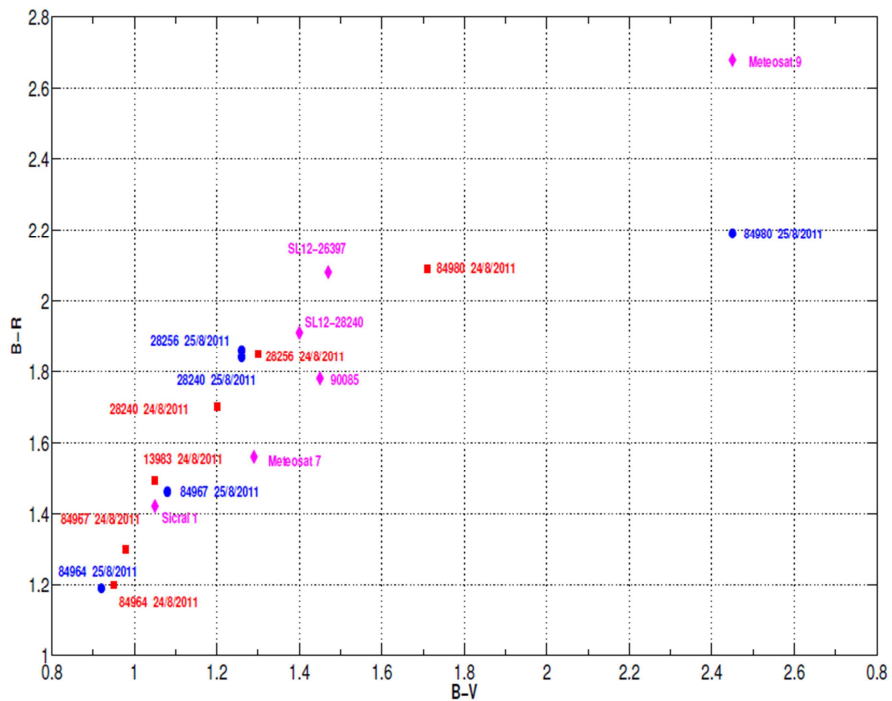


Figure 3.15 – Photometric B-R vs. R-I color indices [44]

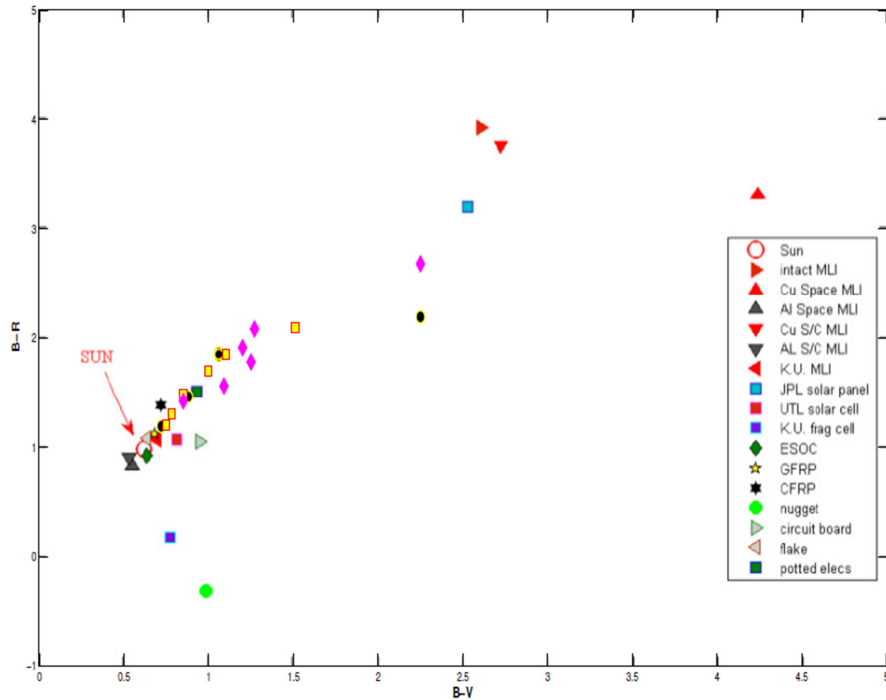


Figure 3.16 – Photometric B-R vs. B-V color indices of target superimposed to the figure 3.9 [44]

Once again, in figure 3.16 data collected at Loiano Observatory has been superimposed on figure 3.10 from Cowardin [52]. It can be noticed how all the objects lie within the main group of the laboratory sample analyzed by Cowardin. This is an indication of the consistency of our data and gives an indication of the possible physical nature of other objects.

The plots of reflectance for the objects observed on 24th and 25th August 2011 are shown in figures 3.17 and 3.18 respectively. It is immediately apparent how the objects divide into two distinct groups with different slopes. The rocket bodies have a distinctly higher slope compared to the HAMR objects. This behavior makes us confident that the reflectance, as computed from Eq. (3.1) is consistent and is probably indicative and directly related to the different materials that cover the two classes of objects: mostly MLI-like materials for the HAMR and probably more “classical” compositions for the rocket bodies.

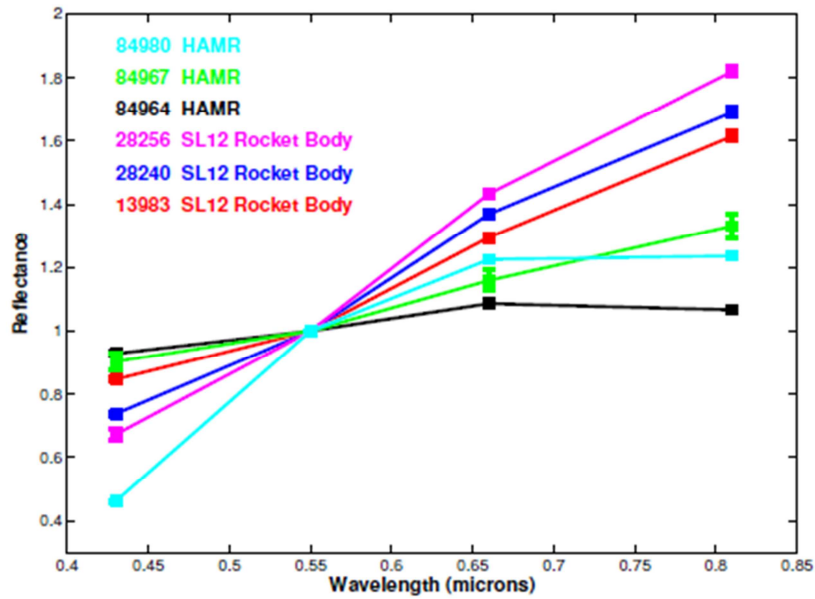


Figure 3.17 - Normalized reflectance of the objects observed on 24th August 2011 [44]

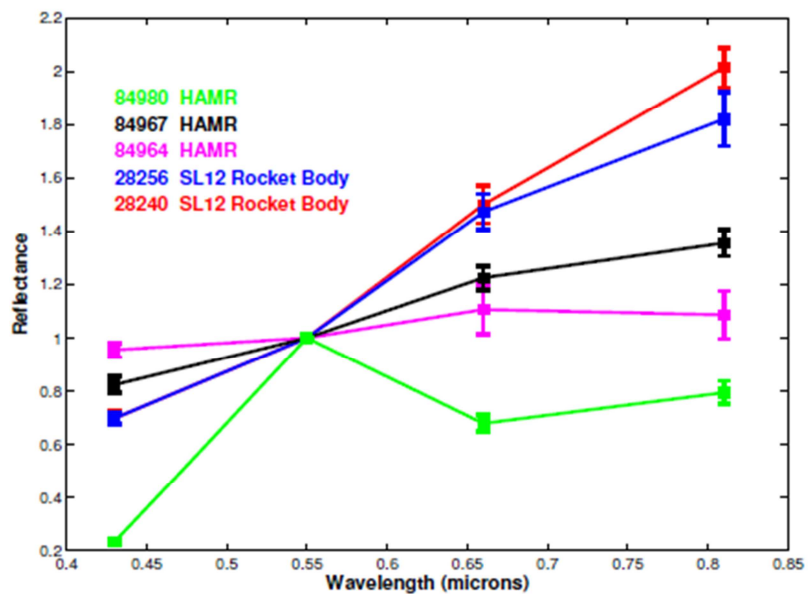


Figure 3.18 – Normalized reflectance of the objects observed on 25th August 2011 [44]

The observations were not carried out to and optimized for the production of lightcurves. On the other hand, plotting the derived magnitudes as a function of time shows the variations associated with the objects, which is another indication of the very different physical nature of our targets. In figures 3.19-21 the lightcurves, in the four different filters of the HAMR object 84980 (as observed on August 24 and

August 25) and of the Rocket Body SL12 28256 are shown. The much higher variation in magnitude in all the filters, typical of HAMRs objects, is apparent in figures 3.18 and 3.19, while a nearly periodic variation, possibly related to a rotational motion of the target can be seen in the case of the RB, in figure 3.20.

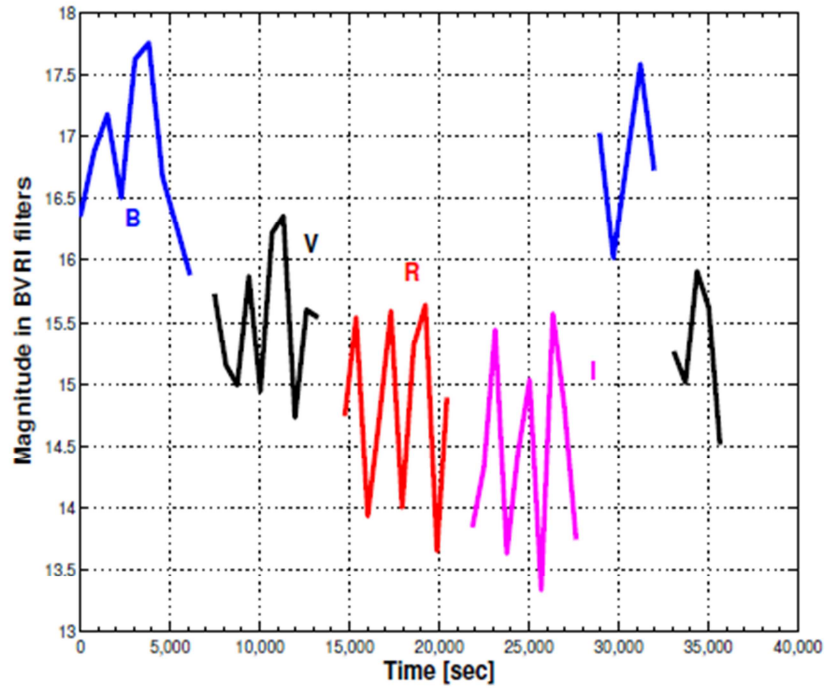


Figure 3.19 - Sample lightcurves of the object 84980 HAMR in the four filters, as observed on August 24th [44]

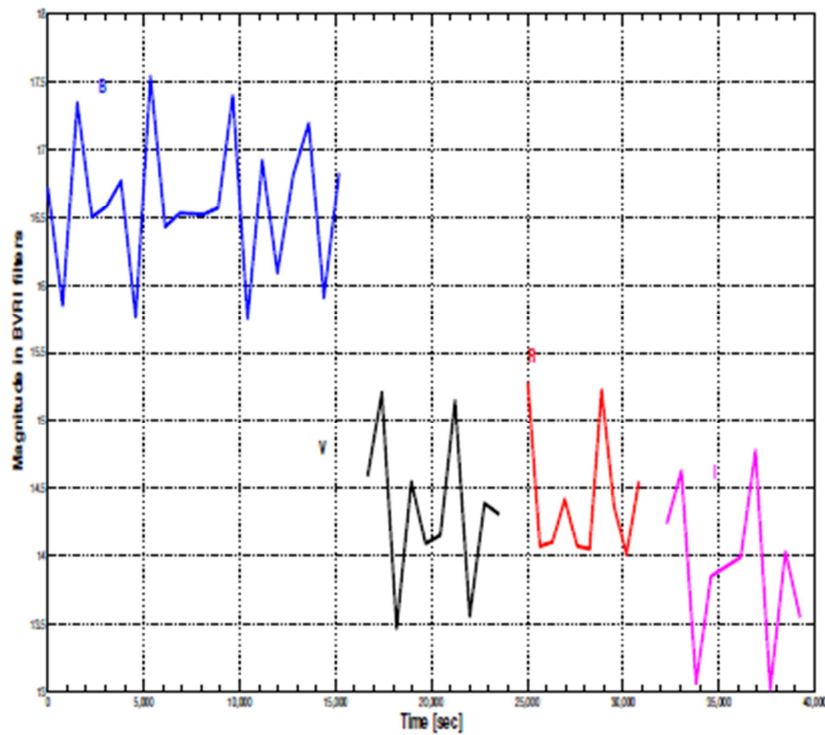


Figure 3.20 - Sample lightcurves of the object 84980 HAMR in the four filters, as observed on August 24th [44]

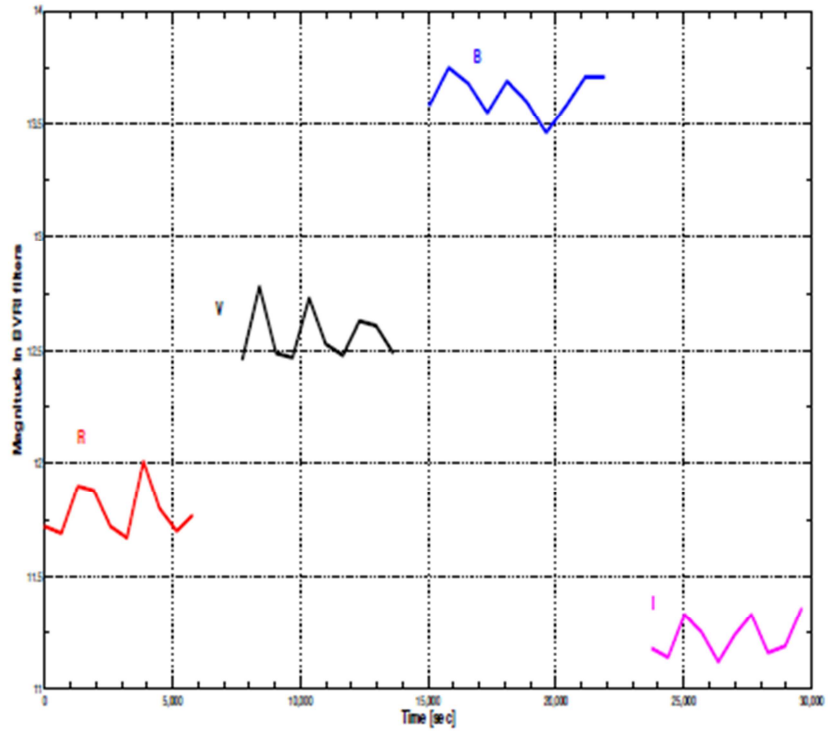


Figure 3.21 – Sample lightcurves of the object 28256 SL12 Rocket Body in the four filters, as observed on August 25th [44]

Chapter 4

Optical reflection spectroscopy of space debris

Part of the work of my thesis was carried out at the *Astronomy Department of the University of Michigan* (USA), coordinated by Professor Patrick Seitzer from March to August 2012. The main purpose of my thesis has been the study of space debris measurement systems and procedure. In particular I had the opportunity to develop several codes to solve the problem of blind non-sidereal tracking for orbital debris, including a Graphical User Interface (GUI) to automate space debris observation for spectroscopy and photometry.

During my period at the University of Michigan I had the opportunity to work closely with members from *NASA Orbital Debris Program Office, ESCG/Jacobs, Aerospace Engineering Department from California Polytechnic State University and LZ Technology*.

The NASA Orbital Debris Program Office, situated at the Johnson Space Center, is the lead NASA center for orbital debris research and conducts measurements of the environment and in developing the technical procedures to protect users of the orbital environment. In particular they develop an improve the understanding of the orbital debris environment and developing measures that can be taken to control debris growth [53].

Space debris research is divided into the following broad research efforts:

- Modeling
- Measurements
- Protection
- Mitigation
- Reentry

In particular measurements of near-Earth orbital debris are effected by conducting ground-based and space-based observations of the orbital debris environment by using optical and radar telescopes [53].

The data professor Seitzer's team gathers is fed into NASA's public software that models the risk to functional satellites from debris such as defunct satellites and spacecraft parts. Several techniques have been developed by professor Seitzer and his team to survey the sky for orbital debris at GEO, new tracking algorithms for spectroscopy of fast-moving targets, and a reverse time-delay integration (TDI) technique that to survey the sky with telescope motion only at the sidereal rate. It is highly efficient and has improved the signal-to-noise ratio of GEO objects in his images [54].

4.1 – The observatory used

Prof. Patrick Seitzer and his team conduct optical studies of orbital debris for the *NASA Orbital Debris Program Office* by using UMich's 0.6 m Curtis-Schmidt Telescope at Cerro Tololo in Chile. The main aim is to assess the total amount of debris at the geosynchronous orbit and then characterize targets by material with spectroscopy at the 6.5 m Magellan Telescope in Chile.

4.1.1 – Magellan

The *Magellan Observatory* is composed by two twins telescopes: *Walter Baade Telescope* and *Landon Clay Telescope*. They were built and continue to be operated by a consortium several university including the *Carnegie Institution of Washington*, *Harvard University*, *MIT*, the *University of Michigan*, and the *University of Arizona*. The telescopes are located at *Las Campanas Observatory*, high in the southern reaches of Chile's Atacama Desert. The Walter Baade telescope started first observations on September 2000, while the Landon Clay telescope only two years later [55].

The two telescopes are located 60 meters apart on an isolated peak (Cerro Las Campanas) (figure 4.1). The telescopes have a diameter of 6.5 m each and have an alt-azimuth design. The principal foci are f/11 at the two Nasmyth locations and f/15 in the Cassegrain position. In addition, three auxiliary f/11 are provided on the center section. An ADC corrector is accessible for f/11 use to provide the non-restriction of the field of view up to 24 arc-min. There are platforms on either side to provide access to the instruments at the principal Nasmyth ports.



Figure 4.1 – The Magellan Telescope (Baade on left, Clay on right)

The primary mirrors of the Magellan telescope were made and polished by the Steward Observatory Mirror Lab. The mirrors are composed of borosilicate glass with a structure in lightweight honeycomb.

The f/11 focus is a Gregorian configuration, which was designated with the purpose of improve the performance of the collimator optics in the wide-field spectrograph (IMACS). The Gregorian secondary is also considerably less aspheric than the corresponding Cassegrain secondary, and for this reason it is easier to test.

Both the telescope are designed to minimize image degradation due to thermal effects. For this reason a separate ventilation systems for the telescope structure has been installed. Moreover this airing system maintains the primary mirror surfaces at the outside air temperature during night time observing.

Active controls are incorporated in the telescope optics. The mirrors have position control for alignment. These are active during observing. To correct low-order aberrations in the optical system, an active control of the primary mirror is used. Moreover, the secondary mirror has a tip-tilt apparatus for fast guiding.

There are several instruments operating on the Las Campanas telescopes. For the purpose of the space debris observation more information is given on the following:

- **Magellan 1 - Baade Telescope - Instruments f/11**

- **IMACS**

The *Inamori Magellan Areal Camera and Spectrograph* (IMACS) is a wide-field imager and multi-object spectrograph. IMACS is a reimaging spectrograph mounted permanently on the Magellan Baade Telescope. It is fed by the telescope's 6.5m primary, f/11 Gregorian secondary, and flat tertiary mirrors, through an ADC/corrector. This optical train delivers an unvignetted field out to $R = 12$ arc-min with 9% vignetting at $R = 15$ arc-min. The all-transmitting (all-spherical-optics) collimator in IMACS contributes very little in the way of additional aberrations ($\text{FWHM} < 0.10$ arc-sec) [56].

- **FIRE**

The *Folded port InfraRed Echellette* (FIRE) spectrograph is a near-infrared echellette. It covers the full 0.8-2.5 micron band at a spectral resolution of 50 km/s. FIRE is designed to deliver high sensitivity with minimal contamination from atmospheric foregrounds [57].

- **Magellan II - Clay Telescope - Instruments f/11**

- **LDSS3**

The *Low Dispersion Survey Spectrograph* (LDSS-3) is a high efficiency, wide-field multi-slit spectrograph. The telescope is focussed onto a multi-aperture mask held in an 8-position wheel. The light then passes through various apertures cut in the mask and enters the collimator which converts the input f/11 beam into parallel light, before passing it through either a filter and/or a grism. The light is then focussed by the camera onto an external detector with a final focal ratio of f/2.5. Removable Hartmann masks are provided in the filter and grism wheels to aid in focusing.

Three grisms are mounted in the grism wheel at any one time and these cover a range of spectral resolution of several hundred to several thousand.

By using clear positions in the aperture and grism wheels, LDSS-3 can be used to give direct images in the chosen filter passband over a wide field of view. It thus doubles as a wide-field imager.

LDSS-3 reimages approximately a 8.3 arc-minute diameter field onto the CCD camera, with a scale of 0.189 arc-sec/pixel [58].

4.1.2 – MODEST

The *Curtis-Schmidt telescope* (figure 4.2) is a 0.61-meter aperture f/3.5 Schmidt telescope and it is located at the *Cerro Tololo Inter-American Observatory* in Chile. Originally installed at *UMich's Portage Lake Observatory* in 1950, but then it was moved due to the light pollution of the location to the clearer skies of north central Chile in 1966. It is named for Heber D. Curtis, who has been the Director of the University of Michigan Observatories from 1930 until 1942.

The telescope is fully dedicated to optical studies of space debris for NASA Orbital Debris Program Office at the Johnson Space Center. The acronym for the debris project is *MODEST* (Michigan Orbital DEbris Survey Telescope) ([53], [59], [60]).

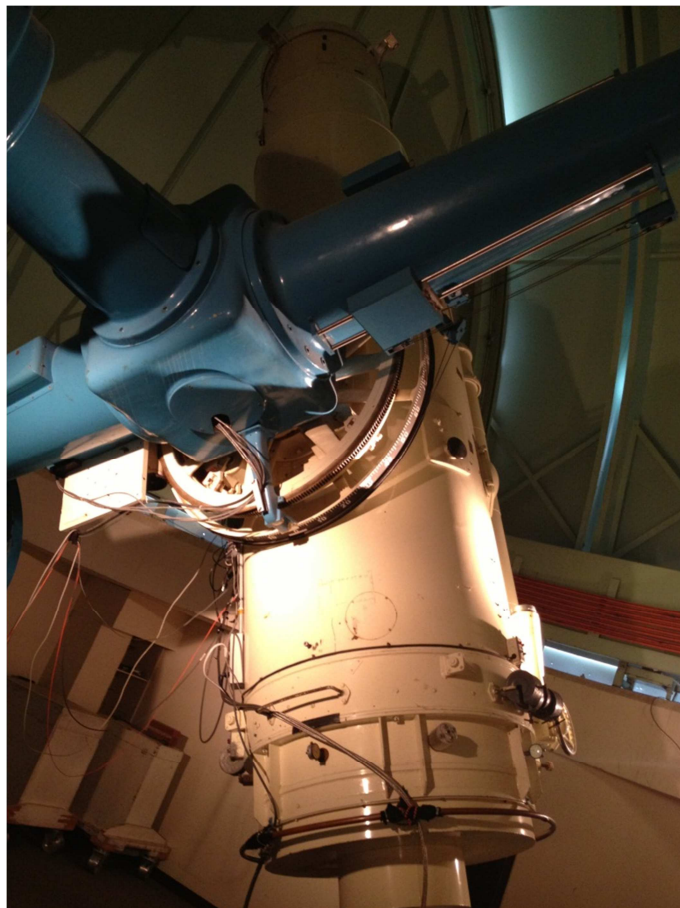


Figure 4.2 – MODEST

4.3 – Blind Non-Sidereal Tracking problem

The main goal of the project I have participated in is to comprehend the physical characteristics of debris at geosynchronous orbit (GEO). The approach is to relate the observed reflectance as a function of wavelength with laboratory measurements of typical spacecraft surfaces to understand what the materials are likely to be. Because debris could be irregular in shape and tumbling at an unknown rate, rapid simultaneous measurements over a range of wavelengths are required. Acquiring spectra of optically faint objects with short exposure times to minimize these effects requires a large telescope ([61], [62]).

Spectroscopy of debris is potentially a powerful tool for understanding just what the surfaces are of the unresolved objects that we track as GEO debris. In many cases, the orbits and the origin of pieces of cataloged debris are known. For some of these objects an estimate of area-to-mass ratio can be determined by observing the change in orbit with time. But what are not known are the exact surface characteristics of the object in question. A spectrum covering a wide range in wavelength could in principal answer this question when compared with laboratory spectra of known spacecraft materials ([64], [65], [66]).

The Magellan telescopes are designed for superb image quality, and frequently the image quality delivered to the focal plane is better than 0.5 arc-sec FWHM. The mounts are alt-azimuth, with image rotators at all focal stations to allow long exposure imaging of the night sky. The advantage of using such large telescopes on bright objects (typical cataloged pieces of debris are between $R = 15^{\text{th}}$ and 19^{th} magnitude) is that only relatively short exposure times are required to achieve usable signal to noise ratios across a wide range of wavelength. Exposure times for all of our debris observations were 30 seconds. If an object is rotating or tumbling slower than this, it is possible to obtain a spectrum of one surface. If the period is shorter than 30 seconds, then it will be obtained a time averaged spectrum of whatever surfaces of the debris piece that were presented during the time the instrument shutter was open.

For optical spectroscopy it was used one of the twin 6.5-m Magellan telescopes, in particular the Clay telescope with the LDSS3 [59]. This instrument has an imaging mode for acquisition. After acquisition and centering of a GEO object, a slit and grism are moved into the beam for spectroscopy. Typical exposure times for spectra were 30 seconds. It has an acquisition field of view of 8.3 arc-minutes diameter. The observations for space debris used a 5 arc-second wide slit, and the VPH-ALL grism. This yields a wavelength range from 3800 to 9000 Angstroms, but due to atmospheric refraction effects and there are only results from 4500 to 8000. The spectral sampling was 1.9 Angstroms/CCD pixel.

With such a wide slit (5 arc-sec), and excellent image quality (always better than 1 arc-sec FWHM) during these observations, the resolution is set by the FWHM of the star in the slit. The primary reason for such a wide slit was the difficulty of tracking the object. The slit is oriented East-West to minimize contamination from star streaks. All observations were obtained at airmass <1.7 to minimize effects of atmospheric refraction.

The major technical challenge of these observations is blind non-sidereal tracking [67]. Once the grism is inserted in the beam, there is no information on where the object is in the slit. The Magellan telescopes were designed for sidereal tracking of stars and have guide probes and wavefront sensors at the edge of the field of view. Such devices work well on round stars but not on streaked stars moving past them at roughly 15 arc-sec/sec.

Previously the observing procedure was as follows [61]:

1. Slew the telescope to a star field near the predicted position of the debris piece as determined from the public TLE (Two Line Element set) [See Appendix A.2].
2. The operator would focus the telescope and align the mirrors for best image quality while tracking at the sidereal rate. These steps can only be done while tracking a star.
3. At the appropriate Universal Time of prediction in step 1, the telescope rates were set to track the object at the rates determined from the TLE by differencing predicted positions at 30 second intervals
4. A 5 second acquisition exposure was obtained through a Sloan r filter.
5. Once the object was acquired a series of 5 short exposures were taken to determine in real-time differential rate corrections since the TLEs are not high precision orbits.
6. The object was offset to the predicted position of the center of the slit. This sometimes took several iterations.
7. The slit was inserted into the beam and an exposure taken to confirm that the object was indeed in the center of the slit.
8. The Sloan r filter was removed, the grism inserted, and five 30 second exposures taken.
9. Once the spectrographic sequence was finished, a comparison arc source (helium - neon - argon) was taken for wavelength determination, and then followed by 5 exposures of a quartz lamp for a continuum flat field, all with the grism and slit in place and the telescope tracking.

The main problem with this procedure concerned the determination of the rate. In fact by differentiating the position of the object with a 30 sec step starting from the date obtained from TLE the error committed was too high for long exposure.

Hereafter the equation showing how the velocity where calculated

$$\begin{cases} dec_{rate_{k+1}} = \frac{dec_{pos_{k+1}} - dec_{pos_k}}{t_{span}} \\ ha_{rate_{k+1}} = \frac{ha_{pos_{k+1}} - ha_{pos_k}}{t_{span}} \end{cases} \quad (4.1)$$

where dec_{rate} is the declination while ha_{rate} is hour angle velocity [for celestial coordinate system see appendix A.1]

As it is possible to observe from figure 4.3, the committed error by considering the value of the rate constant for all the time step is too high, due to the absolute value of the acceleration of the object that is growing (figure 4.4).

Moreover the error is defined as the difference between the position given by propagating the TLEs and the position calculated by updating the rates every 30 seconds. For this reason having the most accurate prediction of the position of the satellite on the orbit is mandatory.

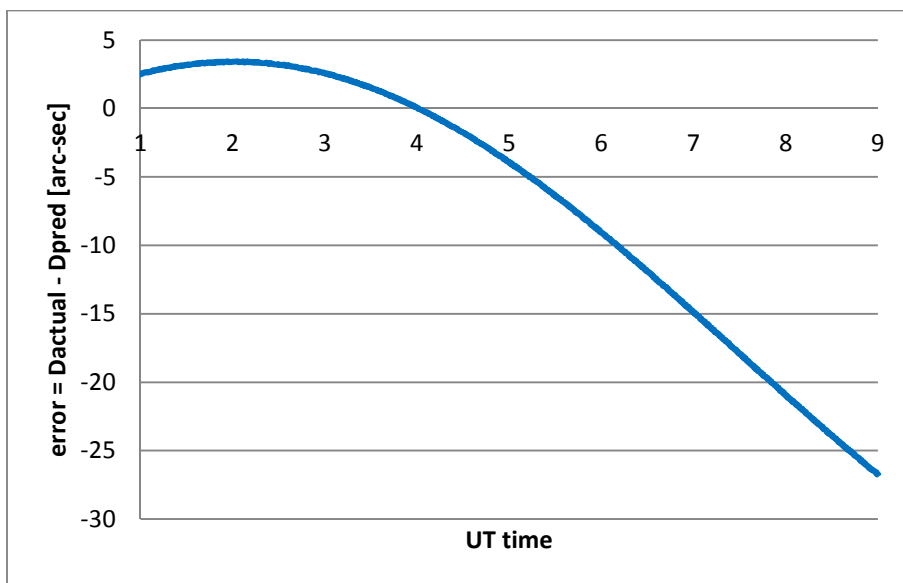


Figure 4.3 – error in DEC position committed by updating DEC rate without corrections for SSN25000

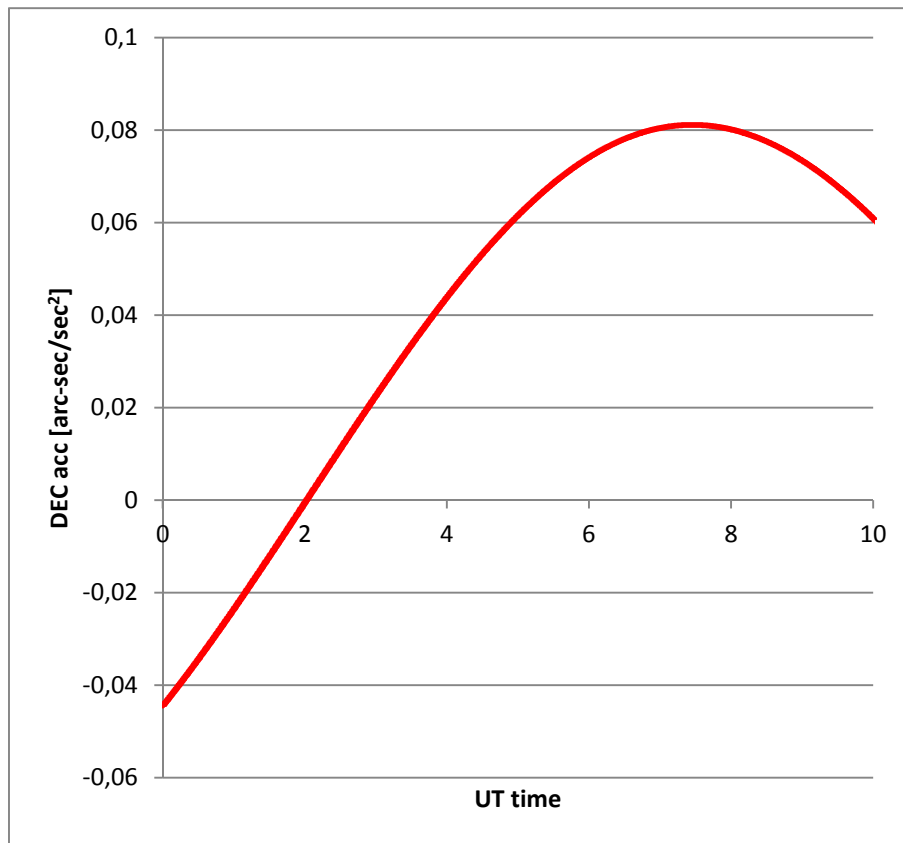


Figure 4.4 – DEC acceleration's plot for SSN 25000

4.4 – Rates correction code

The position of the satellite for the observations is given by NASA Orbital Debris Program Office into a format called *.MLB file* that contains the value of several parameters of the satellites during the orbit with a 30 seconds time steps.

The data contained in the *.MLB files* are obtained directly from the TLEs sets with a custom code that uses *SGP Classic Propagator* (the form of the program is from the *Project Spacetrack Report*). Starting from the TLE data format that contains orbital elements that describe the orbits of Earth-orbiting satellites, the code computes the position of the object on the orbit, calculates the rates by differentiating the value for the positions, the accelerations, the range, the solar phase angle and indicates with a flag if the object at a particular time is in eclipse or not. An example of *.MLB file* is shown in figure 4.5.

UT dec	UT hr	UT min	UT sec			RA dec	DEC dec	RA hr	RA min	RA sec
#m1 2012	-6	-29	22 6000.0	#####	176,0064	961				
21,99167	21	59	30	5,90995	248,2549	213,9676	-5,7254	14	15	52,2293
22	22	0	0	5,9103	248,3802	214,0575	-5,72298	14	16	13,7939
22,00833	22	0	30	5,91064	248,5056	214,1474	-5,72053	14	16	35,3634
22,01667	22	1	0	5,91099	248,6309	214,2372	-5,71804	14	16	56,9379
22,025	22	1	30	5,91134	248,7563	214,3272	-5,71551	14	17	18,5175
DEC deg	DEC min	DEC sec	RArate arc-sec/sec	DECrate arc-sec/sec	HArate arc-sec/sec					epoch
-5	43	31,4254	0	0	0	100	2012,5			
-5	43	22,7312	10,78228	0,28981	4,25872	100	2012,5			
-5	43	13,9014	10,78474	0,29433	4,25626	100	2012,5			
-5	43	4,9359	10,78725	0,29885	4,25375	100	2012,5			
-5	42	55,8345	10,78982	0,30338	4,25118	100	2012,5			
Day of year	RAacc arc-sec/sec ²	DECacc arc-sec/sec ²	Eclipse flag	Range km	Solar phase angle deg					
181	0	0	0	36914,595	67,98					
181	0	0	0	36910,372	67,9					
181	0,295	0,5425	0	36906,057	67,81					
181	0,30144	0,5429	0	36901,65	67,73					
181	0,30789	0,54332	0	36897,151	67,64					

Figure 4.5 – Example of .MLB file for SSN25000

As previously said, the position error that was used to select the correct value of the rate was strictly connected to the predictions which had to be assumed as truth. It has been necessary to implement a new code to compute the value of the rates to keep the theoretical error equal to zero.

Several solutions were analyzed to keep the position error (for both declination and hour angle) equal to zero, in particular two different solutions:

- a polynomial interpolation of declination and hour angle to calculate the rates by differentiating
- an every step correction of the differential value of the functions given by the .MLB file to keep the difference between the theoretical position and the one obtained by updating the rates equal to zero.

The main advantage of the first method would be the one to change the 30 sec time step which is fixed from the .MLB files and realize a code with adaptive time step depending on the velocity of the target. In fact during the orbit the value for DEC (declination) and HA (hour angle) rates change a lot depending on the position of the target on the orbit (in apogee the velocity it is lower than perigee) [See appendix A.1]. With the polynomial interpolation for both declination and hour angle the computational steps to calculate the rates would be very easy but during several simulation a problem was discovered. Due to the time discretization of the .MLB files and the consequential round-off errors, the perfect agreement between the temporal data and the position in both declination and hour angle. Moreover the value of the HA position is strictly connected to the time data due to the presence in the Eq. (4.2)

$$HA = (GST - time\ zone) \cdot 15 - RA \quad (4.2)$$

where HA is hour angle position and GST is Global Sidereal Time [See appendix A.1]

This has an effect and results in an error connected to the round-offs that can rise up to 10^{-1} arc-sec that can cause the drift of the object from the slit and cannot be corrected because it goes directly to change the value of the position that we have to assume as true.

Moreover by assuming the punctual differential value for DEC-rate and HA-rate constant for the whole duration of the time step results in an error that is comparable to the one that was committed by using directly the value of the rates given by the .MLB files.

An example of the increase in error by using this methodology is shown in figure 4.6.

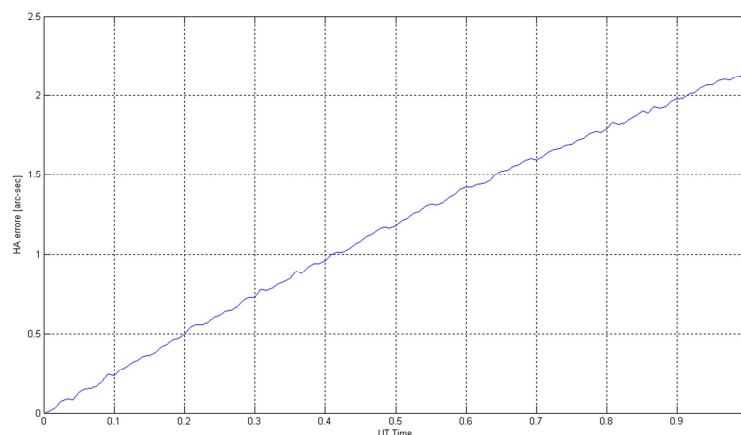


Figure 4.6 – Rising of the HA position error in 1 hour simulation

For this reason a simpler method was developed. The computation cost of this one is lower than the polynomial interpolation and provide better results. By modifying the definition of the difference quotient with the error committed at every steps it was possible to keep the theoretical error equal to zero.

The first step was to define the value of the position of the object at step k by using the value obtained at step $k - 1$ as shown in Eq. (4.3). (For step 0 the values are taken directly from the .MLB file without any correction).

$$dec_{pos_k} = dec_{pos_{k-1}} + dec_{rate_{k-1}} \cdot time_{step} \quad (4.3)$$

Where $time_{step}$ is equal to 30 seconds.

A first evaluation of the committed error is done by

$$errordec_{pos_k} = errordec_{pos_{k-1}} + (dec_{pos_k} - dec_{predicted_k}) \quad (4.4)$$

where $errordec_{pos_{k-1}}$ is the total final error committed at the previous step (The code is developed in such a way that this error is equal to zero) and $dec_{predicted_k}$ is given by the MLB file.

The value of the rate for step $k - 1$ is then modified by using the value of $errordec_{pos_k}$ and dividing it by the time step.

$$dec_{rate_{k-1}} = dec_{rate_{k-1}} - \frac{errordec_{pos_k}}{time_{step}} \quad (4.5)$$

A check is done by calculating again $errordec_{pos_k}$ and it is now equal to zero.

An analogous correction-algorithm is done for HA and the results from a 24-hour simulation are shown in figure 4.7 where it is possible to observe that the HA position error is always kept equal to zero.

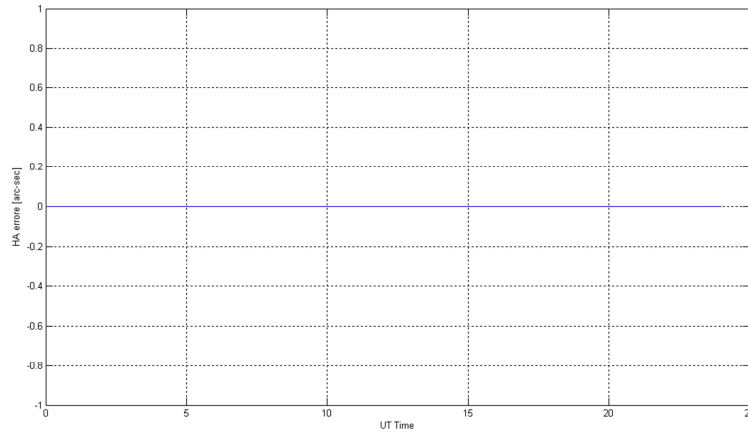


Figure 4.7 – HA position error is kept equal to zero for a 24h simulation

The result is that it is possible to keep the target inside the slit as is shown in figure 4.8.

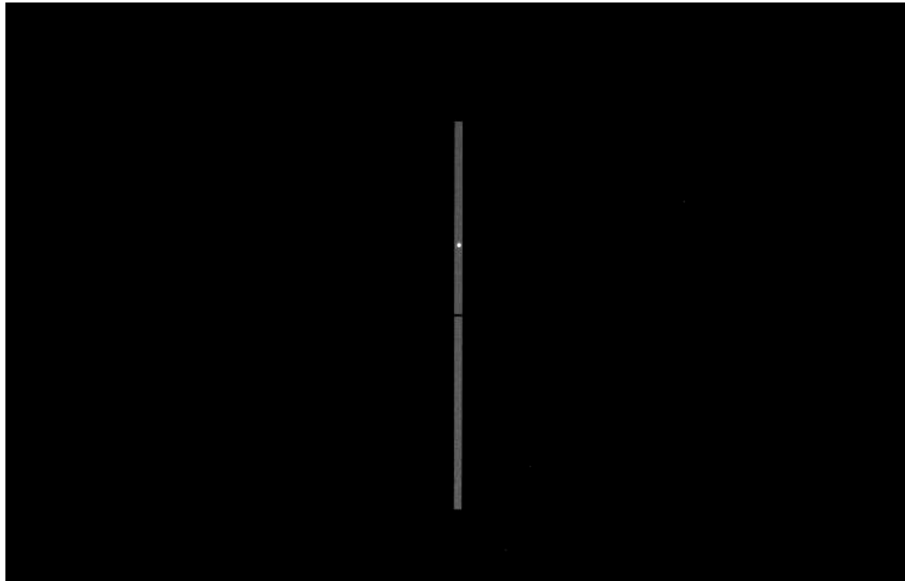


Figure 4.8 – The target is inside the 5" slit

The goal of this code is to create a .txt file that contains all the information needed by the software in order to move the telescope to follow the target.

An example of the output is shown in figure 4.9. It is possible to see that the .txt file created contains information that the telescope needs. It is made up of thirteen different columns:

1. UT time
2. RA (position in right ascension)
3. DEC (position in declination)
4. HA rate (calculated value for HA rate)
5. DEC rate (calculated value for DEC rate)
6. Eclipse flag (0 if the object is not in eclipse, 1 if in eclipse)
7. DOY (Day Of Year)
8. Year
9. DEC error (is equal to zero for construction of the code, it is a visual check)
10. HA error (is equal to zero for construction of the code, it is a visual check)
11. HA rate exceeds flag (0 if rates are below the slew limits of the telescope, 1 if not)
12. DEC rate exceeds flag (0 if rates are below the slew limits of the telescope, 1 if not)
13. SSN (name of the object given by United States Space Surveillance Network)

UT_time	RA_pos	DEC_pos	HA_rate	DEC_rate	Flag	DOY	Year	Derror	HAerror	HA_Exceed	D_Exceed	SSN
22.00000	348.40026	-4.83946	-0.14640	1.86360	0	32	2013.16	0.00000	0.00000	0	0	22911
22.00833	348.52643	-4.82393	-0.12720	1.86960	0	32	2013.16	0.00000	0.00000	0	0	22911
22.01667	348.65259	-4.80855	-0.14520	1.87560	0	32	2013.16	0.00000	0.00000	0	0	22911
22.02500	348.77875	-4.79272	-0.14280	1.88040	0	32	2013.16	0.00000	0.00000	0	0	22911
22.03333	348.90489	-4.77705	-0.12360	1.88640	0	32	2013.16	0.00000	0.00000	0	0	22911
22.04167	349.03102	-4.76133	-0.14160	1.89120	0	32	2013.16	0.00000	0.00000	0	0	22911
22.05000	349.15715	-4.74557	-0.13920	1.89720	0	32	2013.16	0.00000	0.00000	0	0	22911
22.05833	349.28326	-4.72976	-0.12120	1.90200	0	32	2013.16	0.00000	0.00000	0	0	22911
22.06667	349.40937	-4.71391	-0.13680	1.90800	0	32	2013.16	0.00000	0.00000	0	0	22911
22.07500	349.53546	-4.69801	-0.13560	1.91280	0	32	2013.16	0.00000	0.00000	0	0	22911
22.08333	349.66154	-4.68207	-0.11760	1.91880	0	32	2013.16	0.00000	0.00000	0	0	22911
22.09167	349.78762	-4.66608	-0.13320	1.92480	0	32	2013.16	0.00000	0.00000	0	0	22911
22.10000	349.91368	-4.65004	-0.13200	1.92840	0	32	2013.16	0.00000	0.00000	0	0	22911
22.10833	350.03973	-4.63397	-0.11400	1.93560	0	32	2013.16	0.00000	0.00000	0	0	22911
22.11667	350.16578	-4.61784	-0.12960	1.94040	0	32	2013.16	0.00000	0.00000	0	0	22911
22.12500	350.29181	-4.60167	-0.12840	1.94520	0	32	2013.16	0.00000	0.00000	0	0	22911
22.13333	350.41783	-4.58546	-0.11040	1.95120	0	32	2013.16	0.00000	0.00000	0	0	22911
22.14167	350.54385	-4.56920	-0.12600	1.95600	0	32	2013.16	0.00000	0.00000	0	0	22911
22.15000	350.66985	-4.55290	-0.12480	1.96200	0	32	2013.16	0.00000	0.00000	0	0	22911
22.15833	350.79584	-4.53655	-0.10560	1.96680	0	32	2013.16	0.00000	0.00000	0	0	22911
22.16667	350.92182	-4.52016	-0.12360	1.97280	0	32	2013.16	0.00000	0.00000	0	0	22911
22.17500	351.04780	-4.50372	-0.12120	1.97760	0	32	2013.16	0.00000	0.00000	0	0	22911
22.18333	351.17376	-4.48724	-0.10200	1.98240	0	32	2013.16	0.00000	0.00000	0	0	22911
22.19167	351.29971	-4.47072	-0.11880	1.98840	0	32	2013.16	0.00000	0.00000	0	0	22911
22.20000	351.42565	-4.45415	-0.11760	1.99320	0	32	2013.16	0.00000	0.00000	0	0	22911
22.20833	351.55158	-4.43754	-0.09840	1.99920	0	32	2013.16	0.00000	0.00000	0	0	22911
22.21667	351.67750	-4.42088	-0.11520	2.00280	0	32	2013.16	0.00000	0.00000	0	0	22911
22.22500	351.80341	-4.40419	-0.11400	2.01000	0	32	2013.16	0.00000	0.00000	0	0	22911
22.23333	351.92931	-4.38744	-0.09480	2.01480	0	32	2013.16	0.00000	0.00000	0	0	22911
22.24167	352.05520	-4.37065	-0.11160	2.01960	0	32	2013.16	0.00000	0.00000	0	0	22911
22.25000	352.18108	-4.35382	-0.11040	2.02440	0	32	2013.16	0.00000	0.00000	0	0	22911
22.25833	352.30695	-4.33695	-0.09120	2.03040	0	32	2013.16	0.00000	0.00000	0	0	22911
22.26667	352.43281	-4.32003	-0.10800	2.03520	0	32	2013.16	0.00000	0.00000	0	0	22911
22.27500	352.55866	-4.30307	-0.10680	2.04000	0	32	2013.16	0.00000	0.00000	0	0	22911
22.28333	352.68450	-4.28607	-0.08760	2.04600	0	32	2013.16	0.00000	0.00000	0	0	22911
22.29167	352.81033	-4.26902	-0.10440	2.05080	0	32	2013.16	0.00000	0.00000	0	0	22911
22.30000	352.93615	-4.25193	-0.10200	2.05560	0	32	2013.16	0.00000	0.00000	0	0	22911
22.30833	353.06195	-4.23480	-0.08400	2.06160	0	32	2013.16	0.00000	0.00000	0	0	22911
22.31667	353.18775	-4.21762	-0.10080	2.06520	0	32	2013.16	0.00000	0.00000	0	0	22911
22.32500	353.31354	-4.20041	-0.09840	2.07120	0	32	2013.16	0.00000	0.00000	0	0	22911
22.33333	353.43931	-4.18315	-0.08040	2.07720	0	32	2013.16	0.00000	0.00000	0	0	22911

Figure 4.9 – Results file for SSN 22911

The code is developed to allow the user to operate it for several different telescope. In fact starting from the .MLB files from NASA it is possible to run the code and insert the parameters of the observatory that the observer will use.

When the code is running input is required about the characteristics of the telescope (see figure 4.10). Three different telescope characteristics are preloaded:

1. MODEST
2. CTIO 0.9 [72]
3. Magellan

If the telescope in which the results file runs is not one of these the code allows the user to insert the parameters for slew limit [arc-sec/sec] of the observatory: in fact in case the corrected rate is over the slew rate the telescope will not able to follow the target and an indicator flag is needed in the results file.



```
Command Window
Before running code, please have all .mlb files within main path in a subdirectory called "mlb"
What is the code main directory? C:\Users\Tommaso\Documents\Universita\Astronomy Department\Algorithm Blind Tracking\V4.2_SSN5
Obtain results for
1- MODEST
2- C9
3- MAGELLAN
4- Other Telescope
Insert 1 2 3 or 4: 4
Other Telescope
Insert slew rate limitations [arc-sec/sec]
Upper Drate limit : 10
Lower Drate limit : -10
Upper HArate limit : 10
fx Lower HArate limit : -10
```

Figure 4.10 – Initialization of the program in which the users have to select the parameters of the telescope

Once the initialization is done the program will create a .txt file with the name of the SSN object and the DOY to which they relate to.

4.5 – GUI (Graphical User Interface) development

The non-sidereal rate tracking software has been implemented as a graphical user interface (GUI) for use with Magellan and MODEST. These telescope uses Windows Telescope Control Software (*WinTCS*) developed by DFM Engineering and the GUI is realize to communicate with this. In figure 4.11 is possible to observe the DFM Control System that is used at MODEST.

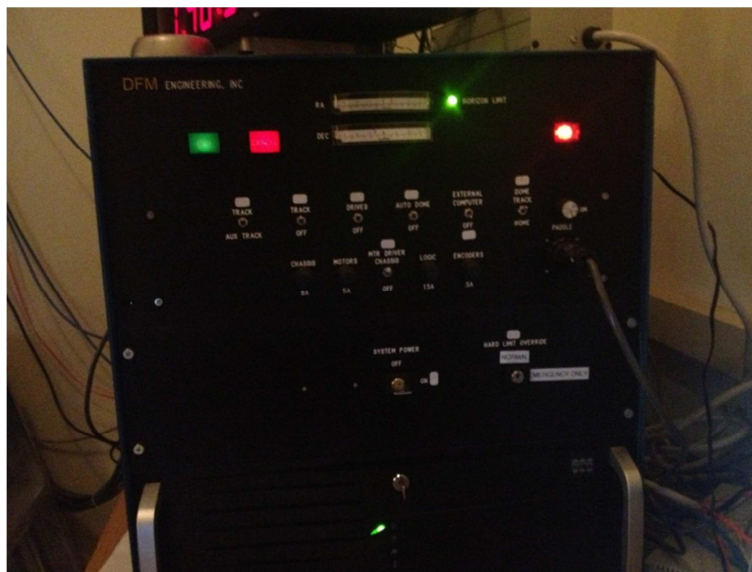


Figure 4.11 – MODEST DFM Control System

A graphical user interface (GUI) is a human-computer interface that uses windows, icons and menus and which can be manipulated by a mouse. GUIs stand in sharp contrast to command line interfaces (CLIs), which use only text and are accessed solely by a keyboard. The main advantages of using a GUI consist in that it can be user-friendly and can speed up the user's work.

The GUI has been developed in MATLAB environment and contains all the commands for the blind non sidereal rate tracking of space debris. The main role of the GUI is to interface the user with the DFM code that is used to control the telescope. The final version of the GUI is shown in figure 4.12.

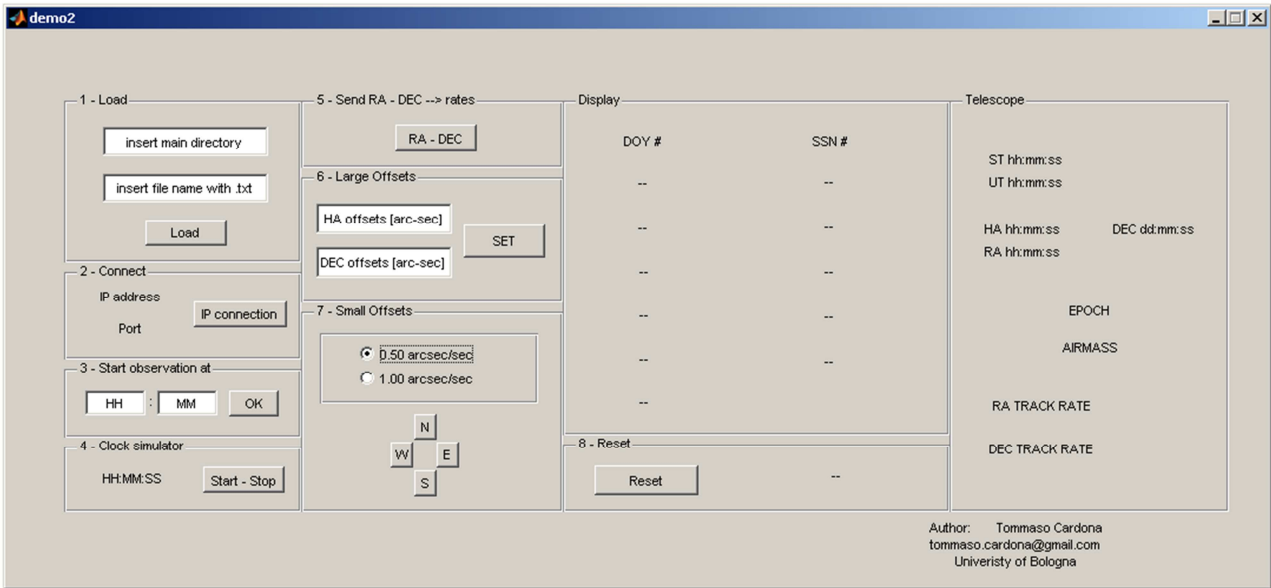


Figure 4.12 – GUI overview

GUI is structured in 8 different input blocks that allow the user to communicate with the telescope and control it to observe the target and keep it inside the slit for spectroscopy or for doing astronomical photometry.

The first input block is called “Load” (figure 4.13). It contains two different *text boxes* in which the user has to insert the main path and the file name created with the non-sidereal tracking rate code. After pushing the *Load* button, the file is loaded. In the *Display* panel a green flag indicates that the file has been loaded properly.

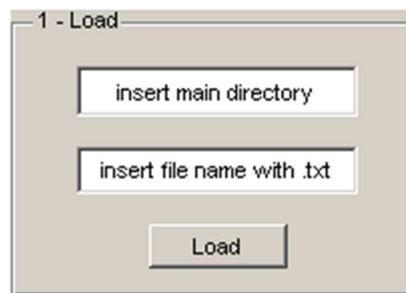


Figure 4.13 – Load box

The communication between the code and the DFM Control System is made by a TCP/IP interface. The TCP/IP connection uses standard Ethernet technology. Ports must be set in WinTCS as well as in the GUI.

For this reason the second box is created (figure 4.14). It allows the user to create a TCP/IP connection with the control system by using a default IP address and port with 9600 baudrate. The connection is established by pushing the *IP connection* button. A green flag in the panel indicates if the communications work fine.

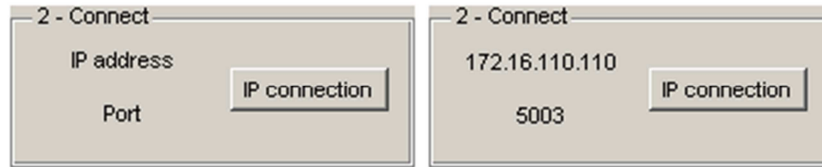


Figure 4.14 – IP communication Box before and after connection

After a connection is established, it is possible to set the time to start the observation. This is made by the third block in which the UT time for starting the observation has to be set. It has to be greater than the current time by at least 3 minutes to allow the telescope to move from the parking spot to the target coordinate position. If the time value is less than 3 minutes, a red flag appears in the display and the user has to change the time. Otherwise the user can start the clock simulator (fourth block) and then push the button to send the coordinates for right ascension and declination (fifth block). Green flags as shown in figure 4.15 indicate that the process is working well without any problem. In particular there is a flag about the eclipse: if there is no eclipse for the target a green flag with the words *NO ECLIPSE* will appear. Otherwise three different situation can happen (figure 4.16):

1. The object is in eclipse. A red flag indicates that it is not possible to observe the target. A countdown also activates until the end of the eclipse phase.
2. The object is not in eclipse but it will be in a short period. A yellow flag indicates this phase and a countdown is activated until the end of the eclipse.
3. The object is not in eclipse because that phase passed just a few minutes before. A green flag indicates how much time has passed since then.

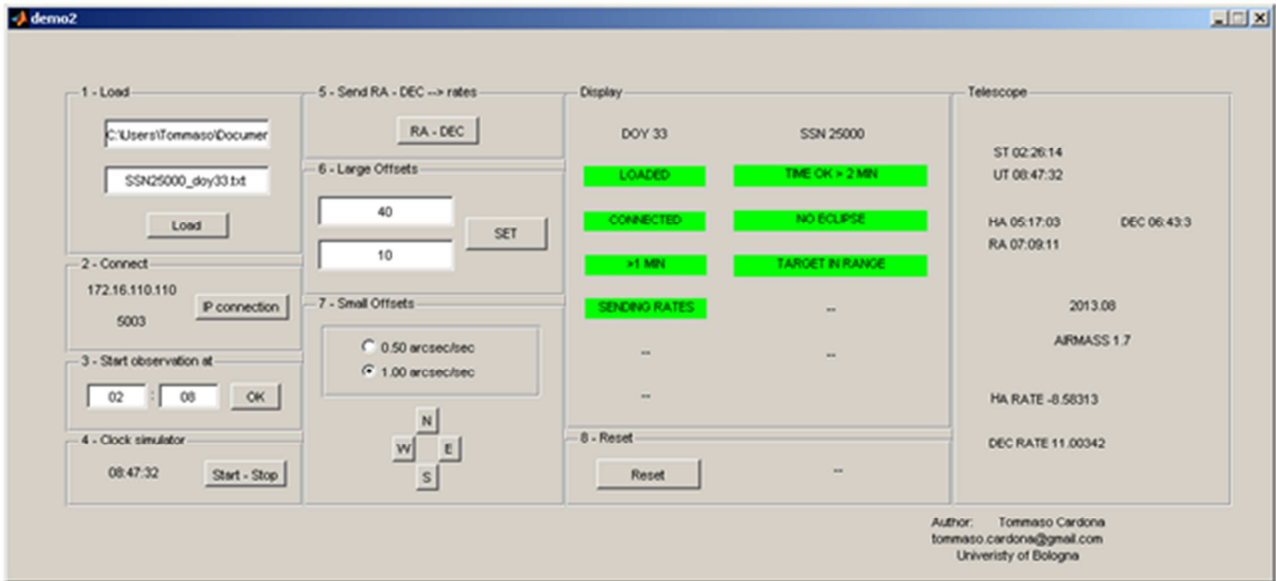


Figure 4.15 –GUI overview during observations

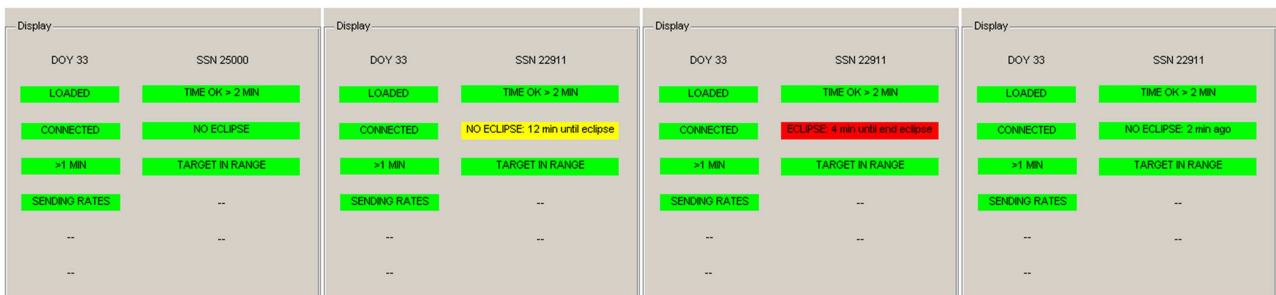


Figure 4.16 – Different eclipse flags

To set up automatic slew a command is necessary. It checks destination coordinates for horizon, if the coordinates are below the telescope horizon, the TARGET OUT OF RANGE red flag will appear on the screen, otherwise a green flag will show that the target is in range and the code then can start sending the coordinates (figure 4.17).

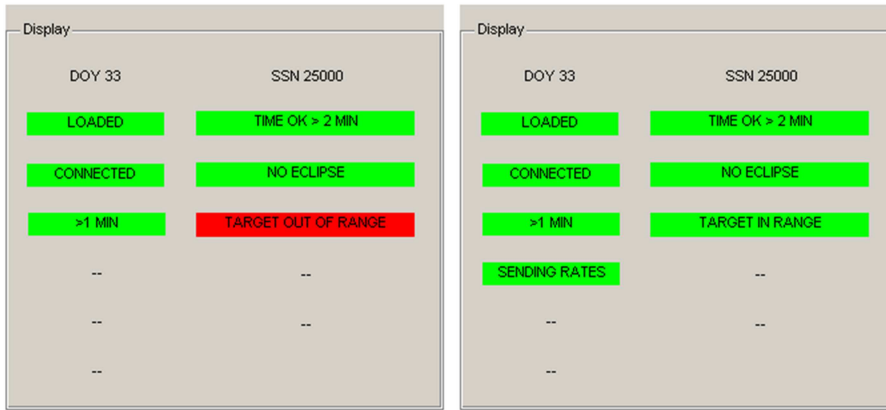


Figure 4.17 – TARGET OUT OF RANGE/IN RANGE Flag

The command used is shown in table 4.1.

Table 4.1
SLEW – COMMAND 6

EXCOM sends	Characters	Comments
	6 <CR>	Command #
	12.012345 <CR>	HA (hours)
	6.645643 <CR>	DEC (degrees)
	2013.08 <CR>	Epoch
TCS Resposnds	NO RESPONSE	Enables slew to HA, DEC

This command prepares TCS to automatically slew the telescope to the coordinates specified. After the slew is ENABLED (status bit set) by COMMAND 6, a COMMAND 12 (GO) is required to initiate slew (table 4.2).

Table 4.2
GO – COMMAND 12

EXCOM sends	Characters	Comments
	12<CR>	Command #
TCS Resposnds	NO RESPONSE	Begins automatic motion

Once the telescope is moved to the correct position of the target, the code starts sending automatically the rates obtained from the .txt file.

To change track rate HA and DEC it is necessary COMMAND 14 (TRACK) (table 4.3).

Table 4.3
TRACK – COMMAND 14

EXCOM sends	Characters	Comments
	14<CR>	Command #
	15.041 <CR>	HA rate (arc-sec/sec)
	6.25 <CR>	DEC rate (arc-sec/sec)
	0 <CR>	AUX HA rate (arc-sec/sec)
	0 <CR>	AUX DEC rate (arc-sec/sec)
TCS Resposnds	NO RESPONSE	Change track rates

This command allows modification of both HA and DEC track rates. There is provision for an auxiliary track rate which is useful if comparisons are made between sidereal and non-sidereal objects. The auxiliary track rate is selected by using a front panel switch.

After this the user have to start taking pictures using the CCD sensor and the calculate the offsets of the object. In fact due to the precision of the instrument the object will appear inside the field of view but not in the center: it is necessary to realize some offsets to place the target in a specific point (i.e. inside the slit for spectroscopy). It is possible to do this by setting parameters for large or small offsets. As the DFM code allows the user to set automatic offsets while the instrument is tracking at sidereal rates, these necessary offset are done by adding or subtracting a certain rate to the one that is sent form the calculated file to the telescope. It is very important not to exceed the slew limit: the telescope has some limits which must be known before starting to observe. These values are the same ones that the non-sidereal rate code requires during initialization to create apposite *rate exceed flags*. To avoid damaging the instrument the telescope can move only between a maximum and minimum rate (DECrate and HArate limits are usually different). If the calculated value is higher (or lower) than the maximum (or minimum) value, the GUI sends to the telescope this max (or min) value: the object starts drifting but this small drift enables the observer non to lose immediately the target from the field of view. Even during offsets the rate can exceed these limits, like the previous case the rate that will be sent is the maximum (or minimum) that is allowed. If DECrate or HArate exceed the limits a red flag on the display will warn the user (figure 4.18).

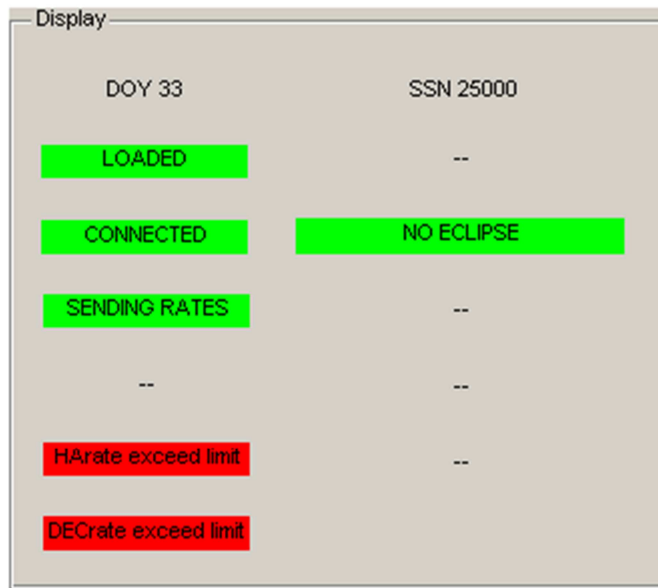


Figure 4.18 – Rate limit red flags indicate that the telescope is receiving the max (or min) rate it is allowed to receive

The large offsets are commutated by dividing the arc-sec input value (figure 4.19) by the hour angle and declination by the time step (that is equal to 30 seconds). They can be considered as correction rate values and are added to the next DECrate and HArate that will be sent to the telescope for all the 30 second step.

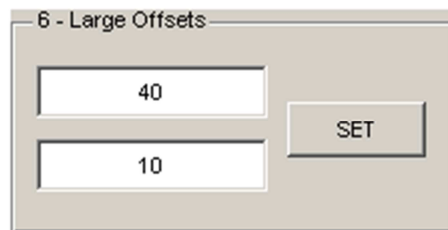


Figure 4.19 – Large offsets input block

Otherwise if the user wants to operate small offsets it is possible to correct the position of the target inside the field of view by using the user friendly arrow pad on screen (figure 4.20). It is possible to select two different precision correction rates (0.5 or 1.0 arc-sec/sec) and by pushing the button N (North), S (South), E (East) or W (West) it possible to add a small correction to the rate. The correction is done only for 1 sec. If more corrections are needed the user has to press again the button. Also in this case if the rates exceed the limits the value that is sent to the telescope is the max (or min) value that is allowed.



Figure 4.20 – Small offsets block

During observations the *Telescope* block (figure 4.21) shows several parameters on screen that are obtained directly from the telescope with COMMAND 25 (COORDS) (table 4.4). This command is used to allow TCS to send the telescope coordinates out over the TCP/IP communication.

Table 4.4
COORDS – COMMAND 25

EXCOM sends	Characters	Comments
	25<CR>	Command #
TCS Resposnds		Twelve real numbers followed by carriage returns
	5.288055 <CR>	HA (hours)
	7.153055 <CR>	RA (hours)
	6.7175 <CR>	DEC (degrees)
	2013.08 <CR>	Epoch
	1.7 <CR>	Airmass
	22.035423 <CR>	Sidereal Time (hours)
	5.23415 <CR>	Universal Time (hours)
	2013.07934 <CR>	Year (Now)
	-8.58313 <CR>	HA track rate
	11.00342 <CR>	DEC track rate
	1800.00 <CR>	Max slew speed
	90 <CR>	Dome azimuth (degrees)

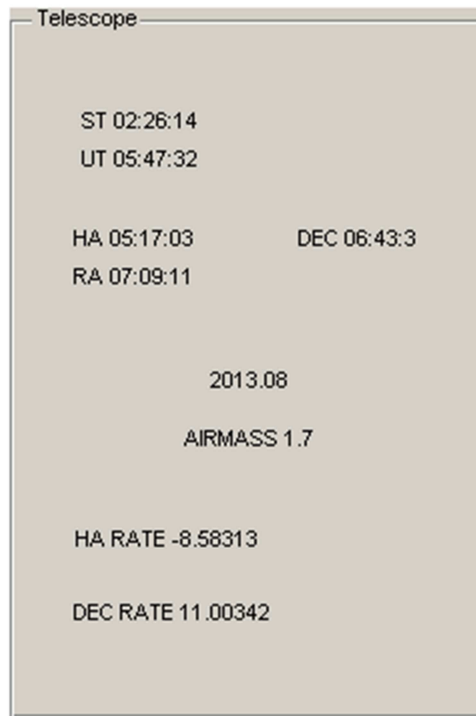


Figure 4.21 – Telescope’s information box

At the end of the observation is important to rest all the parameters and place the telescope in the parking position. A rest button has been implemented to do this. It is used to send the HA and DEC coordinates for parking spots, and it also sends the rates equal to zero and then terminates the TCP/IP connection (figure 4.22).

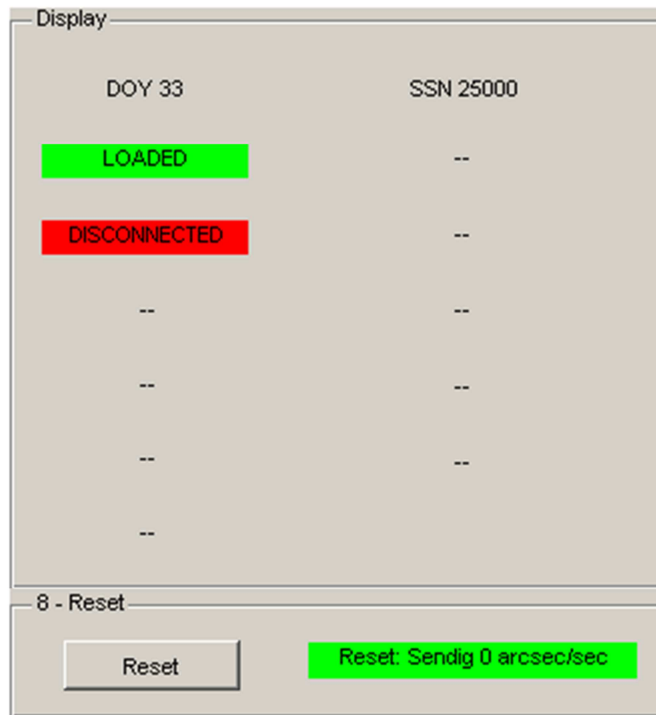


Figure 4.22 – Reset

4.5.1 – Test at Angel Hall Observatory

The GUI has been developed and tested for the first time at Angell Hall Observatory (figure 4.23). The observatory is run by the Astronomy Department of the University of Michigan and it is used for classes and public outreach. It is located inside the campus The main telescope is a 0.4 m Ritchey-Chretien reflector, equipped with a spectrograph and camera. The telescope is controlled by an old DOS based version of the MODEST control system and for this reason it has been a good test for the GUI (figure 4.24).



Figure 4.23 – Angell Hall telescope

The observatory is located inside the Central Campus on the top of the Angell Hall Building. Due to the location and the characteristics of the telescope it has been not possible to track GEO debris because they will be too faint. For this reason the test has been done by observing GPS satellites.



Figure 4.24 – Angell Hall Observatory TCS

Tracking a GPS satellite is even more challenging than tracking a GEO debris because the value of HA and DEC change more quickly as it possible to observe from figure 4.25 and 4.26 for position and rates respectively.

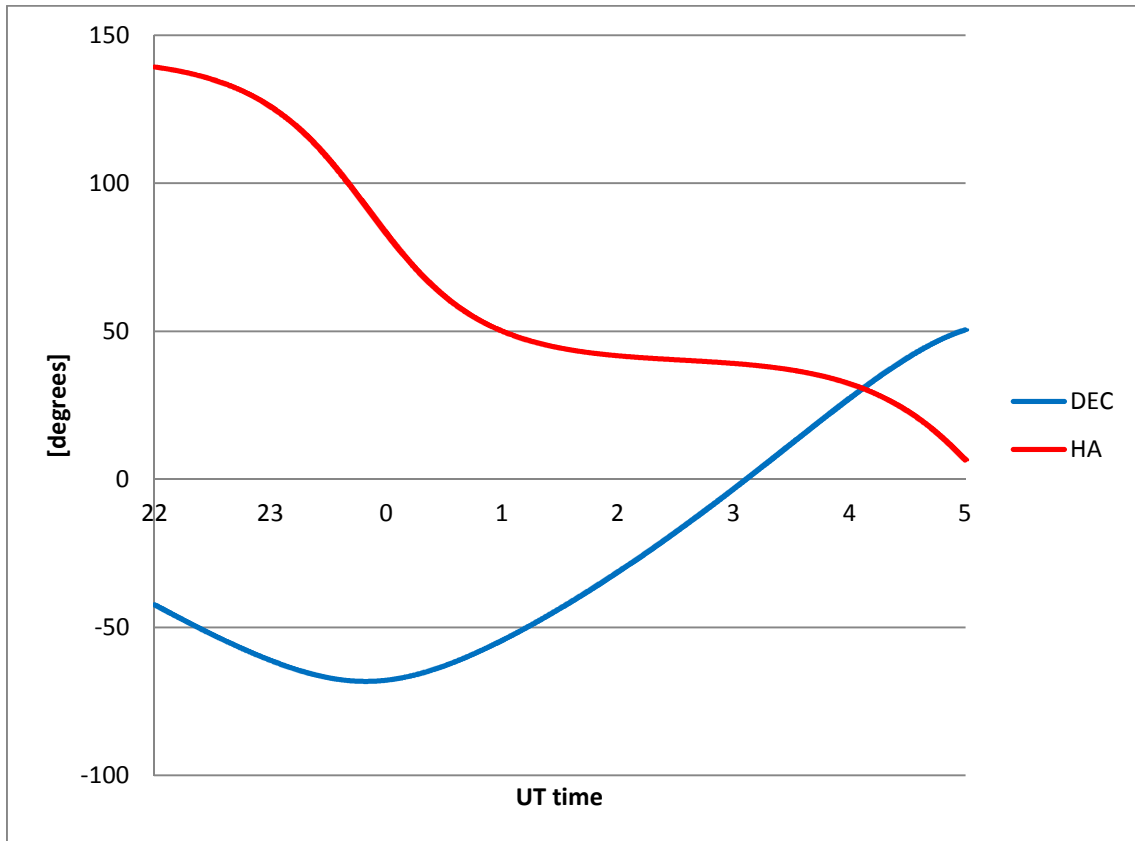


Figure 4.25 – HA and DEC position for GPS SSN 22014

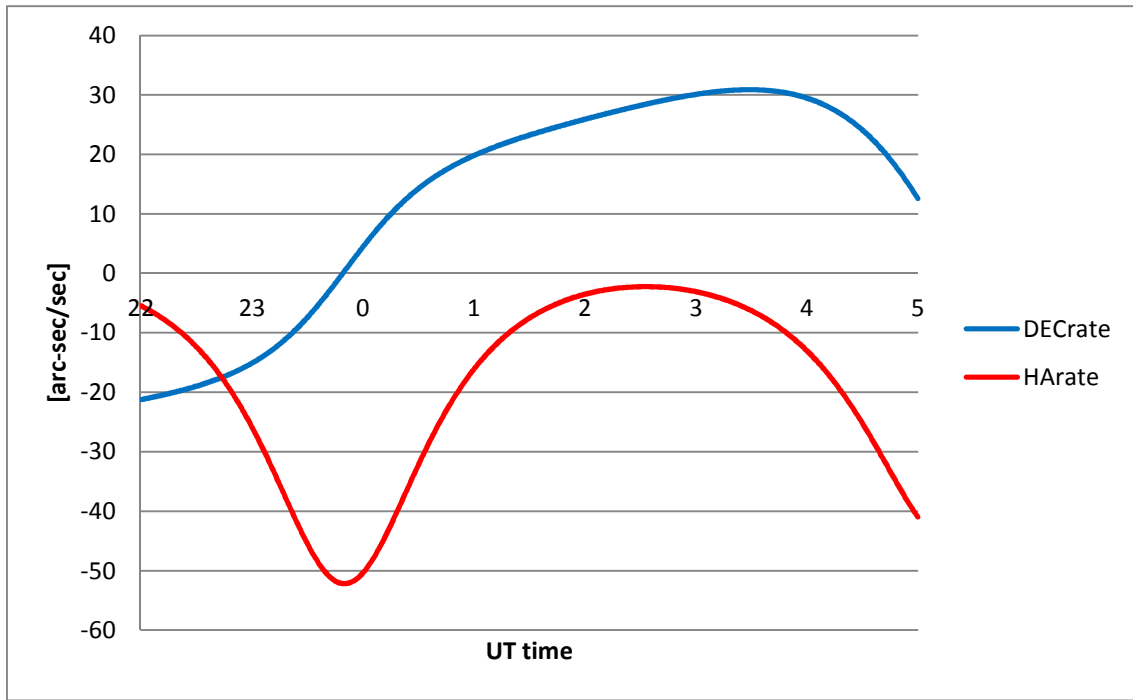


Figure 4.26 – HA and DEC rate for GPS SSN 22014

The observation has been planned with the software *STK 9* by finding which GPS satellites could be visible during the night from Angell Hall Observatory (see figure 4.27).



Figure 4.27 – STK simulation for Angell Hall Observatory

We found out that several satellites could be visible from the observatory and for this reason two different observation nights have been performed during August 2012. The list of observed targets is shown in Table 4.5.

Table 4.5
List of observed objects

Name	Type of object	Epoch of observation
SSN 35752	GPS satellite	14th and 15th August 2012
SSN 22014	GPS satellite	14th and 15th August 2012
SSN 28474	GPS satellite	15th August 2012

More than 1500 photometric pictures has been taken to test properly the GUI in particular the precision of large and small offsets (figure 4.28-30).

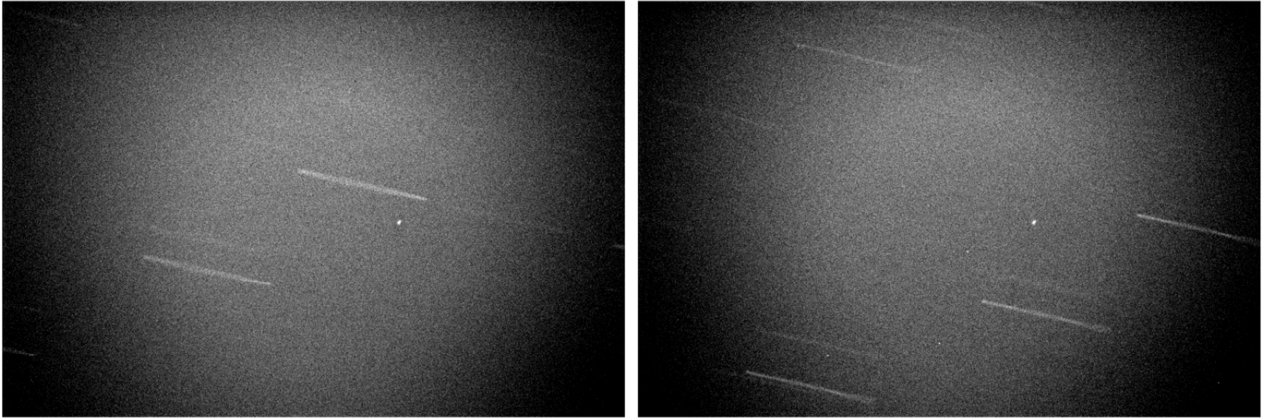


Figure 4.28 – The telescope follows the target SSN 35752 and keep it in the same point of the FOV

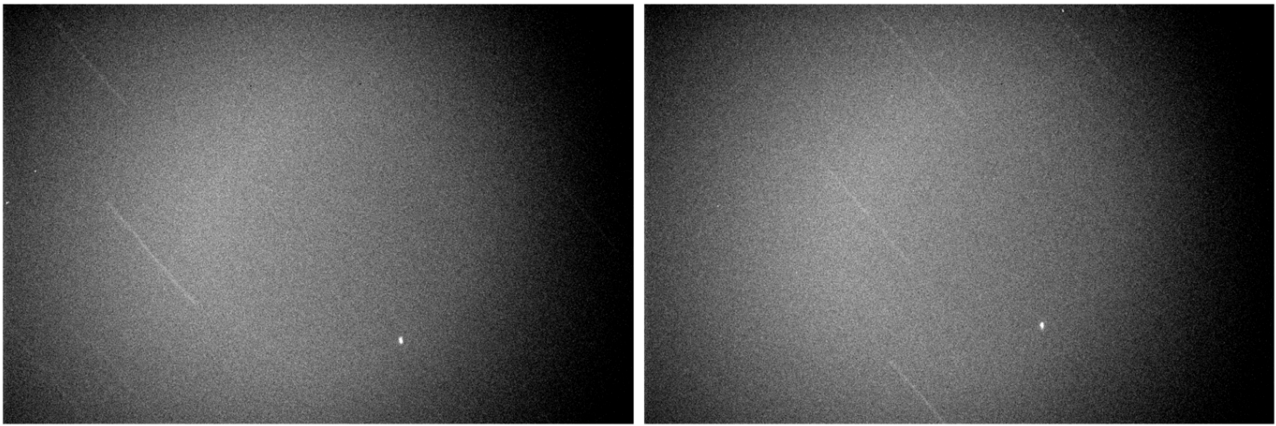


Figure 4.29 – Small offset test for SSN 28474

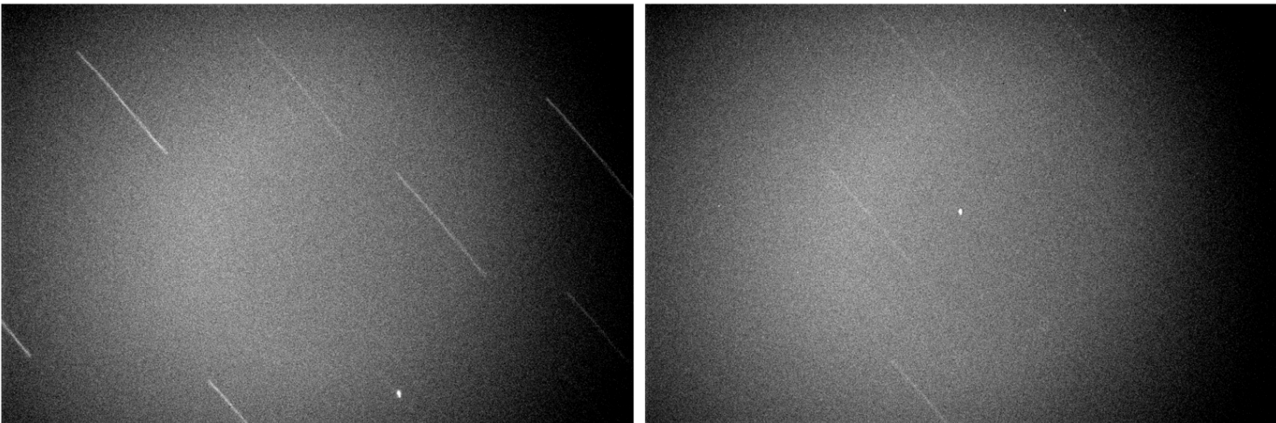


Figure 4.30 – Large offsets test in both HA and DEC for SSN 28474

As it possible to see from figure 4.28 the GUI enables tracking of satellites quite well, especially when the rates changes do not change so much from one step to the next one (when accelerations are low). This is also connected to the precision of the telescope mount which is not able to track with the necessary precision at such a high rate. The results of the large and small offsets have been satisfactory because they allow us to follow the target and place it into a specific point of the FOV with a reduced number of interactions.

Figure 4.31 shows the version of the GUI tested at Angell Hall during the observations.



Figure 4.31 – Test in Angell Hall

Chapter 5

Chile observing campaigns

The codes have been tested at the observatories in Chile during two different campaigns. The first one was carried out in May 2012 at Magellan and the first version of the non-sidereal tracking code was tested.

In January I personally participated to a three-day observing run for orbital debris on the 6.5 m Magellan-Clay telescope in order to perform optical spectroscopy of space debris for NASA's Orbital Debris Program Office and to implement directly the non-sidereal tracking programs that I had developed.

Moreover in the first week of February 2013 I had the opportunity to participate in a four-day observing campaign at Cerro Tololo Inter-American Observatory to perform photometry and to test the GUI on the Curtis-Schmidt telescope for the MODEST program.

5.1 – First test at Magellan Telescope in May 2012

The data collected were obtained on 1-2 May 2012 on the Landon Clay telescope (figure 5.1) with the spectrograph LDSS3. Five pieces of GEO or near-GEO debris were identified and observed with an exposure time of 30 seconds on average.



Figure 5.1 – Clay telescope

The targets for these first observations were whatever GEO objects satisfied the following criteria:

- Listed as debris in the public U.S. Space Command catalog.
- Were visible from Magellan at the time, were above a local airmass of 1.7, and not in eclipse.

Five objects satisfied these criteria on the observation nights available and are shown in Table 5.1

Table 5.1
List of observed objects

SSN	Launch Date	Description
12996	1977	EKRAN 2 DEB
13753	1976	LES 8,9/SOL 11A,B DEB
25000	1968	TITAN TRANSTAGE DEB
29014	1977	EKRAN 2 DEB
29106	2005	MSG 2 DEB (COOLER COVER)
02655	1967	IDCSP SATELLITE

Two of the observed objects had known characteristics at the time of their launch:

- SSN02651 - the IDCSP satellite known to be a 36 sided structure covered with solar cells [73]
- SSN29016 - a cover from the MSG2 spacecraft launched in 2005 and described in [74]

Unfortunately, it did not prove possible to schedule the observations to keep all objects within the same narrow range of solar phase angle.

Figure 5.2 shows the first spectrum of all six objects observed, after division by a spectrum of the solar analog SF1615, and smoothing. The final spectral resolution was about 10 Angstroms. All observations were normalized to 1.0 in the wavelength region from 7500 to 8000 Angstroms to allow easy comparison.

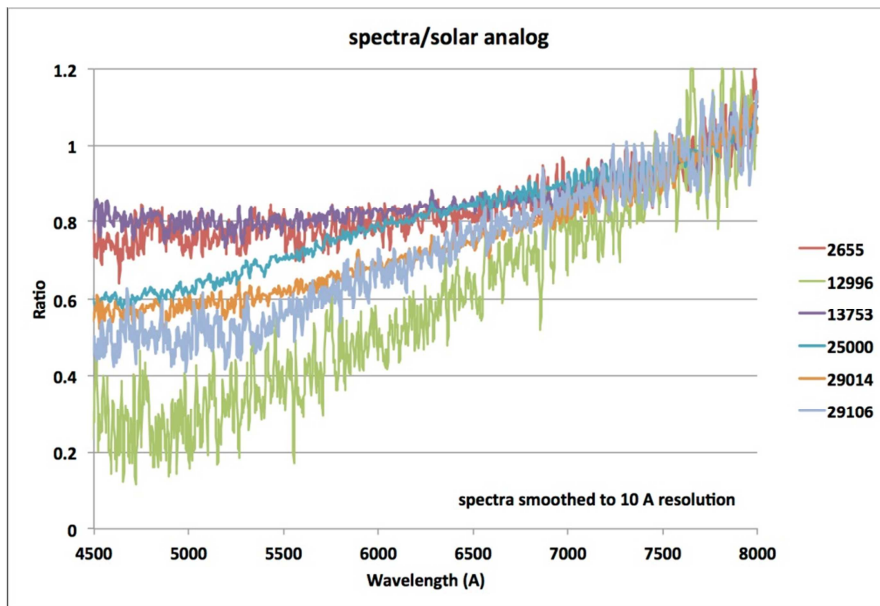


Figure 5.2 – Magellan LDSS3 spectra of 6 GEO or near GEO objects [49]

It is noteworthy that:

- All objects show a positive slope from blue to red, with an upturn redward of 7000 Angstroms.
- The IDCSP 2655 and 13753 (LES 8,9/SOL 11A,B) have flat responses shortward of 7000 Angstroms.
- The Ekran 2 debris piece 12996 has the greatest slope.
- The two pieces of Ekran 2 debris (12996 and 29014) have different slopes.

Figure 5.3 shows laboratory measurements from the NASA Spectral Library in the same spectral region of selected materials known to be on spacecraft. At first glance, there appears to be a substantial difference in the signature of these materials.

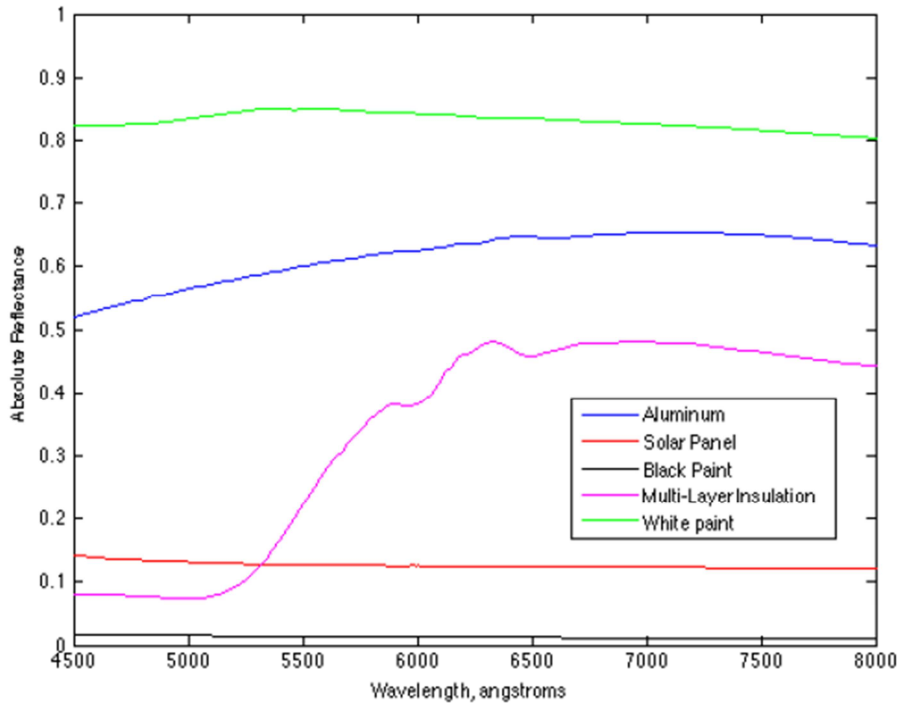


Figure 5.3 – Laboratory measurements of selected spacecraft materials [61]

But when taking laboratory measurements the amount of incident light is known. Figure 5.4 shows what the plot looks like if we treat the laboratory measurements in exactly the same manner as the telescopic observations, and normalize in the same wavelength region.

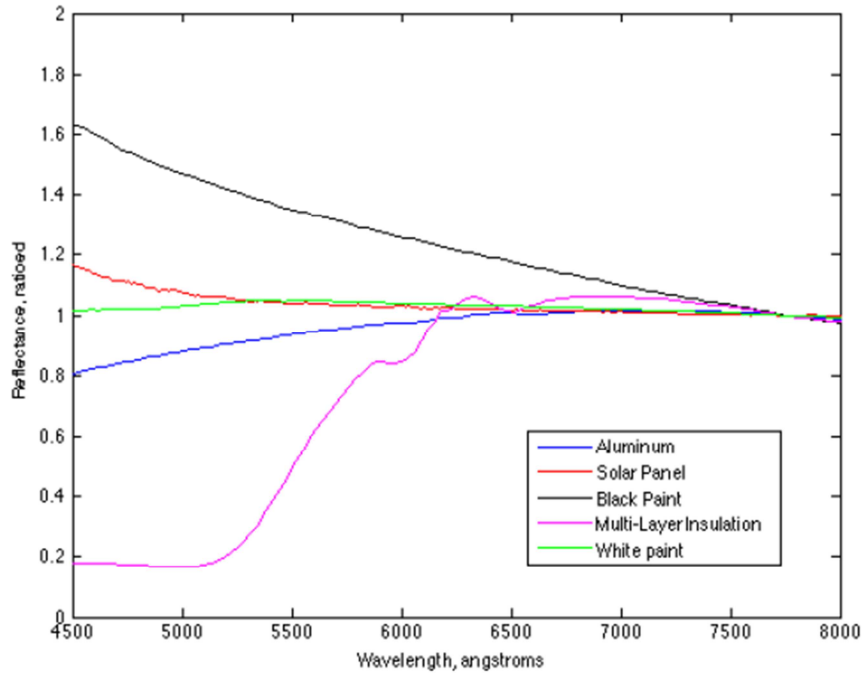


Figure 5.4 – Laboratory measurements treated normalized in the wavelength region 7500 to 8000 Angstroms [61]

In this simple example, there are three classes of materials that can be determined: black paint, the gold multi-layer-insulation, and all others. With high signal-to-noise observations, it might be possible to further distinguish the solar panels, aluminum, and white paint. But one should always keep in mind the differences in observing conditions between laboratory measurements and telescopic observations of GEO debris on orbit. The lab measurements are taken in atmosphere, presumably at the same phase angle, and with no space weathering effects.

The mystery of our Magellan observations is why most of them do not look anything like the laboratory results. The exceptions are the IDCSP 2655 and the debris piece 13753. They have flat response and compare well with laboratory measurements of solar panels, aluminum, and white paint except for the reddening beginning near 7000 Angstroms. All other debris pieces have spectrum unlike any of the laboratory measurements.

It is important to examine how the observed spectra correlate with other parameters: launch date and solar phase angle. Figure 5.5 shows the ratio of the debris spectrum divided by the solar analog star at 4500 Angstroms plotted against launch date. There is no correlation between launch date and the spectral ratio.

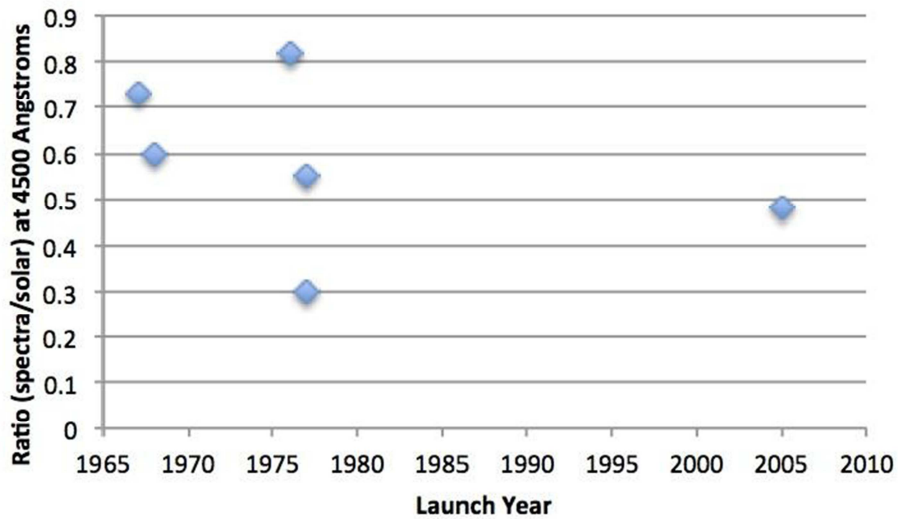


Figure 5.5 – Plot of spectral ratio at 4500 Angstroms versus launch date [61]

Of more concern is the solar phase angle distribution of our observations shown in figure 5.6.

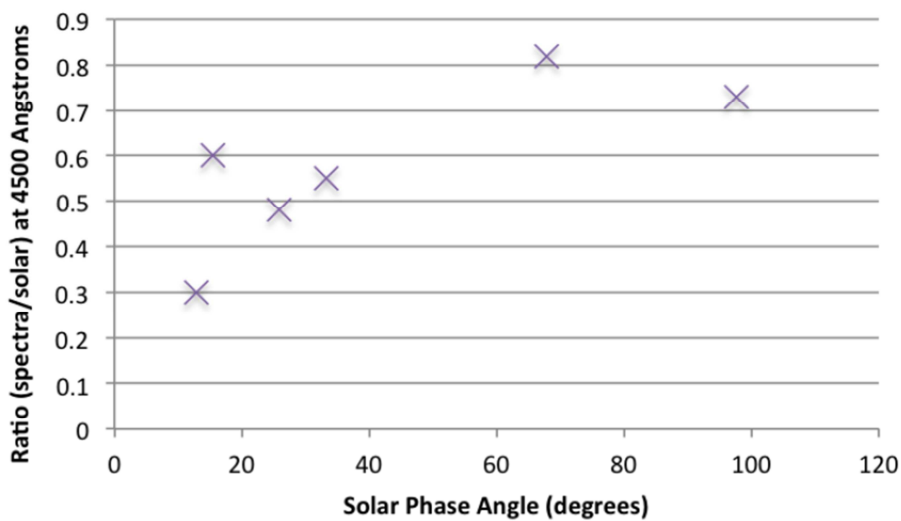


Figure 5.6 – Plot of spectral ratio at 4500 Angstroms versus solar phase angle at time of observation [61]

Although four of the debris pieces were observed in a fairly narrow range of phase angle between 10 and 40 degrees, scheduling constraints during the one half night that all of this data was obtained on meant that two of the objects (2655 and 13753) were obtained at much larger phase angles. These two objects have the flattest spectrum but it is not possible to say from the current small number data set whether this effect is real, or just a chance occurrence. In fact one can only speculate why most of the spectra do not compare well with any of the laboratory spectra of spacecraft materials.

Possible reasons include:

- We are seeing complex structures and not a simple surface during our 30 second exposure
- The object is rapidly tumbling and presenting multiple surfaces towards us during the exposure
- Phase angle differences discussed above
- Space weathering effects of surfaces with time
- All of the above.

5.2 – Test at Magellan Telescope in January 2013

In the last week of January 2013, I have participate to a three-day observing campaign at the Clay telescope at the Las Campanas Observatory (figure 5.7). The main goal of the campaign was to collect spectroscopic images of orbital debris with LDSS3.



Figure 5.7 – Clay Telescope

This running campaign gave me the opportunity to test the code that I have developed for blind non-sidereal tracking personally. Unfortunately, due to the extremely high cost of the telescope (several millions of USD), even if the GUI code had been developed to be functional also at Magellan, it is strictly forbidden to interface any personal laptop to the mount controlling station (figure 5.8) which is always operated by members of the staff of the Las Campanas Observatory who assisted me during the observing.



Figure 5.8 – Mount controlling station

While it is not possible to control the position of the telescope directly and it is still necessary to communicate the position to the Las Campanas Observatory technicians, the program enables the user to modify the rates of the telescope. In this way, it was possible to have the telescope follow the targets to keep them inside the slit. The control of the LDSS3 spectrograph during the observations has been performed and several objects were analyzed (figure 5.9).

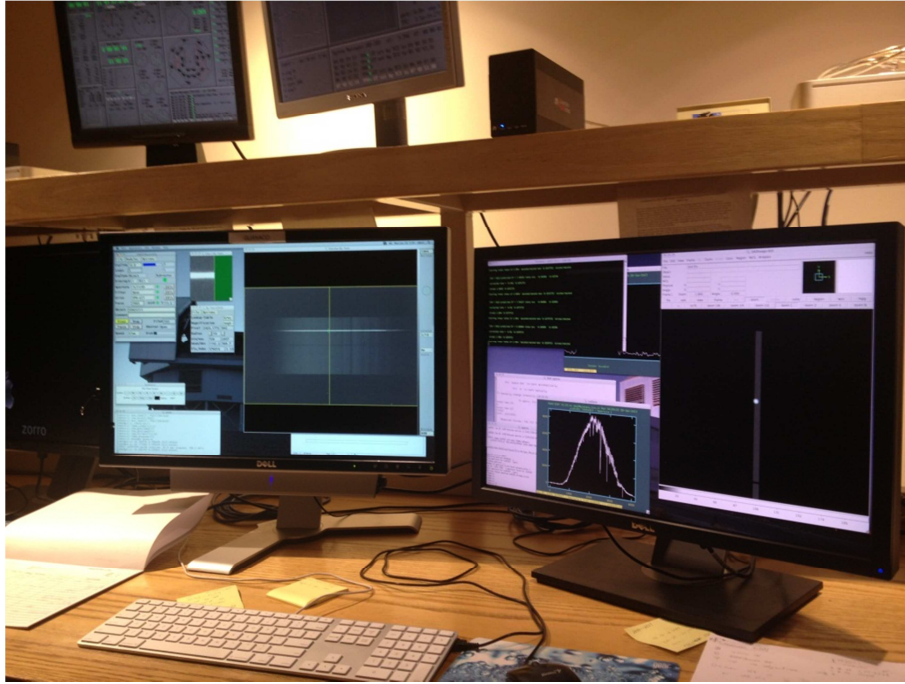


Figure 5.9 – LDSS3 controlling station

To date spectral observations of 13 GEO objects have been obtained on Magellan. We concentrated on pieces catalogued as debris in the SSN catalog, along with objects whose characteristics were known prior to launch:

- 5 pieces of debris from the Titan Transtage 3C-4 (1968-081) breakup in 1992: SSN 25000, 38690, 38691, 38699, and 38705.
- 4 other pieces of GEO debris: SSN 08832, 12996, 13753, and 29014
- 1 piece of GEO debris whose pre-launch characteristics are known: SSN 29106, the MSG2 Cooler Cover.
- 3 Initial Defense Communications Satellite Program (IDCSP) satellites whose original surfaces were very simple (solar cells) and known prior to launch: SSN 02653, 02655, and 03287.

5.2.1 – Results

All observations are normalized to 1 in the wavelength region 7500-8000 Angstroms.

5.2.1.1 – Titan IIIC Transtage debris

Observations of 5 pieces of Titan Transtage 1981-081 debris and one piece of debris from the Titan Transtage 1976-023J (SSN08832) were obtained and are displayed in figure 5.10.

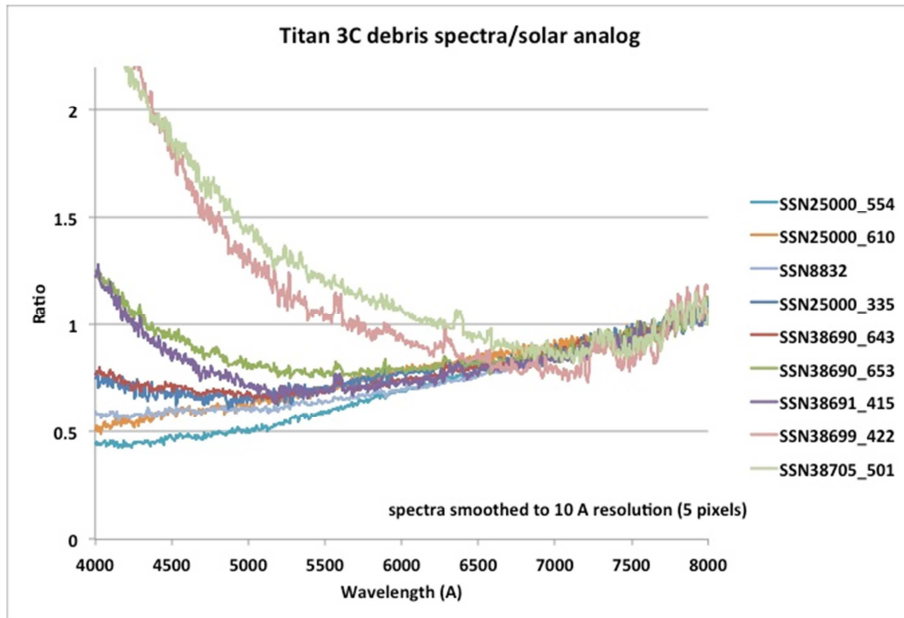


Figure 5.10 – Observed spectrum of Titan Transtage debris after division by a spectrum of a solar analog standard star [63]

For SSN25000, we obtained observations on 3 different nights, and these spectra are shown in figure 5.11.

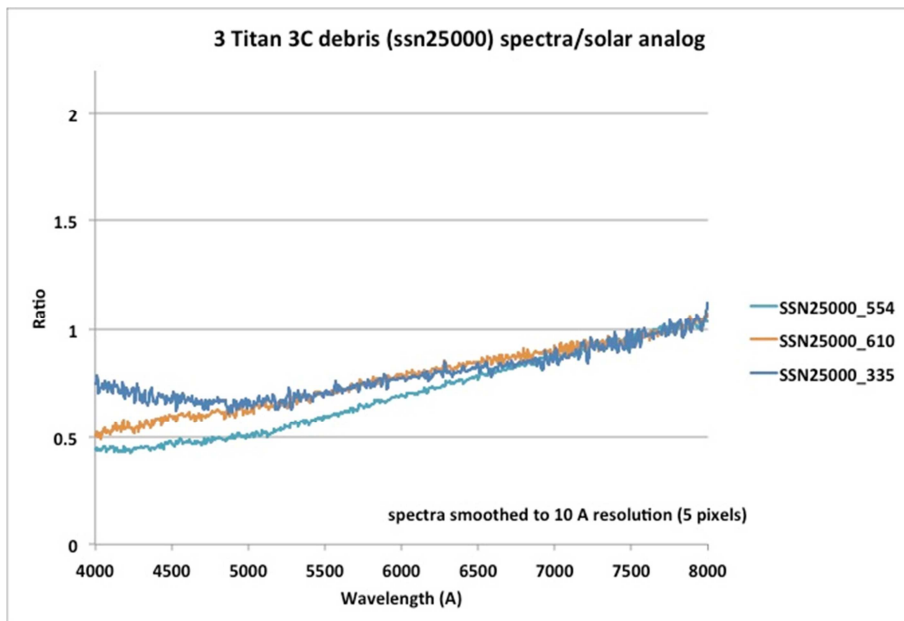


Figure 5.12 – Repeat observations of the Titan Transtage debris piece SSN25000 on 3 different nights [63]

There are several reasons why the observed differences may be larger than the expected errors:

1. A problem with the absolute calibration in the blue on one or more of the nights observed.
2. We are seeing different parts of this object as its attitude changed between the various observations.

5.2.1.2 - Other GEO Debris

Observations of an additional four objects classified as debris in the public catalog were obtained and are shown in figure 5.12.

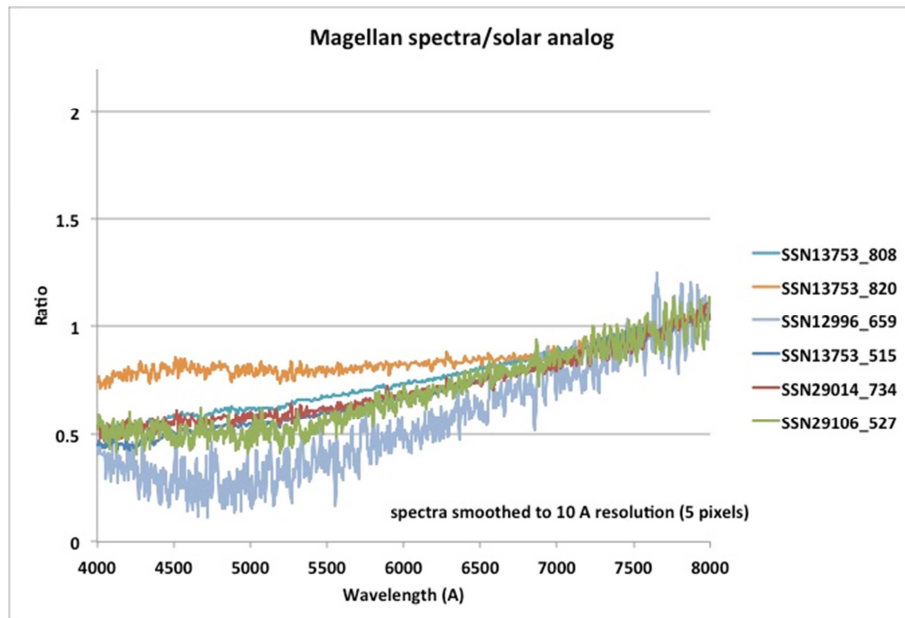


Figure 5.12 – Observations of non-Titan GEO debris pieces obtained with Magellan [63]

These pieces show less variation in spectral slope than the Titan debris sample.

For SSN13753, multiple observations were obtained on all three nights, and the individual spectra are shown in figure 5.13.

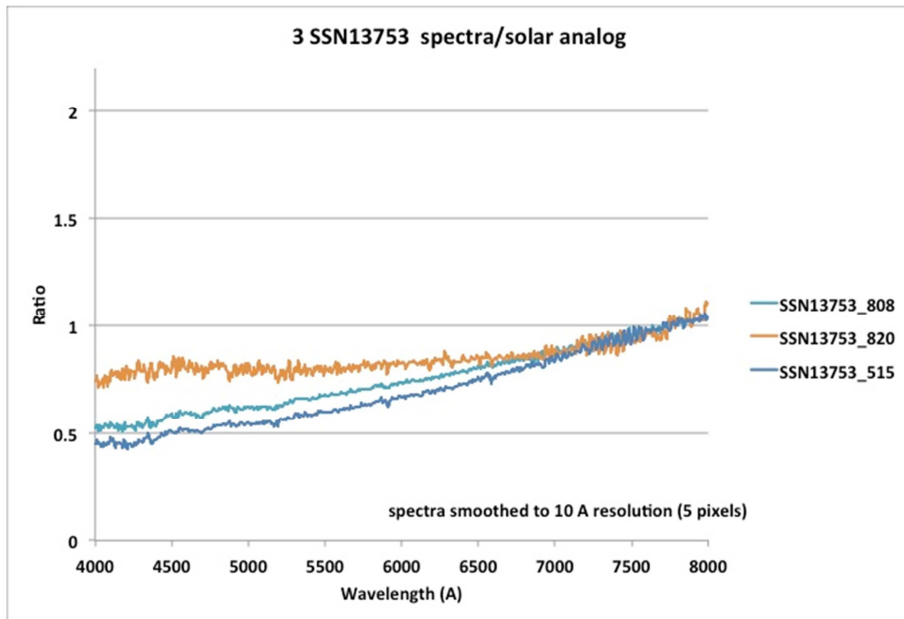


Figure 5.13 – Repeat observations of SSN13753 [73]

For this object, the agreement on two of the nights is quite good over the full wavelength range, but for the third observation the agreement is less good. The difference is larger than would be expected for calibration errors, and thus could indicate that we are seeing a different part of a tumbling, uncontrolled object on this night.

5.2.1.3 – IDCSP Observations

Just below the GEO regime is the constellation of the Initial Defense Communications Satellite Program (IDCSP) satellites. These were launched in the 1960s. These are of particular interest because of their very simple and uniform construction: 26 sided polygons completely covered in solar panels and just smaller than 1 meter in diameter.

They offer the possibility of a uniform sample of objects at launch, whose launch characteristics are known, for comparison with laboratory measurements.

Spectra of three objects were obtained, and are shown in figure 5.14

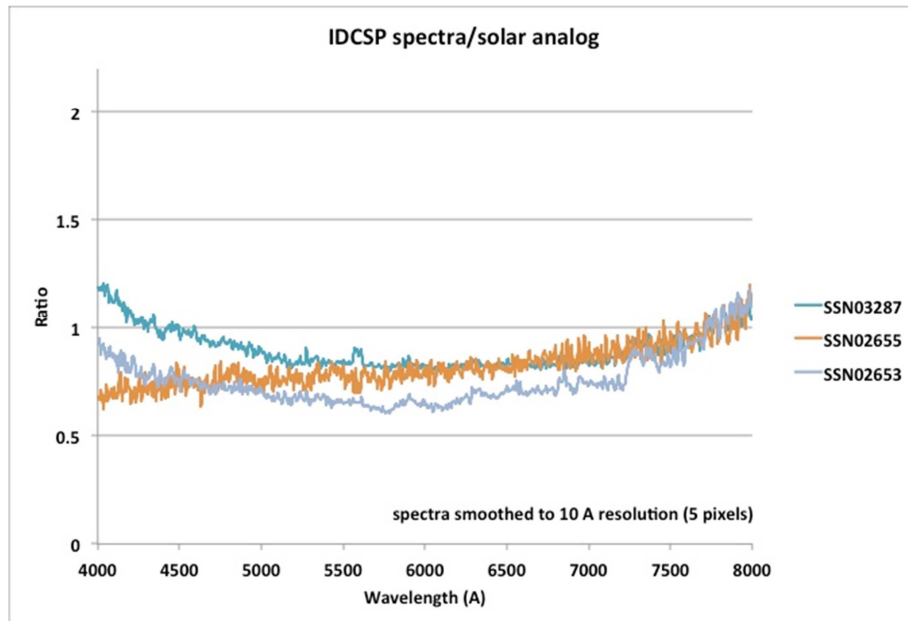


Figure 5.14 – Normalized spectra of three IDCSP satellites obtained with Magellan [63]

The agreement between the three spectra is reasonable, and much better than what was seen in the other two samples of GEO debris observed.

5.2.3 – Results discussion

The Magellan spectra show a wide range of spectral slopes from blue to red. As previously mentioned, laboratory measurements of materials used in spacecraft construction were used for comparison as seen in figure 5.4 .

With the exception of the black paint and the solar panel, there is no good agreement between any of the laboratory curves and the observed spectra. There are a number of reasons why this is not an unexpected result:

1. The observed spectra are of a complex surface with multiple materials contributing to the flux measured at the telescope. More sophisticated models incorporating a mix of materials may be required.
2. Related to this effect may be that the spectra are time averaged over the length of the exposure. If an irregularly shaped object does not have a constant attitude during the exposure, then a model requiring a mix of materials and sizes related to its and tumbling rate may be required as well.

3. Nothing is known about the orientation with respect to the Sun and observer of the surface(s) contributing to a spectrum. The topocentric solar phase angle (defined as the angle between the Sun, observer, and object) is known, but it is the only angle we can compute. To first order this is also the angle between the incident and reflected rays at the object, but this tells the observer nothing about their relationship to the surface normal. These rays could be on the same side of the normal vector, or on different sides. Bédard [79] discusses the importance of knowing the reflected angle to predict the observed spectral response. And with regard to point 2 above, the normal vector could be changing even during short exposure times for an object that is rapidly tumbling or rotating.
4. The effects of the space environment ("*space weathering*") have not been included. One is tempted to look at the space weathering histories of well-studied asteroids for guidance here, but we are not optimistic that this will be an easy task. Gaffey [81] points out the asteroids 433 Eros and 243 Ida have very different space weathering styles, and both are different from space weathering effects on the Moon. Gaffey [81] goes on to point out that analysis based on band characteristics is invaluable in such studies, but there are no bands other than solar and telluric expected from typical debris surfaces in these spacecraft materials visible spectra. Reflectance curve analysis similar to that presented here is the only diagnostic tool available.

It is likely that a full interpretation of the observed spectra will require a sophisticated model incorporating different materials, a range of incident and reflected angles, and space weathering effects.

Because the spectra show a wide range of slopes, and do not compare well in a simple comparison with laboratory measurements of spacecraft materials it is probable that more sophisticated modeling will be required for interpretation of these spectra.

5.3 – Test at MODEST in February 2013

On February 2013 an observation campaign at MODEST has been performed (figure 5.13). The main purpose of the campaign was to execute photometric observation of space debris. Moreover during the observing nights I had the opportunity to implement the GUI on the WinTCS (figure 5.14, 5.15) that controls the telescope to test it.

Some modification on the code has been necessary, in fact the GUI has been developed at the Angell Hall Observatory where the telescope is controlled by an old DOS-based version of TCS. The main differences consist in a different communication protocol. After making these changes to the code, the GUI started working properly.



Figure 5.13 – MODEST Dome

The GUI has been tested to follow in particularly two different GEO debris target, SSN25000 and SSN24313. In particular SSN25000 is an orbital debris from the breakup of a Titan 3C-4 Transtage on 21 February 1992 which has been observed many times at Magellan [78].

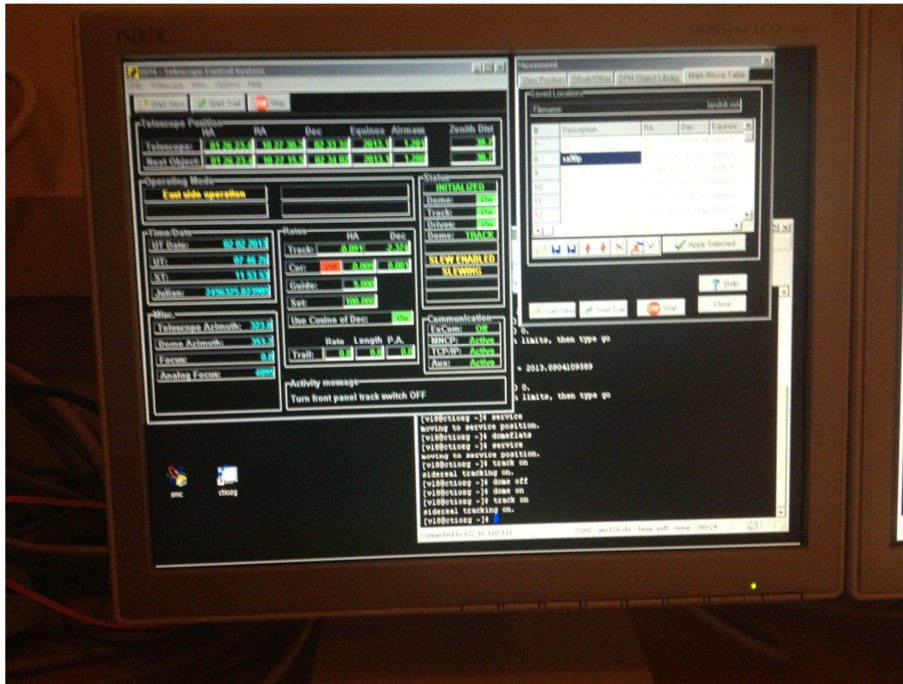


Figure 5.14 – WinTCS at MODEST

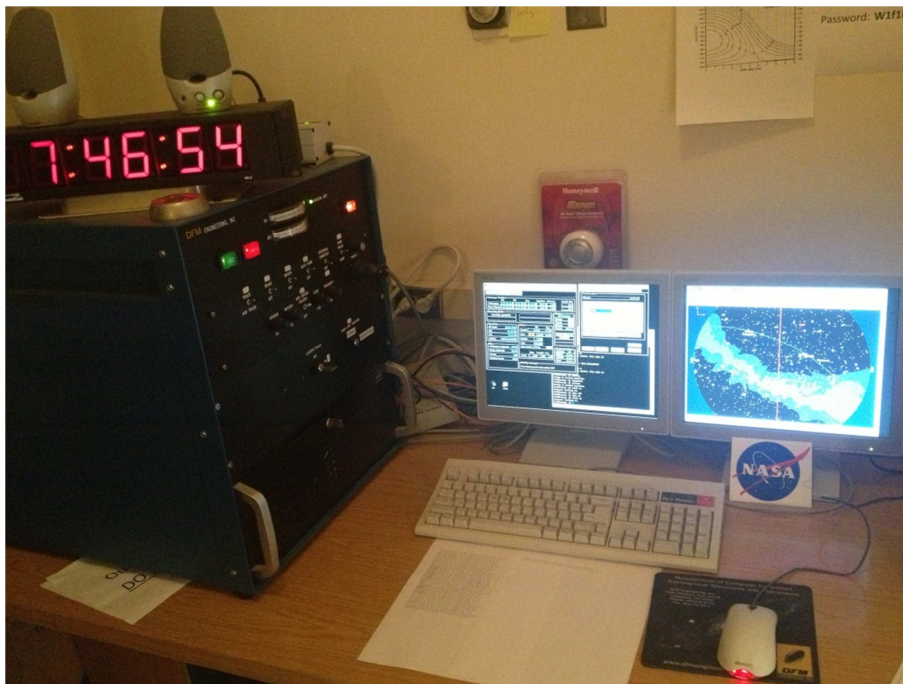


Figure 5.15 – WinTCS and DFM Control System at MODEST

Figure 5.16 shows the use of the GUI during one observing nights. The DFM control box is seen on the left, WinTCS can be seen running on the central screen, and initialization of the GUI is taking place on the laptop seen on the right. After checking every command independently, the main code has been tested.



Figure 5.16 – Testing the GUI on MODEST

More than 500 photometric pictures were taken to test the GUI at MODEST in order to test the precision of large and small offsets as performed previously at Angell Hall (figure 5.17).

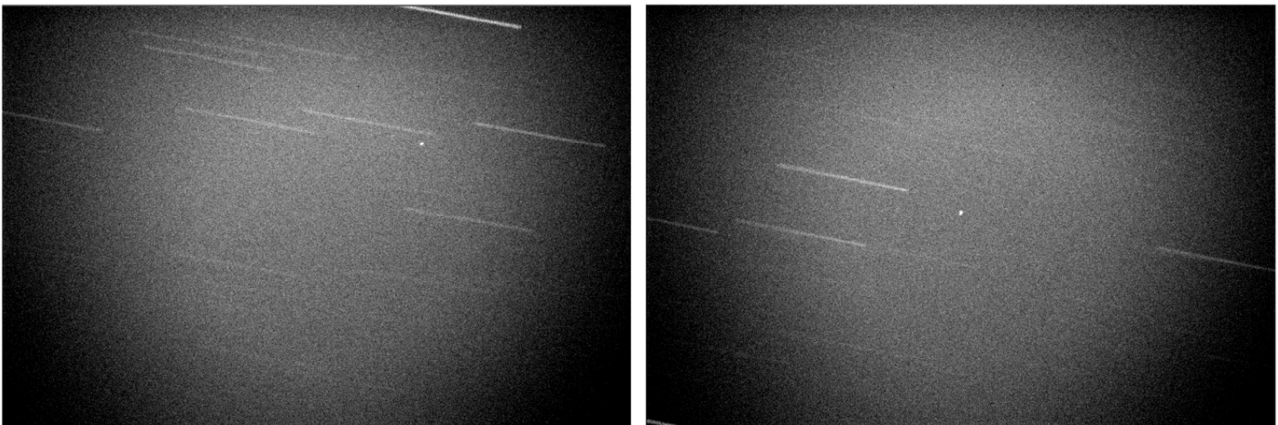


Figure 5.17 – Offset test at MODEST

Chapter 6

Conclusions

6.1 – ALMASCOPE conclusion

The feasibility of establishing an observatory for space debris at the Broglio Space Centre in Malindi (Kenya) has been demonstrated as a result of an observation campaign performed in September 2010, based on the model of the standard IADC survey campaign in HEO. By comparing statistical results of the surveys obtained in Malindi using the ALMASCOPE observatory with literature data, a good agreement was found, showing that, though operating at sea level, the site is suitable for space debris observation.

6.2 – Loiano observation campaign conclusion and future work

The measurements acquired in the observing nights at Loiano telescope are in good agreement with the data from other international groups and can give a first impression of the physical nature of the targets. In particular, two HAMR objects were observed. One of them, HAMR 84980, shows large variations in magnitude typical of the HAMR objects and has color indexes that are very similar to laboratory copper-colored Kapton samples. The other one, HAMR 84967, has a less extreme lightcurve and less conclusive compositional indications, with color indexes close to those of laboratory Mylar samples [43]. Moreover two clearly distinct slopes in the reflectance were identified for large intact RB and for HAMR objects [44] permitting to conclude that different object could be classified by their photometric signature.

The results of the two August 2011 nights of photometric observations from the Loiano telescope confirm that this telescope can be an interesting instrument for this kind of studies thus.

The project is continuing and two more observation nights are scheduled in December 2013. This will allow us to build a more consistent database of objects and to check our conclusions on the slopes of the reflectance, over a significant sample of GEO targets.

6.3 – Future work with NASA Orbital Debris Program Office

The final goal for the project coordinated by the NASA Orbital Debris Program Office is to use infrared spectrographs such as FIRE on the Magellan telescope Walter Baade to provide spectroscopy of debris from 800 nm to 2.5 microns. This will complement visual data from 400 nm to 800 nm with imaging spectrographs such as IMACS and LDSS3. In fact object could be tumbling at unknown orientation and rates, therefore necessitating simultaneous observations at all wavelengths.

Unfortunately the widest slit available on FIRE is 1 arc-sec and this cannot be changed [57].

The main idea is to find if there is a way to update orbit with MODEST prior to the start of Magellan observing that is accurate and precise enough for observing with a 1 arc-second slit.

Before improving the orbit, several questions have to be answered:

- How many days before the Magellan run starts do we need to start MODEST observations?
- How many observation sets per night per object are required?
- How do we represent mathematically the updated orbit?
- How do we minimize acquisition observations on Magellan, which will maximize time spent in spectrographic observations?

As previously said in chapter 4, the position of the satellite comes from NASA in .MLB files in which the orbit is propagated starting from TLEs with a SGP orbit propagator. The main problem with this method is that unfortunately, the SGP orbital data, in the form of TLE sets, does not provide any kind of accuracy information. Some approaches have been published to estimate these errors by performing consistency or checks, but they do not validate their assumptions or provide any validation by comparison to high-accuracy ephemerides.

According to T.S. Kelso [68]:

- Errors associated with almanac and TLE predictions are comparable, at least within 15 days of the epoch, although almanac predictions are much better near the epoch.

- TLE consistency analysis does reasonably approximate the true error of a TLE prediction, both in propagation time, direction, and overall magnitude, although it does underestimate it near the epoch.
- There are clear biases in the TLE errors which, if not accounted for, can lead to an overestimation of the error. It should, however, be possible to improve a TLE estimate by estimating and removing this bias. Not only would the estimate improve but the associated error would decrease, thereby increasing the overall confidence in the resulting prediction.
- Error characteristics for satellites in similar orbits can be considerably different. Consequently, the error characteristics of each satellite should be determined independently.

To follow up on this study, an Extended Kalman filter based on measures taken from the Curtis-Schmidt telescope is being developed. In this way, we hope to obtain a better simulation of the orbit.

Appendix

A.1 – Celestial Equatorial Coordinate System

The *Celestial Equatorial Coordinate System* is based on the theory of the celestial sphere, that is an imaginary sphere with infinite radius that is surrounding the earth. The position of objects in the sky are given by projecting their location onto this sphere. While technically impossible to represent the perspective of looking down on the celestial sphere that is infinite in size, it is usually represent a celestial sphere with a finite radius (figure A.1).

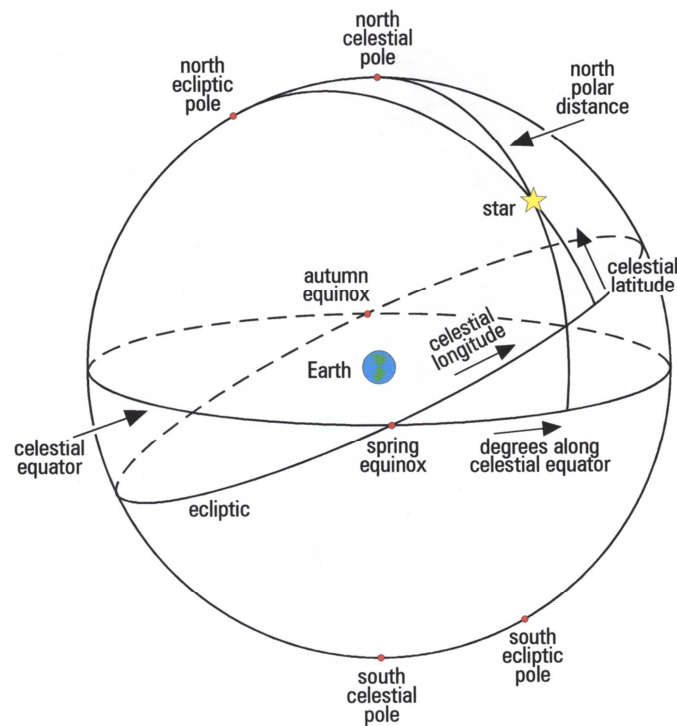


Figure A.1 – Celestial sphere [75]

The celestial sphere is immobile respect to the universe and its alignment does not change. But due to the earth rotation from west to east (counterclockwise from the viewpoint of looking down at the north pole),

an observer standing on the earth will see the celestial sphere rotate from east to west (or clockwise while observing at sky).

Alike terrestrial coordinates (e.g. longitude and latitude), two coordinates are defined to represent a point on the celestial sphere. The rotation of the earth defines a direction in the universe and it is convenient to base a coordinate off that rotation/direction. The celestial equator is the line coplanar with the earth's equator. The north celestial pole is straightly above the earth's north pole and similarly for the south celestial pole. The coordinate representing where an object is between those poles is declination.

Declination is measured from the celestial equator. It ranges from 0° at the celestial equator to $+90^\circ$ at the north celestial pole and from 0° down to -90° at the south celestial pole.

The second coordinate is *right ascension* that could be considered analogous to longitude. Much as Greenwich is the arbitrary zero point for longitude, right ascension also has a zero reference point that coincides with the Vernal Equinox Point. For the reason that the earth rotates, from the perspective of the earth, the celestial sphere rotates once about every 24 sidereal hours. Right ascension, consequently, is measured in sidereal hours too, 0h to 24h east from the Vernal Equinox Point. East is the direction of growing right ascension. The half-circle with right ascension 0h is called the 0 hour circle. 1 hour right ascension is equal to an arc of 15° .

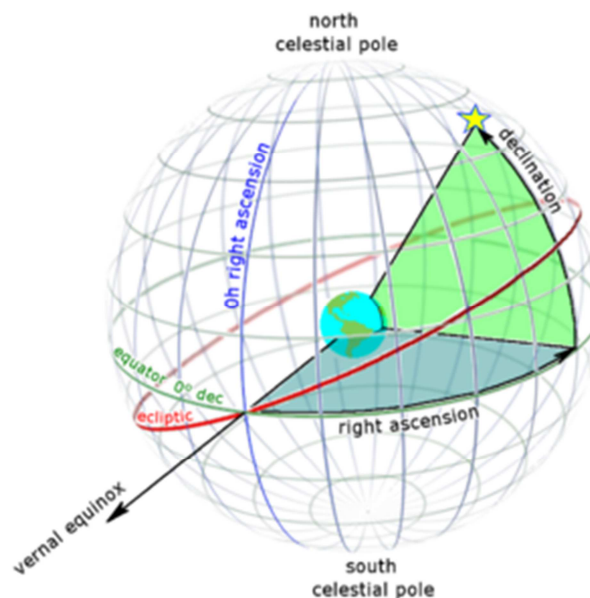


Figure A.2 – Declination and right ascension [76]

The right ascension of an object indicates the Sidereal Time at which an object will transit across local meridian. It is possible to define the Hour Angle that is specify as the difference between the current Local Sidereal Time and the right ascension of the object:

$$HA_{obj} = LST - RA_{obj} \tag{A.1}$$

Consequently, the object's Hour Angle indicates how much Sidereal Time has passed since the object was on the Local Meridian.

A.2 - Definition of Two-line Element Set Coordinate System

A NORAD two-line element set contains two lines of data composed by 69-character which can be used with NORAD's SGP4/SDP4 orbital model to determine the position and velocity of the related satellite. The only valid characters in a two-line element set are the numbers 0-9, the capital letters A-Z, the period, the space, and the signs like plus and minus.

Figure A.3 shows an example for a TLE.

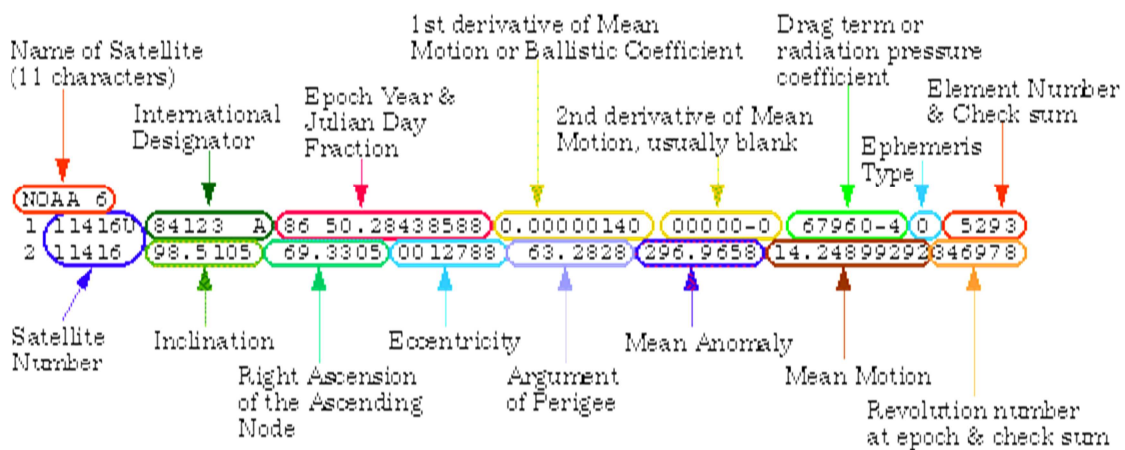


Figure A.3 – TLE example for NOAA 6 (SSN 11416) [77]

The TLE set is composed of multiple parts [77]:

- The **Name of Satellite** is the name related with the satellite
- The **International Designator** indicates launch year and the number of the launches of the year before the one that put the satellite into orbit.
- The **Epoch Date and Julian Date Fraction** the data of the launch. In particular the Julian day fraction is just the number of days passed in the year.
- The **Ballistic Coefficient** (also called the first derivative of mean motion) is the daily rate of change in the number of revs the object completes each day, divided by two. Units are revs/day.
- The **Second Derivative of Mean Motion** is a second order drag term in the SGP4 predictor used to model terminal orbit decay. It measures the second time derivative in daily mean motion, divided by 6. Units are revs/day³.
- The **Drag Term** (also called the radiation pressure coefficient or BSTAR), is a drag term in the SGP4 propagator. Units are earth radii⁻¹.
- The **Element Set Number and Check Sum** is a running count of all 2 line element sets generated by USSPACECOM for the object. The last digit is the check sum for line 1.
- The **Satellite Number** is the catalog number that USSPACECOM has designated for the object. A "U" indicates an unclassified object.
- The **Inclination** is the angle in degrees between the equator and the orbit plane. The value provided is the mean inclination.
- The **Right Ascension of the Ascending Node** is the angle in degrees between vernal equinox and the point where the orbit crosses the equatorial plane (going north). The value provided is the mean right ascension of the ascending node.
- The **Eccentricity** is constant defining the shape of the orbit. If it is equal to 0 the orbit is circular, while if it less than 1 the orbit is elliptical. The value provided is the mean eccentricity.
- The **Argument of Perigee** is the angle in degrees between the ascending node and the orbit's point of closest approach to the earth (perigee). The value provided is the mean argument of perigee.
- The **Mean Anomaly** is the angle, measured in degrees from perigee, of the satellite location in the orbit referenced to a circular orbit with radius equal to the semi-major axis.
- The **Mean Motion** is the mean number of orbits per day the object completes.
- The **Revolution Number and Check Sum** is the orbit number at Epoch Time. The last digit is the check sum for line 2.

Bibliography

A. B. Roy, *"Orbital Motion"*, Adam Hilger, 1991

D. A. Vallado, W. D. McClain, *"Fundamentals of Astrodynamics and Applications"*, Space Technology Library, 2007

H. Klinkrad, *"Space Debris: Models and Risk Analysis"*, Springer Praxis Books, 2006

Interagency Group Space, *"Report on Orbital Debris"*, National Security Council, 1989

J. J. Poeha, *"An Introduction to Mission Design for Geostationary Satellites"*, Reidel Publishing Company, 1987

J. M. A. Danby, *"Fundamentals of Celestial Mechanics"*, Macmillan, 1962

J. R. Wertz, *"Spacecraft Attitude Determination and Control"*, Astrophysics and Space Science Library, 1980

J. R. Wertz, W. J. Larson, *"Space Mission Analysis and Design"*, Space Technology Library, 1999

K. J. Abercromby, P. Seitzer, H. M. Cowardin, E. S. Barker, M. J. Matney, *"Michigan Orbital DEbris Survey Telescope Observations of the Geosynchronous Orbital Debris Environment"*, NASA/TP-2011-217350, 2010

P. R. Escobal, *"Methods of Orbit Determination"*, Krieger Publishing Company, 1965

R. E. Kalman, *"A New Approach to Linear Filtering and Prediction Problems"*, ASME-Journal of Basic Engineering, 1960

R. G. Brown, P. Y. C. Hwang, *"Introduction to Random Signals and Applied Kalman Filtering"*, John Wiley and Sons, 1992

R. H. Battin, *"An Introduction to the Mathematics and Methods of Astrodynamics"*, AIAA Education Series, 1999

R. R. Bate, D. D. Mueller, J. E. White, *"Fundamentals of Astrodynamics"*, Dover Publications, 1971

V. A. Chobotov, *"Orbital Mechanics"*, AIM Education Series, 2002

W. E. Wiesel, *"Spaceflight Dynamics"*, McGrawHill Book Company, 1996

Reference

- [1] <http://nssdc.gsfc.nasa.gov/nmc/SpacecraftQuery.jsp>
- [2] <http://www.cmp.caltech.edu/refael/league/CPL1.html>
- [3] <http://nssdc.gsfc.nasa.gov/nmc/spacecraftDisplay.do?id=1961-015A>
- [4] D. S. F. Portree, J. P. Loftus, *“Orbital Debris - A Chronology”*, NASA/TP-1999-208856
- [5] *IADC Space Debris Mitigation Guidelines, 2002*
- [6] Forum Session *“Mission Models and Space Planning”* held at the congress of the International Astronautical Federation (IAF) in Munich September 17, 1979
- [7] http://www.nasa.gov/mission_pages/station/news/orbital_debris.html
- [8] <http://www.agi.com/media-center/multimedia/current-events/iridium-33-cosmos-2251-collision>
- [9] <http://www.thespacereview.com/article/1417/1>
- [10] *NASA Orbital Debris Quarterly News*
- [11] T. Schildknecht, *“Optical astrometry of fast moving objects using CCD detectors”*, Geod.-Geophys. Arb. Schweiz, No. 49, 1994.
- [12] C. Fruh, T. Schildknecht, *“Variation of Area-to-Mass-Ratio of HAMR Space Debris Objects”*, Monthly Notices of the Royal Astronomical Society Volume 419, Issue 4, pages 3521–3528, February 2012
- [13] C. Fruh, T. Schildknecht, *“Investigation of Properties and Characteristics of High-Area-to-Mass-Ratio Objects Based on Examples of Optical Observation Data of Space Debris Objects in GEO-like Orbits”*, AMOS 2010 conference
- [14] W. Romanishin, *“An Introduction to Astronomical Photometry Using CCDs”*, University of Oklahoma Press, 2006
- [15] P. Massey, M. M. Hanson, *“Astronomical Spectroscopy”*, Cornell university Library, 2011
- [16] A. Landolt, *“UBVRI Photometric Standard Stars in the Magnitude Range $11.5 < V < 16.0$ Around the Celestial Equator”*, Astron. J 104:340 (1992).
- [17] A. Landolt, *“Broadband UBVRI Photometry of the Baldwin-Stone Southern Hemisphere Spectrophotometric Standards”*, Astron. J. 104:372 (1992).
- [18] http://imagine.gsfc.nasa.gov/docs/science/how_l1/light_curves.html
- [19] <http://www.satobs.org/tumble/tumbleintro.html>
- [20] F. Santoni, E. Cordelli, F. Piergentili, *“Rocket body rotation state estimation by remote optical observation”*, 63rd International Astronautical Congress Naples, Italy, 1-5 October 2012

- [21] S. Lederer, P. Seitzer, H. Cowardin, K. J. Abercromby, E. Barker, A. Burkhardt, "Characterizing Orbital Debris and Spacecrafts Through a Multi-Analytical Approach", AMOS 2012 conference
- [22] R. Binzel, C. Thomas, F. DeMeo, A. Tokunaga, A. Rivkin, S. Bus, "The MIT-Hawaii-IRTF Joint Campaign for NEO Spectral Reconnaissance, 37th Annual Lunar and Planetary Science Conference", March 13-17, 2006, League City, Texas, abstract no.1491, 2006.
- [23] IADC, "Report on action item 23.4", International 2007 Optical Debris Campaign in Higher Orbit
- [24] F. Piergentili, A. Ceruti, F. Rizzitelli, T. Cardona, M. L. Battagliere, F. Santoni, "Space debris measurement using joint mid-latitude and equatorial optical observations". Transactions on Aerospace and Electronic Systems, IEEE. In print (2013)
- [25] D. A. Vallado, T.S. Kelso, V. Agapov, I. Molotov, "Orbit Determination Issues And Results To Incorporate Optical Measurements In Conjunction Operations".
- [26] James G. Miller, "Covariance Analysis For Deep-Space Satellites With Radar And Optical Tracking Data", AAS/AIAA Astrodynamics Specialists Conference, Lake Tahoe, CA, August 7-11, 2005, AAS Publications, San Diego, CA
- [27] F. Santoni, F. Piergentili, R. Ravaglia, "Nanosatellite Cluster Launch Collision Analysis", Journal of Aerospace Engineering.
- [28] Alarcon J.R., Klinkrad H., Cuesta J., Martinez F.M., "Independent orbit determination for collision avoidance", Proceedings of the fourth European Conference on Space Debris, Darmstadt, Germany, 18-20 April 2005
- [29] R. G. Gottlieb, S. J. Sponaugle, D. E. Gaylor, "Orbit Determination Accuracy Requirements For Collision Avoidance", AAS 01-181, Volume 108, Part II, Advances in the Astronautical Sciences, Spaceflight Mechanics 2001
- [30] F. Santoni, R. Ravaglia, F. Piergentili "Analysis of close approach in GEO using optical measurements", 63rd International Astronautical Congress Naples, Italy, 1-5 October 2012
- [31] DeMars, K.J.; Jah, M.K.; Schumacher, P.W, "Initial Orbit Determination using Short-Arc Angle and Angle Rate Data", Transactions on Aerospace and Electronic Systems, IEEE, Volume: 48, Issue: 3, DOI: 10.1109/TAES.2012.6237613, Publication Year: 2012, Page(s): 2628 -2637
- [32] F. Piergentili, M. L. Battagliere, F. Graziani, V. Agapov, I. Molotov, "FIRST (First Italian Russian Space debris Telescope)", Presentation given at the XXVIII IADC, WG1 Measurements, Trivandrum, India, March 9-12, 2010
- [33] F. Santoni, E. Cordelli, F. Piergentili, "Determination of Disposed-Upper-Stage Attitude Motion by Ground-Based Optical Observations", Journal of Spacecraft and Rockets, in print, (2013) doi:10.2514/1.A32372

- [34] E. Stöveken, T. Schildknecht, *“Algorithms for the Optical Detection of Space Debris Objects”*, Proceedings of the 4th European Conference on Space Debris (ESA SP-587). 18-20 April 2005, ESA/ESOC, Darmstadt, Germany. Editor: D. Danesy., p.637
- [35] T. Yanagisawa, A. Nakajima, H. Kurosaki, *“Detection of Small Geo Debris Using Automatic Detection Algorithm”*, Proceedings of the 4th European Conference on Space Debris (ESA SP-587). 18-20 April 2005, ESA/ESOC, Darmstadt, Germany. Editor: D. Danesy, p.147
- [36] M. Laas-Bourez, G. Blanchet, M. Boer, E. Ducrotte, A. Klotz, *“A new algorithm for optical observations of space debris with the TAROT telescopes”*, Advances in Space Research 44 (2009) 1270–1278
- [37] F. Paolillo, M. Porfilio, F. Piergentili, *“First Italian space debris observatory: the image processing automation”*, 58th IAC, International Astronautical Congress., International Astronautical Congress Proceedings, Issn: 1995-6258, Hyderabad, India, 24-28, September 2007
- [38] W. B. Rossow, R. A. Schiffer, *“Advances in Understanding Clouds”* from ISCCP. Bull. Amer. Meteor. Soc., 80, 2261-2288, 1999.
- [39] <http://www.ilmeteo.it/portale/medie-climatiche/> site available on April 2012
- [40] V. Agapov, V. Molotov, Z. Khutorovsky, *“GEO Protected Region Situation Analysis from the ISON observations”*, AMOS 2009 Conference
- [41] T. Schildknecht, R. Musci, M. Ploner, S. Preisig, J. de Leon Cruz, H.Krag, *“Optical Observation of Space Debris in the Geostationary Ring”*, Proceedings of the Third European Conference on Space Debris, Darmstadt, Germany, 19-21 March 2001.
- [42] A. Rossi, S. Marinoni, **T. Cardona**, E. Dotto, D. Perna, F. Santoni, F. Piergentili, *“Physical characterization of space debris in the geosynchronous region”*, paper IAC- 11,A6,1,7,x10320, 62nd International Astronautical Congress, Cape Town, South Africa.
- [43] A. Rossi, S. Marinoni, **T. Cardona**, E. Dotto, F. Santoni, F. Piergentili, *“The Loiano campaigns for photometry and spectroscopy of geosynchronous objects”*, 63rd International Astronautical Conference, Naples, Italy.
- [44] A. Rossi, S. Marinoni, **T. Cardona**, E. Dotto, F. Santoni, F. Piergentili, *“Physical characterization of objects in the GEO region with the Loiano 1.5m telescope”*, 6th European Conference on Space Debris, ESA/ESOC, Darmstadt/Germany, 22-25 April 2013.
- [45] T. Schildknecht, R. Musci, W. Flury, J. Kuusela, J. de Leon Cruz, L. de Fatima Dominguez Palmero, *“Optical Observations of Space Debris in High-Altitude Orbits – Discovery of a new Population”*, 2004 AMOS Technical Conference, September 13-17 2004, Maui, Hawaii, USA.
- [46] J. C. Liou, J. K. Weaver, *“Orbital Dynamics of High Area-To Mass Ratio Debris and Their Distribution in the Geosynchronous Region”*, Proceedings of the 4th European Conference on Space Debris (ESA SP-587). 18-20 April 2005, ESA/ESOC, Darmstadt, Germany. Editor: D. Danesy., p.285

- [47] R.Gualandi, R.Merighi, *“BFOSC – Bologna Faint Object Spectrograph & Camera. User Manual”*
- [48] E. Bertin, S. Arnouts, *“SExtractor: Software for source extraction”*, Astronomy and Astrophysics Supplement 117, 393–404
- [49] B. W. Holwerda, *“Source Extractor for Dummies”*, v5, arXiv:astro-ph/0512139
- [50] A. U Landolt, *“UBVRI photometric standard stars in the magnitude range 11.5-16.0 around the celestial equator”*, AJ 104, 340–371, 436–491
- [51] P. Seitzer, H. M. Cowardin, E. Barker, K. J. Abercromby, T. M. Kelecy, M. Horstman, *“Optical Photometric Observations of GEO Debris”*, 2010 AMOS Technical Conference, September 14-17 2010, Maui, Hawaii, USA.
- [52] H. M. Cowardin, P. Seitzer, K. J. Abercromby, E. Barker, T. Schildknecht, *“Characterization of Orbital Debris Photometric Properties Derived from Laboratory-Based Measurements”*, 2010 AMOS Technical Conference, September 14-17 2010, Maui, Hawaii, USA.
- [53] <http://orbitaldebris.jsc.nasa.gov/>
- [54] http://www.lsa.umich.edu/astro/people/seitzerpatrick_ci
- [55] <http://www.lco.cl/>
- [56] *“IMACS Spectrograph User Manual”*,
<http://www.lco.cl/telescopes-information/magellan/instruments/imacs/user-manual/the-imacs-user-manual>
- [57] *“FIRE User Manual”*, <http://web.mit.edu/~rsimcoe/www/FIRE/>
- [58] *“LDSS3 User Guide”*, <http://www.lco.cl/telescopes-information/magellan/instruments/ldss-3/ldss-3-users-guide/users-guide>
- [59] <http://www.ctio.noao.edu/noao/>
- [60] <http://www.lsa.umich.edu/astro/facilities/telescopes/curtisschmidt>
- [61] P. Seitzer, S. M. Lederer, H. Cowardin, **T. Cardona**, E. S. Barker, K. J. Abercromby, *“Visible Light Spectroscopy of GEO Debris”*, AMOS 2012 Conference
- [62] K. J. Abercromby, J. Rapp, D. Bedard, P. Seitzer, **T. Cardona**, H. Cowardin, E. Barker, S. Lederer, *“Comparisons of a Constrained Least Squares Model versus Human-in-the-loop for Spectral Unmixing to Determine Material Type of GEO Debris”*, Sixth European Conference on Space Debris, Darmstadt- Germany 22-25 April 2013
- [63] P. Seitzer, **T. Cardona**, S. M. Lederer, H. Cowardin, K. J. Abercromby, E. S. Barker, D. Bedard, *“Optical Reflection Spectroscopy of GEO Objects”*, 64rd International Astronautical Conference: 23-27 September 2013 Beijing, China
- [64] T. Schildknecht, A. Vananti, H. Krag, C. Erd, *“Reflectance Spectra of Space Debris in GEO”*, AMOS 2010 Conference.

- [65] H. Cowardin, K. J. Abercromby, E. S. Barker, P. Seitzer, M. Mulrooney, T. Schildknecht, “*An Assessment of GEO Orbital Debris Photometric Properties Derived from Laboratory-Based Measurements*”, AMOS 2009 Conference.
- [66] D. Bedard, “*Using a physics-based reflection model to study the reddening effect observed in spectrometric measurements of artificial space objects*”, AMOS 2011 Conference
- [67] **T. Cardona**, “*Analysis for 6.5-m Magellan telescope blind tracking*”, Presented at the MODEST Telecon 2012
- [68] T.S. Kelso, “*Validation of SGP4 and IS-GPS-200D Against GPS Precision Ephemerides*”, 17th AAS/AIAA Space Flight Mechanics Conference, Sedona, Arizona January 28–February 1, 2007
- [69] R. G. Brown, P. Y. C. Hwang, “*Introduction to Random Signals and Applied Kalman Filtering*”, 1992 Second Edition, John Wiley and Sons
- [70] G. Welch, G. Bishop, “*An Introduction to the Kalman Filter*”, UNC-Chapel Hill, TR 95-041, July 24, 2006
- [71] R. E. Kalman, “*A New Approach to Linear Filtering and Prediction Problems*”, 1960, ASME—Journal of Basic Engineering, pp. 35-45
- [72] <http://www.ctio.noao.edu/noao/content/SMARTS-09-m-Telescope>
- [73] S. M. Lederer, P. Seitzer, H. M. Cowardin, E. S. Barker, K. J. Abercromby, A. Burkhardt, “*Characterizing Orbital Debris and Spacecrafts through a Multi-Analytical Approach*”, AMOS 2012 Conference.
- [74] M. Jah, T. Kelecy, “*Studies of the Orbit of the MSG 2 Cooler Cover*”, IAC 2010.
- [75] <http://astro.unl.edu/naap/>
- [76] http://en.wikipedia.org/wiki/File:Ra_and_dec_on_celestial_sphere.png
- [77] http://spaceflight.nasa.gov/realdata/sightings/SSapplications/Post/JavaSSOP/SSOP_Help/tle_def.html
- [78] E. S. Barker, M. Matney, Y. Yanagisawa, J. C. Liou, K. J. Abercromby, H. M. Cowardin, M. F. Horstman, P. Seitzer, “*An Attempt to Observe Debris from the Breakup of a Titan 3C-4 Transtage*”, AMOS 2007 Conference
- [79] D. Bedard, “*Using a physics-based reflection model to study the reddening effect observed in spectrometric measurements of artificial space objects*”, AMOS 2011 Conference.
- [80] H. Cowardin, “*Observations of Titan IIIC Transtage Fragmentation Debris*”, AMOS 2013 Conference.
- [81] M. J. Gaffey, “*Space weathering and the interpretation of asteroid reflectance spectra*”, Icarus, Vol 209, Issue 2, p 564-574, 2010.

Acknowledgements

I am grateful to my thesis advisor, Professor Fabrizio Piergentili, for his guidance and support. His experience in observation of space debris and satellite orbital dynamics and control has improved my research skills and prepared me for future challenges. I will always be grateful for the opportunity he gave me to participate in so many research projects.

I thank Professor Patrick Seitzer for his support during all my time spent at the Astronomy Department of the University of Michigan. I am extremely thankful to him for his expert, sincere and valuable guidance and encouragements extended to me.

I take this opportunity to express my sincere thanks to all the members of the MODEST project: Gene Stansberry and Sue Lederer from NASA Johnson Space Center Orbital Debris Office, Heather Cowardin from ESCG/Jacobs for her inestimable help during the development of the non-sidereal tracking code, Kira Abercromby from CalPoly and Ed Barker from LZ Technology.

A special thanks goes to all the members of the observing night from Loiano: Alessandro Rossi from CNR, Silvia Marinoni from ASI, Elisabetta Dotto from INAF and Fabio Santoni from University La Sapienza. It has been a pleasure for me to work with all of you.

I wish to acknowledge the support received from the personnel of the Italian Space Agency, which made possible the observation test campaign from the Broglio Space Center in Kenya. I also express, my sense of gratitude to all the staff and technicians of the Loiano Observatory for their invaluable help during the observing sessions. I want to thank the staff of the Las Campanas Observatory for their help during the observing night at the Magellan telescope.

This dissertation would not have been possible without the help of my family and friends that have continuously supported me for all these years.

Tommaso Cardona